Spin-Dependent Transport Phenomena in Ferromagnet/Semiconductor Heterostructures

A DISSERTATION
SUBMITTED TO THE FACULTY OF THE GRADUATE SCHOOL
OF THE UNIVERSITY OF MINNESOTA
BY

Chad Christopher Geppert

IN PARTIAL FULFILLMENT OF THE REQUIREMENTS
FOR THE DEGREE OF
Doctor of Philosophy

Paul A. Crowell

June, 2014

© Chad Christopher Geppert 2014
ALL RIGHTS RESERVED

Acknowledgements

Te-yu Chen (陳得於), Michael Erickson, Lee Wienkes, Eric Garlid, Mun Chan, Steve Snyder, Kevin Christie, Andrew Galkiewicz, Changjiang Liu (刘长江), Timothy Peterson, Gordon Stecklein, Nicholas Krueger, Steve Snyder, Dima Spivak, Paul Crowell, Sahil Patel, Qi Hu (胡奇), Chris Palmstrøm, Michael Flatté, Nicholas Harmon, Boris Shklovskii, Adam Schreckenberger, Kevin Christie, Tianran Chen (陈天然), Joffrey Peters, Pamela Vo, Alexey Finkel, Joe Pastika, Ryo Namba (難波 亮), Sean Kalafut, and Michael Schecter, Steve and Rebecca Geppert, John Liao (廖妙友), Zöe Wang (王容英), David Dikken, Peng-Huei Liao (廖鵬惠), Isaiah Geppert (廖以恩), Hadassah Geppert (廖以樂), Elias Geppert (廖以聖)

This work was supported by NSF Grant No. DMR-1104951; by C-SPIN, one of the six centers of STARnet, a Semiconductor Research Corporation program sponsored by MARCO and DARPA; and by the NSF MRSEC program. Parts of this work were carried out in the Minnesota Nano Center which receives partial support from NSF through the NNIN program.

Dedication

À mes parents

Abstract

This dissertation examines several aspects of spin-dependent transport phenomena in epitaxially grown ferromagnet/n-GaAs heterostructures. Further maturation of the field of semiconductor-based spintronics is hindered by difficulties in evaluating device performance across materials systems. Using Fe/n-GaAs and Co_2MnSi/n-GaAs heterostructures as a test case, the main goal of this work is to demonstrate how such difficulties may be overcome by (1) specifying a more quantitative framework for evaluating transport parameters and (2) the introduction of a new spin-to-charge conversion phenomenon which may be parameterized by bulk semiconductor parameters.

In the introductory chapter, this work is placed in the broader context of developing improved methods for the generation, modulation, and detection of spins. The lateral spin-valve geometry is presented as a concrete example of the typical measurement procedures employed. Chapter 2 presents the charge-based transport properties of these samples and establishes the notation and calculation techniques to be employed in subsequent chapters. In particular, we examine in detail the calculation of the electrochemical potential for a given carrier concentration. Chapter 3 provides a full derivation of the equations governing spin-dependent transport in the large polarization regime. This is applied to the case of extracting spin lifetimes and diffusion rates, demonstrating how quantitative agreement with theoretical predictions may be obtained upon properly accounting for both device geometry and material parameters. Further examination of the boundary conditions applicable to the heterojunctions of these samples demonstrates to what extent device performance may be parameterized across materials systems.

Chapter 4 presents experimental observations of a new spin-to-charge conversion phenomenon using a non-magnetic probe. In the presence of a large non-equilibrium spin accumulation, the combination of a non-constant density of states and energy-dependent conductivity generates an electromotive force (EMF). It is shown that this signal dephases in the presence of applied and hyperfine fields, scales quadratically with the polarization, and is comparable in magnitude to the spin-splitting. Since this spin-generated EMF depends only on experimentally accessible parameters of the bulk material, its magnitude is used to

quantify the injected spin polarization in absolute terms, independent of any assumptions regarding the spin-resistance of the interface.

Chapter 5 examines spin-dependent contributions to signals measured in the Hall geometry. In particular, a large scattering asymmetry develops in the presence of hyperfine interactions with dynamically polarized nuclei. A pulsed measurement technique is introduced which allows the polarization of the electron spin system and nuclear spin system to be manipulated independently. Based on these results, a possible mechanism is presented based on inhomogeneities in the nuclear polarization. This motivates a phenomenological model which is compared against experimental data using the modeling techniques of the previous chapters.

Contents

Acknowledgements **i**

Dedication **ii**

Abstract **iii**

List of Tables **viii**

List of Figures **ix**

1 Introduction to spintronics **1**

1.1 Example: Lateral spin valve 2

2 Semiconductor fundamentals **6**

2.1 Conduction band of zinc-blende semiconductors 7

2.2 Charge transport properties 7

2.3 Electrochemical potential 9

2.3.1 Preliminary definitions 9

2.3.2 Parabolic conduction band (CB) 11

2.3.3 Modeling the density of states in the band tail 12

2.3.3.1 Band-tail: Blakemore model 14

2.3.3.2 Band-tail: Kane DOS model 14

2.3.3.3 Band-tail: Modified Kane DOS 16

2.4 Energy dependence of the momentum relaxation time 16

3 Electrical spin injection and detection **20**

3.1 Theory of diffusive spin-transport 20

3.1.1 Current densities 21

3.1.2 Polarized drift and diffusion 23

3.1.3 Small polarization limit . . . 28
3.1.4 Homogeneous magnetic field . . . 28
3.2 Drift-diffusion models . . . 30
3.2.1 Spin resistances . . . 30
3.2.2 0D model: Lorentzian . . . 32
3.2.3 1D model: vertical diffusion . . . 33
3.2.4 1D model: lateral diffusion . . . 38
3.3 Non-local Hanle fitting . . . 41
3.3.1 Temperature dependence of D . . . 43
3.3.2 Temperature dependence of τ_s . . . 43
3.4 Boundary conditions . . . 46
3.4.1 Transparent interfaces . . . 46
3.4.2 FM/n-GaAs interface . . . 48
3.4.3 Tunneling currents – interface conductances . . . 49
3.4.4 Tunneling currents – localized states . . . 55

4 Spin-generated electromotive force **58**
4.1 Phenomenological model of the spin-generated EMF . . . 60
4.2 Shorted-Hall measurements . . . 66
4.3 Dual-injector experiment . . . 68
4.4 Oblique Hanle measurements . . . 68
4.5 Comparison with non-local data: quadratic scaling . . . 72
4.6 Modeling . . . 72
4.7 Temperature dependence . . . 78
4.8 Corrections . . . 83

5 Hyperfine-induced Hall effect **86**
5.1 Device design: local Hall geometry . . . 87
5.2 Pump-probe measurements . . . 92
5.3 Bias dependence . . . 94
5.4 Hyperfine-enhanced spin-relaxation . . . 99
5.4.1 Resonant skew scattering . . . 103
5.5 Angle dependence . . . 107

6 Conclusions **113**

References **115**

A Derivations **121**
A.1 Compressibility and higher derivatives 121
A.2 Derivation of spin-dependent current densities 122
A.3 Energy dependence of mobility and diffusion constant 123

List of Tables

2.1 Material parameters for n-GaAs 7

3.1 Momentum scattering factor γ_3 for each scattering mechanism 45

5.1 Optimized modeling parameters 109

List of Figures

1.1 2011 International Technology Roadmap for Semiconductors[1] – Executive Summary, Fig. 5 2

1.2 Components of a spintronic device. 3

1.3 (a) Cartoon of non-local spin valve device (b) Non-local spin valve data acquired sweeping a magnetic field in the plane of the device 4

2.1 Degenerate Pauli gas polarized out of equilibrium. 6

2.2 Charge transport properties for sample UMN023-01 as a function of temperature. (a) Resistivity (b) Conductivity (c) Drift (Hall) mobilities shown in solid black (dotted red) line (d) Doping (Hall) concentration shown in solid black (dotted red) line (e) Hall factor assuming $r_{300\text{ K}} = 1$. 8

2.3 (a) Chemical potential vs. temperature and (b) inverse compressibility vs. temperature for the models described in the text. 13

2.4 Density of states vs. energy 15

2.5 Energy exponent vs. temperature obtained from Hall factor (solid lines) and magnetoresistance (dashed lines) for three different carrier concentrations: $3.8 \times 10^{16}/\text{cm}^3$ (black, sample UMN023), $5.5 \times 10^{16}/\text{cm}^3$ (red, sample UMN019), $8.4 \times 10^{16}/\text{cm}^3$ (blue, sample UMN026). 18

3.1 Energy dependence of the (a) mobility and (b) diffusion constant as a function of temperature, normalized by the polarization. Solid, dashed, and dotted curves correspond to scattering exponents of $+\frac{3}{2}$ (ionized impurity), $+\frac{1}{2}$ (acoustic phonon, piezoelectric), and $-\frac{1}{2}$ (acoustic phonon, deformation potential) respectively. 26

3.2 Polarization dependence of the conductivity polarization (solid), diffusion constant (dashed), and charge conductivity (dotted). These curves were evaluated at a concentration of $n = 2n_c$ assuming a scattering exponent of 3/2 (ionized impurity scattering). 27

3.3 (a) Cartoon of balance between spin injection and relaxation. (b) Real and imaginary components of the spin resistance r_{0D} as a function of applied transverse field B. 32
3.4 Spins allowed to diffuse into a one-dimensional channel. 34
3.5 Comparison of Hanle line-shapes for the 0D and 1D models. 35
3.6 Bias dependence of (a) polarization at interface and (b) spin diffusion length. 37
3.7 Phase diagram of current polarization vs. current density. Colored dots correspond to the arrows indicating saturation points in Fig. 3.6(a). 38
3.8 1D lateral spin-valve model divided into four regions. 39
3.9 Spin resistance vs. position for the 1D lateral diffusion model for four different values of the drift current J. 41
3.10 (a) Non-local spin valve with field applied out-of-plane. (b) Bias and dependence of non-local Hanle signal. (c) Temperature dependence of non-local Hanle signal. Gray open circles are the experimental data (after background subtraction) and the blue solid lines the result of fitting with the model presented in Sec. 3.2.4. (Sample UMN022-01B) 42
3.11 (a) Diffusion constant extracted from non-local Hanle fitting (black points) in comparison with values predicted from the Einstein relation (solid line). The extracted spin lifetimes are shown as red points and correspond to the right axis. (b) Spin diffusion length λ_s as a function of temperature. 44
3.12 Temperature dependence of τ_s extracted from non-local Hanle measurements for (a) an Fe/n-GaAs sample (UMN019-04B) and (b) a Co_2MnSi/n-GaAs sample (UMN022-01B). (c) Doping dependence of τ_s for 30 K, 60 K, and 90 K. 47
3.13 Spin currents at a transparent interface between a ferromagnet (FM) and non-magnetic semiconductor (S). Egregiously not to scale. 48
3.14 (a) Material structure of FM/n-GaAs heterostructure (b) Schottky tunnel barrier and localized quantum well states at interface. 50
3.15 Potential levels near a forward biased FM/n-GaAs heterojunction. The thick dashed lines indicate the electrochemical potential in the absence of a spin accumulation. 51

4.1 Introduction of the spin-generated EMF by analogy to the Seebeck effect. . 59
4.2 Physical origin of the spin-generated EMF as a difference in diffusion rates. 61

4.3 (a) Diagram of chemical potentials in the presence (left) and absence (right) of spin accumulation. (b) Current density as a function of non-local position for each spin band (↑ red, ↓ blue) and their total (black). Dotted (solid) curves exclude (include) the contribution from the steady-state potential ϕ. (c) Magnitude of ϕ and average chemical potential shift $\Delta\mu_{avg}$ vs. non-local position. 64
4.4 (a) Cartoon of shorted Hall device allowing three independent spin detection methods. (b) Micrograph of a Co_2MnSi/n-GaAs lateral spin valve device (sample UMN023-02D) with shorted central Hall arms for electrostatic detection of spin accumulation. 65
4.5 (a) Non-local spin valve (field in-plane) and Hanle effect (field out-of-plane) measured at contact D with forward current bias on contact B. (b) Hanle effect observed at contact C under identical conditions as panel (b) for both magnetization directions of contact B. 67
4.6 (a) Wiring diagram for the spin-EMF measurement. (b) Raw voltages measured between contacts C and H at 60 K, 75 K, and 90 K. Solid gray lines indicate 3rd-order polynomial background. No offset applied. (c) Same data as (b), but with third-order polynomial background subtracted and offset for clarity. Dotted gray lines indicate magnitude of cubic background term only. 69
4.7 (a) Wiring diagram for the dual-injector experiment. (b) Spin valve and (c) Hanle effect data measured at contact C with identical current biases applied simultaneously to contacts B and D. 70
4.8 Oblique Hanle effects observed at (a) ferromagnetic injector B (three-terminal), (b) semiconducting arms C (spin-generated EMF), and (c) remote ferromagnetic detector D (non-local) under identical conditions with forward current bias on contact B. 71
4.9 Log-log plot of the spin-generated EMF observed at contact C vs. (ferromagnetic) non-local spin-valve magnitude at contact D showing a quadratic dependence at low biases. Solid lines have a slope of 2. 73
4.10 (a) Three-dimensional simulation geometry. (b) Simulation geometry overlaid on top of micrograph of device. Blue (red) indicates channel (interface) region. (c) Contour plot of kp^2 obtained from simulation at 60 K. 74
4.11 Definitions of vectors $\hat{n}_0$ normal to all surfaces of the device and $\hat{n}$ normal to the contact regions. 75

4.12 (a) Contour plot of ϕ_b obtained from Laplace relaxation. Vectors show spin-EMF induced eddy currents $\propto \vec{\nabla}\phi_b$. (b) Contour plot of $kp^2 + \phi_b$ showing the equipotential in the contact regions and potential drop between Hall arm contacts C and remote counter-electrode H. 77
4.13 (a) Number polarization and (b) current polarization vs. temperature at injector contact B determined from the magnitude of the spin-generated EMF (Co_2MnSi: black squares, Fe: blue circles). 79
4.14 (a) Magnitude of 3T signal as a function of temperature. Green shaded region indicates the estimate contribution from the spin-EMF. (b) 3T magnitude after subtracting the contribution from the spin-EMF. Red line shows the expected contribution determined from (ferromagnetic) non-local measurements. 80
4.15 Detection efficiency as a function of temperature extracted from Eq. 4.26. . 82
4.16 Spin-EMF prefactor for different scattering mechanisms. 83
4.17 Prefactor for the spin-generated EMF as a function of temperature for the four models discussed in Sec. 2.3. 85

5.1 Local Hall geometry wired for (a) spin-dependent Hall and (b) three-terminal measurements. (c) Micrograph of Fe/n-GaAs sample (UMN019-02I). 88
5.2 (a, b) ‘Parallel’ and ‘perpendicular’ device geometries. (c, d) Expected magnitude and width of Hanle curves. 90
5.3 (a, b) ‘Parallel’ and ‘perpendicular’ device geometries. (c, d) Raw spin-dependent Hall data. (e, f) Spin-dependent Hall data after removal of quadratic background. (g, h) Three-terminal measurement under identical conditions. 91
5.4 (a) Micrograph of mis-aligned Co_2MnSi/n-GaAs sample (UMN023-02I). (b) Raw spin-dependent Hall data for both magnetization directions. (c) Component of signal odd with respect to magnetization. No background subtracted. (d) Component of signal even with respect to magnetization. Second-order polynomial background subtracted. 93
5.5 (a) Timing diagram for pulsed measurement sequence. (b) ISHE Hanle signal measured for several different wait times. (c) Magnitude of ISHE signal vs wait time fitted to stretched exponential functions with exponents $\beta = 0.56$ (black), $\beta = 0.5$ (red), and $\beta = 1.0$ (blue). 95
5.6 Timing diagram for the pump-probe measurement. 96
5.7 (a) Magnitude of ISHE signal as a function of current densities j_{probe} and j_{pump}. (b) Non-local spin valve vs. current density. 97

5.8 (a) Quadratic dependence of the ISHE magnitude on spin injection rate of the probe pulse. Solid lines are a fit to the quadratic form given in Eq. 5.9. (b) Linear dependence of the ISHE magnitude on spin injection rate of the pump bias. 98
5.9 Cartoon showing an electron spin traversing inhomogeneities in the nuclear system. 100
5.10 Diagram showing behavior of a spin polarized ensemble in (a) homogeneous and (b) inhomogeneous environments. 101
5.11 Diagram of oblique Hanle field direction 106
5.12 3T signal as a function of angle (gray). Modeling shown (a) without and (b) with additional source of spin relaxation due to nuclear polarization. 108
5.13 Experimental ISHE signal for several oblique angles shown in gray. (a) Modeling using the normal ISHE prediction of Eq. 5.1. (b) Modeling using the anisotropic expression in 5.38. 110
5.14 (a) Wiring diagram for perpendicular device. (b) Experimental angle dependence obtained on Fe/*n*-GaAs device. (c) Modeling using the normal ISHE prediction of Eq. 5.1. (d) Modeling using the anisotropic expression in 5.38. 112

Chapter 1

Introduction to spintronics

The work in this dissertation falls under the ever broadening scope of the field known as 'spintronics', the central aim of which is to investigate devices whose principle of operation depends on the intrinsic angular momentum of the electron[2]. The desired outcome of such research is generally cited as being (a) the demonstration of superior performance to existing structures or (b) the development of devices which exhibit novel functionality. These two aims are nicely illustrated by the ordinate and abscissa respectively of the general semiconductor roadmap shown in Fig. 1.1. In particular, incorporating the spin degree of freedom into existing device applications was demonstrated by the discovery of giant magnetoresistance by Fert[3] and Grünberg[4] for which the Nobel Prize was awarded in 2007. The potential for novel device functionality was suggested by the spin-based field effect transistor (spin-FET) proposal of Datta and Das[5]. Based on the general paradigm of leveraging additional degrees of freedom for the purpose of device development, other nascent fields are beginning to develop: spin-caloritronics[6], spin-orbitronics[7], valleytronics[8], and straintronics[9].

Inherent in all such endeavors is the relatively higher uncertainty associated with convolving more than one physical process in the signal output. Each spintronic device may be viewed as performing three tasks: spin generation, spin modulation, and spin detection. This is illustrated by the 'menu' of generation and detection choices shown in Fig. 1.2, which is far from exhaustive. Typical research efforts focus on either improving the efficiency of one of the listed components, or on introducing more exotic entries to Fig. 1.2. However, isolating a single component for characterization requires assumptions about the behavior of the other elements, which are often not independently measurable. The resulting spin-dependent signal is a convolution all three processes: spin generation, spin modulation/transport, and spin detection. Progress towards the goals stated above there-

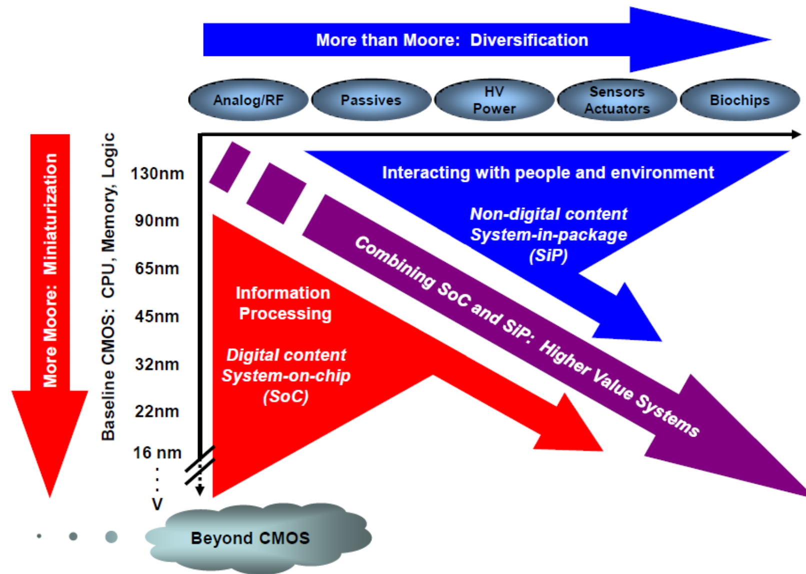

Figure 1.1: 2011 International Technology Roadmap for Semiconductors[1] – Executive Summary, Fig. 5

fore depends on establishing a quantitative understanding of each these processes.

Despite recent progress in demonstrating electrical spin injection and detection in a wide variety of semiconducting materials systems[10, 11, 12, 13, 14, 15, 16, 17, 18, 19, 20, 21, 22, 23, 24], quantitative comparison among these experimental efforts is hindered primarily by difficulties in distinguishing between bulk and interfacial effects. One of the main goals of this dissertation is to demonstrate how such difficulties may be overcome by (1) developing a more quantitative framework than what has been employed in past efforts, (2) properly parameterizing the efficiencies of each component to allow comparisons across material systems, and (3) introducing a new spin-to-charge conversion phenomenon which depends only on experimentally accessible material parameters.

1.1 Example: Lateral spin valve

To provide a concrete example of the process discussed above, we start with a description of the lateral non-local spin valve device shown in Fig. 1.3(a). In this device, ferromagnetic contacts are used to generate as well as to detect non-equilibrium spin accumulation in the semiconducting channel. A constant current bias is applied between the injector contact labeled 'B' and the remote counter-electrode labeled 'A'. This causes spins to be injected (or extracted) at contact 'B' in the center of the channel. Notice that in this configuration,

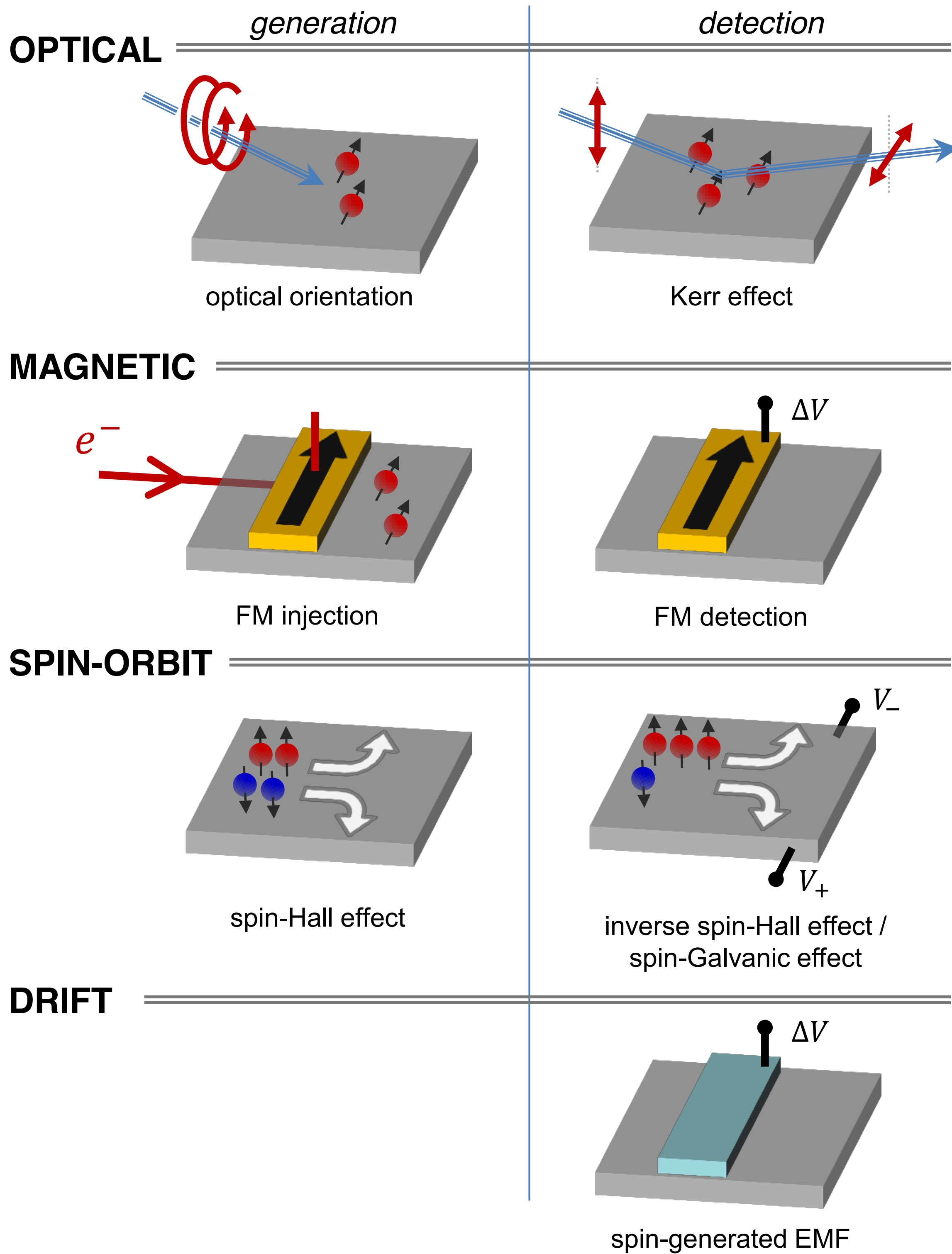

Figure 1.2: Components of a spintronic device.

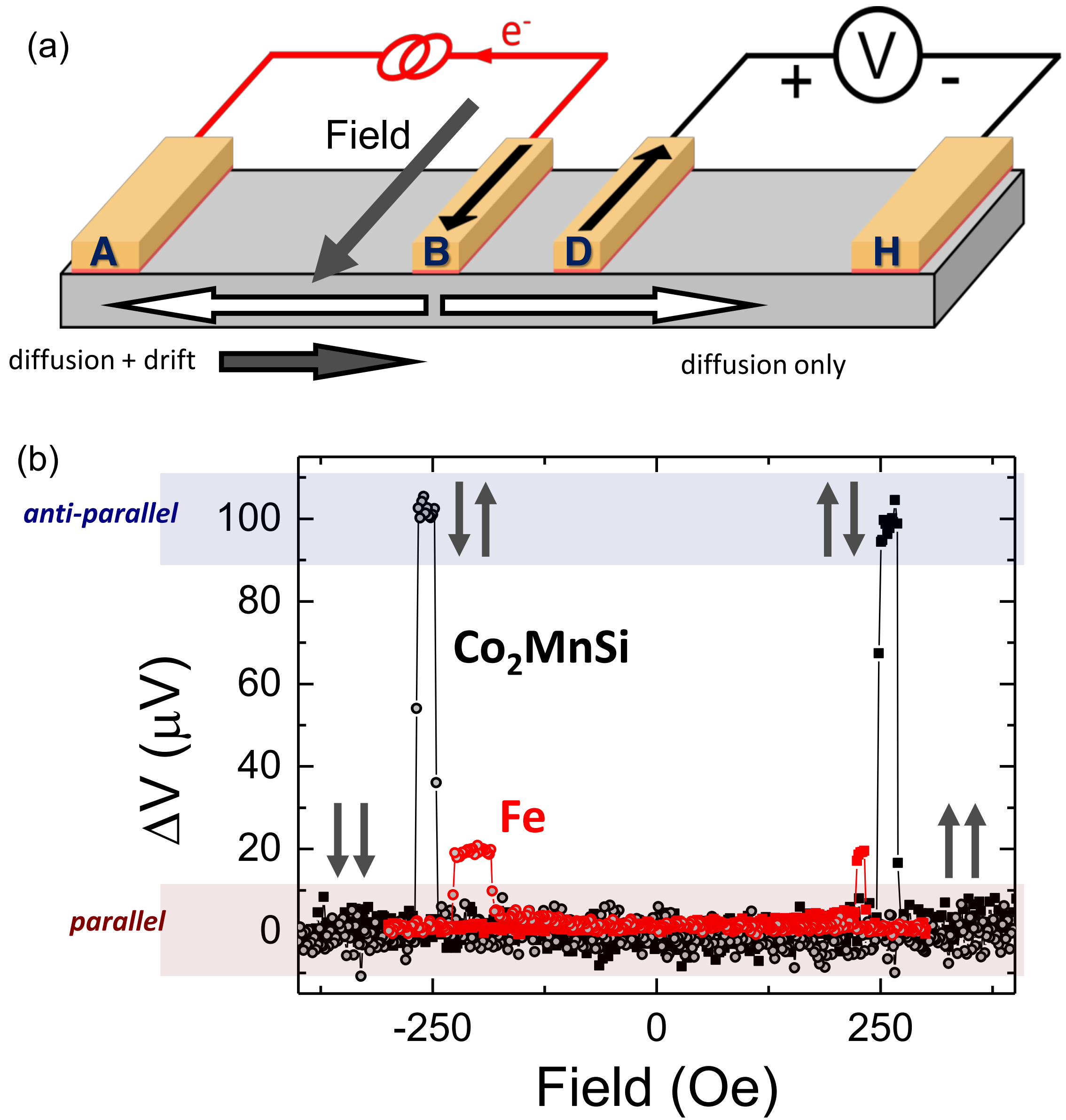

Figure 1.3: (a) Cartoon of non-local spin valve device (b) Non-local spin valve data acquired sweeping a magnetic field in the plane of the device

the ferromagnetic detector labeled 'D' lies outside of the charge current path, i.e. in the non-local region. This helps to reduce unwanted magnetoresistive contributions to the spin signal. The spins are detected as a chemical potential shift at detector contact 'D' relative to the remote voltage counter-electrode labeled 'H'.

Fig. 1.3(b) shows the experimental data upon application of an in-plane field. Sharp jumps in the voltage signal are observed when the magnetization of the injector and detector contacts switches between the parallel and anti-parallel configurations. The black curve shows results obtained for a Co_2MnSi Heusler alloy ferromagnet epitaxially grown on n-type GaAs. The red curve shows spin valve data acquired on an identical device where Fe was used as the ferromagnet instead. Since the magnitude of these two curves differs by a factor of five, we may ask which component of the device is primarily responsible. Is the enhanced signal from the Co_2MnSi device due to a larger efficiency of the injection process? Or since the same ferromagnetic material constitutes both the injector and detector contacts, is it due to an improvement in both? To what extent do inevitable variations in the channel properties play a role?

It will be demonstrated in Chap. 4 that the efficiency of the spin injection process is roughly equal for both devices (see Fig. 4.13(b)). We know from the spin transport measurements of Chap. 3 that spins diffuse farther in the Co_2MnSi device, but that the conversion from polarization to voltage is smaller. As such, we may attribute most of the signal enhancement to the detection efficiency of the unbiased detect contact.

Chapter 2

Semiconductor fundamentals

To support a general discussion of the relevant parameters for describing spin transport in semiconductors, we must first introduce some background information about charge-based transport. The reason for this is illustrated in Fig. 2.1, which shows a degenerate Pauli gas polarized out of equilibrium. The chemical potentials for spin-up and spin-down electrons reside at different energies denoted $\mu_\uparrow$ and $\mu_\downarrow$ respectively. Thus, an understanding of the energy dependence of unpolarized transport is a prerequisite for even the simplest model of polarized transport in which the spin-up and spin-down electrons behave independently. The extent to which such a 'non-interacting' model may be used to interpret experimental data will be discussed in future chapters. In this chapter, we introduce the band structure and charge-based properties of our samples, as well as establish the nomenclature and computational techniques which will be employed in subsequent chapters. In Sec. 2.1 we introduce the main features of the band structure of GaAs, focusing in particular on the sources of spin-orbit coupling. Sec. 2.2 presents typical charge transport parameters of

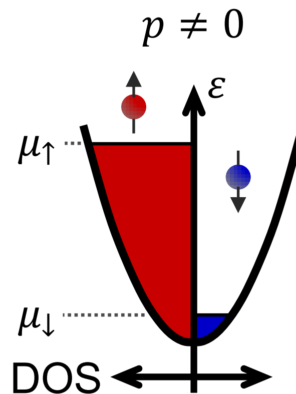

Figure 2.1: Degenerate Pauli gas polarized out of equilibrium.

Table 2.1: Material parameters for n-GaAs

Parameter	Expression (SI units)	Value
effective mass	$m^\star$	$0.067m_0$
dielectric constant	ϵ	$12.0\epsilon_0$
effective Bohr radius	$a_B^\star = 4\pi\epsilon\hbar^2/m^\star e^2$	94.8 Å
donor binding energy	$\varepsilon_B = e^2/4\pi\epsilon\left(2a_B^\star\right)$	6.3 meV, 73 K
critical concentration	$n_c = \left(0.26/a_B\right)^3$	$2.1\times10^{16}/\mathrm{cm}^3$

our samples and discusses the consequences of being doped just above the metal-insulator transition. Finally, Sec. 2.3 concludes with a detailed discussion on the calculation of electrochemical potential which forms the basis for later spin-dependent calculations.

2.1 Conduction band of zinc-blende semiconductors

We start with the following dispersion relation for the bulk conduction band of GaAs[25]:

$$\varepsilon\left(\vec{k},\vec{\sigma}\right) = \frac{\hbar^2k^2}{2m^\star} + \frac{g^\star\mu_B}{2}\vec{B}\cdot\vec{\sigma} + \frac{\hbar}{2}\vec{\Omega}\left(\vec{k}\right)\cdot\vec{\sigma} + \lambda_{SO}\left(\vec{k}\times\vec{\nabla}V\right)\cdot\vec{\sigma}, \tag{2.1}$$

where $m^\star = 0.067m$ is the effective mass and $g^\star = -0.44$ is the effective g-factor. The third term is known as the Dresselhaus spin orbit term and has the form

$$\frac{\hbar}{2}\vec{\Omega}_D\left(\vec{k}\right) = \beta\left\{k_x\left(k_y^2-k_z^2\right), k_y\left(k_z^2-k_x^2\right), k_z\left(k_x^2-k_y^2\right)\right\} \tag{2.2}$$

with a prefactor[25] of $\beta \simeq 19.55$ meV nm^3 extracted from fourth-order $\vec{k}\cdot\vec{p}$ perturbation theory. The fourth term of Eq. 2.1 is the Pauli-like spin-orbit term which in GaAs has a prefactor of $\lambda_{SO} = 5.2$ Å^2.

2.2 Charge transport properties

The charge transport properties of our samples are shown in Fig. 2.2 as a function of temperature. Our samples are doped slightly above the Mott criterion for the metal-insulator transition (MIT):

$$n_c^{1/3}a_B \approx 0.26. \tag{2.3}$$

where a_B denotes the effective Bohr radius for a hydrogenic impurity. For n-GaAs, the transition occurs at $n_c \approx 2.1\times10^{16}/\mathrm{cm}^3$. This parameter, along with several others relevant to our samples are listed in Table 2.1. This doping level was chosen due to the maximal spin

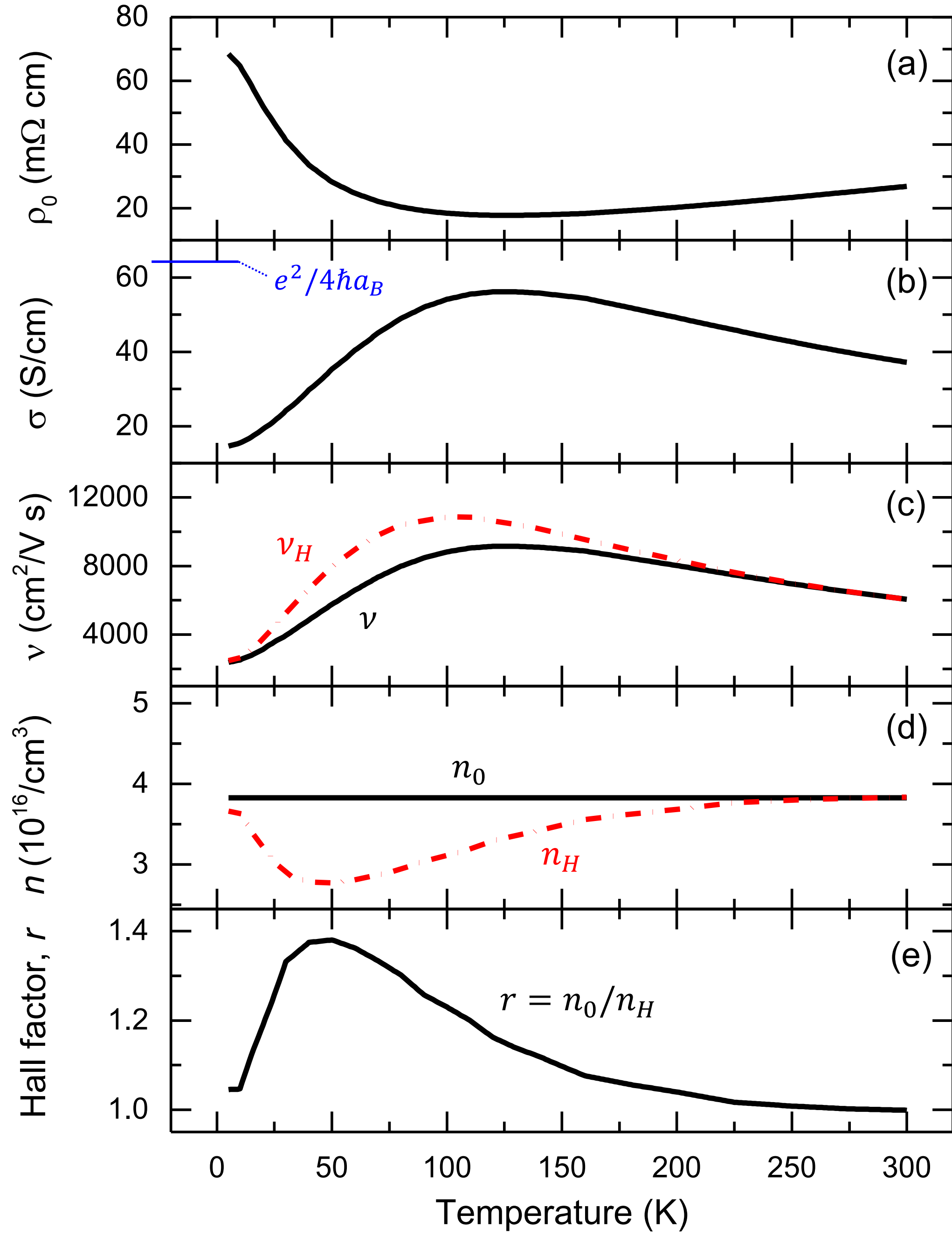

Figure 2.2: Charge transport properties for sample UMN023-01 as a function of temperature. (a) Resistivity (b) Conductivity (c) Drift (Hall) mobilities shown in solid black (dotted red) line (d) Doping (Hall) concentration shown in solid black (dotted red) line (e) Hall factor assuming $r_{300\ \mathrm{K}} = 1$.

lifetime which occurs near the MIT. Because the MIT in n-GaAs occurs in the impurity band[26, 27, 28], not all models assuming free electron conduction are fully applicable. One of the goals of the subsequent sections is to establish under what conditions such models, the density of states in particular, are applicable.

A discussion of the rich physics related to the MIT is beyond the scope of this work. However, one important consequence for our samples is the presence of nearly-isolated donor sites which weakly hybridize with the conduction band. These donor sites permit the exchange of spin information with the nuclear system via the Fermi contact hyperfine interaction[29, 30]. The influence of these states on spin transport is discussed further in Chap. 5.

2.3 Electrochemical potential

In this section we present several models for calculating the electrochemical potential from a knowledge of the density of states (DOS) in n-GaAs doped just above the metal insulator transition. This allows us to connect the phenomenological transport coefficients obtained in the previous section (2.2) with quantities more relevant for understanding spin transport. Simple formulae exist, of course, for describing systems in either the fully degenerate or non-degenerate limits. However, for n-GaAs doped just above the metal insulator transition, neither limit is valid over the range of typical experimental temperatures.

In particular, choosing a proper model for the DOS allows us to calculate the electronic bulk modulus, denoted κ^{-1}. This is the energy cost associated with increasing the number of carriers in the system. This quantity has several important uses. First, it allows us to calculate the diffusion constant from a knowledge of the mobility and carrier concentration. Second, it provides a direct conversion factor between spin polarization and chemical potential splitting. Third, knowing the energy dependence of κ^{-1} allows us to quantify the new source of electromotive force demonstrated in Ch. 4.

The main goal of this section is to demonstrate that, while these systems cannot be regarded as being fully metallic, the influence of the impurity levels on the structure of the DOS does not significantly influence the calculation of the chemical potentials needed for our subsequent analysis.

2.3.1 Preliminary definitions

We start by writing the *electrochemical* potential ζ as being composed of both chemical and *electrostatic* contributions:

$$\zeta = \mu - e\phi. \tag{2.4}$$

Here ϕ denotes the electrostatic potential and e the magnitude of the unit charge. The chemical potential[1] μ is defined as the derivative of the local (Helmholtz) free energy density F with respect to the electron density n:

$$\mu = \frac{\partial F}{\partial n}. \tag{2.5}$$

This will be generalized to the polarized case in Chapter 3 where F may be a function of more than one chemical species. The electron density is related to the electrochemical potential via the usual expression:

$$n = \int_{-\infty}^{\infty} g(\varepsilon) f(\varepsilon - \zeta) \, d\varepsilon, \tag{2.6}$$

where $g(\varepsilon)$ denotes the density of states (DOS) at energy ε and $f(\varepsilon - \mu) = \left[e^{(\varepsilon-\mu)/k_B T} + 1\right]^{-1}$ the Fermi-Dirac distribution function. k_B is Boltzmann's constant and T is the temperature of the system.

The electrochemical potential $\zeta = \mu - e\phi$ defined above is the quantity observed experimentally as a voltage difference between two points in our devices, i.e. $V = \Delta\zeta/(-e)$. Equivalently, gradients of this quantity give rise to charge current densities of the form

$$\vec{j} = -\sigma \vec{\nabla}\zeta/(-e) = eD\vec{\nabla}n - \sigma\vec{\nabla}\phi, \tag{2.7}$$

where σ is the (isotropic) electrical conductivity. The first and second terms are statements of Fick's law and Ohm's law respectively. The diffusion constant D appears as a consequence of choosing to write $\vec{j}$ in terms of gradients of n rather than gradients of μ. Consistency between Eqs. 2.4 and 2.7 requires that

$$\sigma = e^2 D \frac{\partial n}{\partial \mu}, \tag{2.8}$$

which is known as the Einstein relation. Note that this is sometimes referred to as the 'generalized' form of the Einstein relation to distinguish it from the degenerate and non-degenerate limits are frequently seen in the literature:

$$\text{(non-degenerate)} \qquad \sigma = e^2 Dn/k_B T \tag{2.9a}$$

$$\text{(degenerate)} \qquad \sigma = e^2 Dg(\varepsilon_F) \tag{2.9b}$$

[1]Within the context of semiconductor physics, this quantity is more traditionally refered to as the *Fermi level* and is often denoted as E_F or some variant thereupon[31, 32]. We depart from this nomenclature to avoid confusion with the *Fermi energy*, which refers to its zero temperature value denoted by us as ε_F.

Unfortunately, there exist several works in the literature which misapply these limits in place of Eq. 2.8. (Ref. [33] exemplifies the former and Ref. [34] points out an important example of the latter.) Although Eqs. 2.9a and 2.9b are easier to parameterize based on the measurements of Sec. 2.2, neither limit is appropriate for describing the full temperature range over which our samples were measured (≈ 0.5 to $5\varepsilon_F/k_B$). It is therefore necessary to assume a form for the density of states $g(\varepsilon)$ which will allow us to determine the quantity $\partial n/\partial\mu$ from the carrier concentration n and conductivity σ.

For the remainder of our discussion, in which the electrostatic potential ϕ is homogeneous[2], we assume that the levels are suitably defined such that $\phi = 0$. We now introduce the electronic compressibility as

$$\kappa = \frac{\partial n}{\partial\mu} = \frac{\partial^2 F}{\partial\mu^2}. \tag{2.10}$$

Note that assuming the conductivity $\sigma = ne\nu$ is proportional to the carrier concentration and mobility ν, the Einstein relation can be written more compactly as the ratio $D/\nu = n/e\kappa$. For higher dopings and/or lower temperatures, the system becomes *more* degenerate and *more* compressible. This implies, perhaps non-intuitively, that the spin-splitting *increases* as a function of temperature for a given value of the spin accumulation.

2.3.2 Parabolic conduction band (CB)

For a band with a parabolic dispersion relation $\varepsilon(k) = \hbar^2k^2/2m^\star$, the density of states is given by

$$g_{CB}(\varepsilon) = \frac{\partial n}{\partial\varepsilon} = \frac{(2m^\star)^{3/2}}{2\pi^2\hbar^3}\varepsilon^{1/2}\theta(\varepsilon), \tag{2.11}$$

where $m^\star$ denotes the effective mass and the bottom of the band has been defined at $\varepsilon = 0$. $\theta(x)$ denotes the Heaviside theta function. For convenience, we make use of the dimensionless quantities reduced temperature $x = \varepsilon/k_BT$ and reduced chemical potential $\xi = \mu/k_BT$. This allows us to write Eq. 2.6 in a more compact form as

$$n_{CB}(\xi, T) = \frac{(2m^\star k_BT)^{3/2}}{2\pi^2\hbar^3}\int_0^\infty \frac{x^{1/2}d\xi}{e^{x-\xi}+1} = n_Q(T)\,\mathcal{F}_{1/2}(\xi). \tag{2.12}$$

$n_Q(T)$ is known as the quantum concentration. The function $\mathcal{F}$ can be expressed more generally as

$$\mathcal{F}_\alpha(\xi) = \frac{1}{\Gamma(\alpha+1)}\int_0^\infty \frac{x^\alpha dx}{e^{x-\xi}+1} = -\mathrm{Li}_{1+\alpha}\left(-e^\xi\right), \tag{2.13}$$

[2] This will not be the case in Ch. 4 where spacial variations of the spin polarization require a clear distinction between the roles of chemical potential and electrostatic potential.

where $\Gamma(z)$ is the gamma function and $\mathrm{Li}_\nu(z)$ is the polylogarithm. When written in this form, Eq. 2.13 has the following useful property under differentiation

$$\mathcal{F}'_\nu(\xi) = \mathcal{F}_{\nu-1}(\xi)\,. \tag{2.14}$$

Note that if the concentration is known, ξ may be obtained by solving Eq. 2.12 numerically[3]. For later reference, we list below expressions for the compressibility as well as its first derivative with respect to chemical potential:

$$\kappa_{CB} = \frac{n_Q(T)}{k_B T}\mathcal{F}_{-1/2}(\xi) \tag{2.15}$$

$$\frac{\partial \kappa_{CB}}{\partial \mu} = \frac{n_Q(T)}{(k_B T)^2}\mathcal{F}_{-3/2}(\xi)\,. \tag{2.16}$$

2.3.3 Modeling the density of states in the band tail

In this section we examine a few different approaches for including the influence of the impurity band on the density of states. The main purpose is to establish the domain of applicability for the models to be developed in future chapters. The disorder in the system is given roughly by the binding energy $\varepsilon_B \approx 70$ K, which happens to coincide with the Fermi energy in the samples examined this this work $\varepsilon_F \approx 6$ meV. In general, we expect the influence of the impurity states to be much weaker as the temperature is raised and the system trends toward non-degenerate behavior.

Our results using models described in this section are summarized in Fig. 2.3(a), which shows the position of the chemical potential as a function of temperature for a concentration of $2n_c$. Fig. 2.3(b) plots the temperature dependence of the inverse compressibility as the ratio D/ν. Note that this ratio features prominently in our analysis of spin-dependent phenomena. It provides the proper conversion between fractional number polarization and chemical potential splitting as

$$p = \frac{n_\uparrow - n_\downarrow}{n_\uparrow + n_\downarrow} = \frac{(\mu_\uparrow - \mu_\downarrow)/2e}{D/\nu} \tag{2.17}$$

From the results in Fig. 2.3, we conclude that for temperatures above 30 K we do not need to include the influence of the band tail states in our calculations. This is confirmed via the non-local Hanle measurements of Sec. 3.3 which allow us to extract independent information about the compressibility of the system. The influence of band tail states will

[3]This may be accomplished rather concisely in Mathematica with commands of the form `FindRoot[n==-nQ[T]PolyLog[`$\frac{3}{2}$`,-Exp[ξ]]]`.

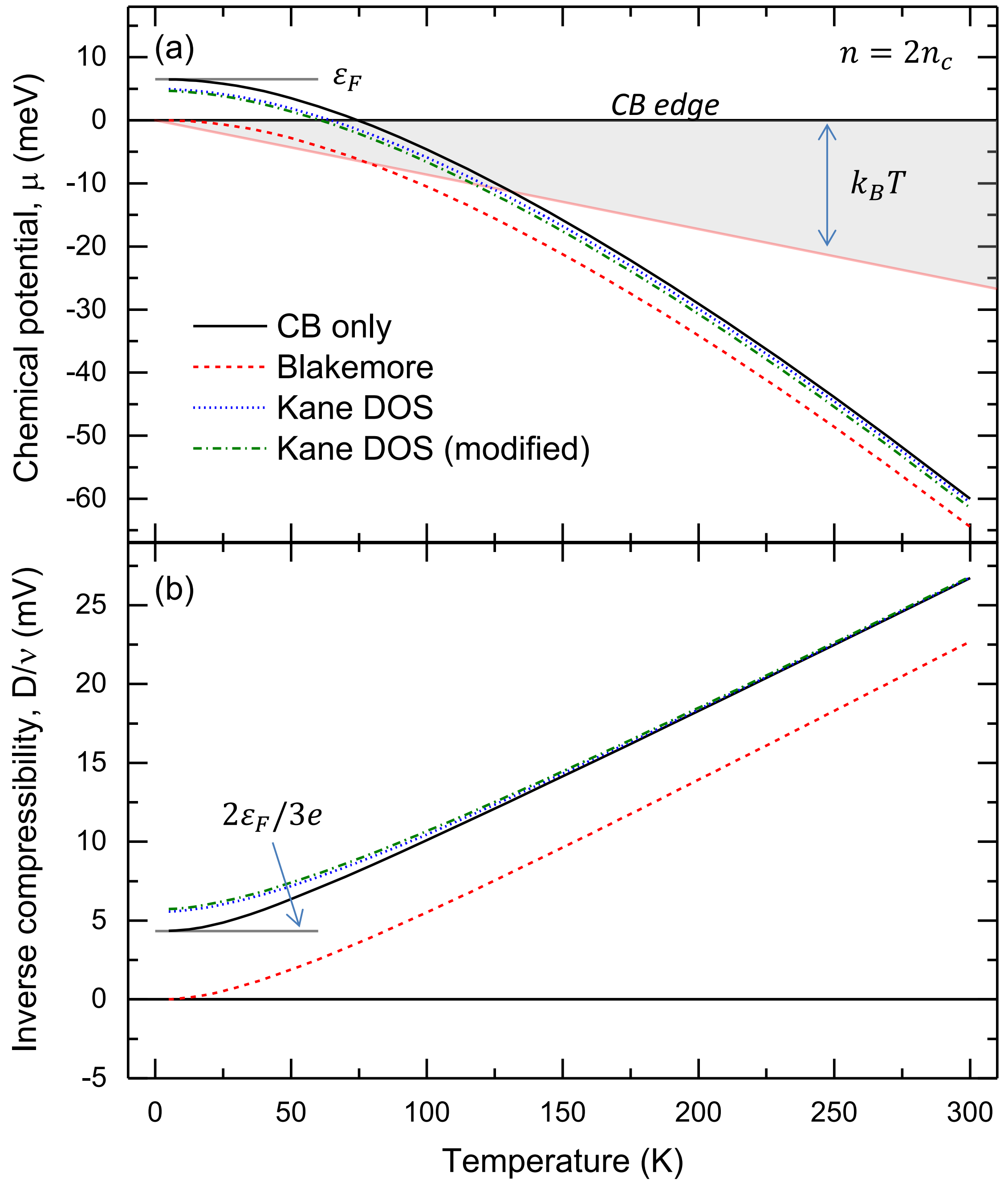

Figure 2.3: (a) Chemical potential vs. temperature and (b) inverse compressibility vs. temperature for the models described in the text.

be re-visited in Chap. 4 in the context of understanding how large spin polarizations may generate asymmetric shifts in the electrochemical potentials.

2.3.3.1 Band-tail: Blakemore model

Blakemore [35] introduced perhaps the simplest first step towards including the influence of impurity states above the transition. His approach was to simply add a delta function to the density of states at the bottom of the conduction band. This approach allows easy calculation of the number of ionized donors, particularly in the non-degenerate limit. As expected, this also lowers the electrochemical potential relative to the conduction band-only model as shown in 2.3(a). However, for our purposes, this model suffers from the major drawback of not accounting for the reduction of the density of states in the conduction band itself. Because of this the compressibility exhibits a large offset relative to the other models. The validity of this model at higher dopings has also been questioned[36]. Including full account of the degree of degeneracy, we obtain the following expressions:

$$g_{BM}(\varepsilon) = \frac{(2m^\star)^{3/2}}{2\hbar^3\pi^2}\varepsilon^{1/2} + n\delta(\xi) \tag{2.18}$$

$$n_{BM} = n_Q(T)\mathcal{F}_{1/2}(\xi)\left(-\coth\frac{\xi}{2}\right) \tag{2.19}$$

$$\kappa_{BM} = \frac{n_Q(T)}{k_B T}\left[\mathcal{F}_{-1/2}(\xi)\left(-\coth\frac{\xi}{2}\right) + \mathcal{F}_{1/2}(\xi)\left(\frac{1}{2}\text{csch}^2\frac{\xi}{2}\right)\right] \tag{2.20}$$

$$\frac{\partial\kappa_{BM}}{\partial\mu} = \frac{n_Q(T)}{(k_B T)^2}\left[\mathcal{F}_{-3/2}(\xi)\left(-\coth\frac{\xi}{2}\right) + 2\mathcal{F}_{-1/2}(\xi)\left(\frac{1}{2}\text{csch}^2\frac{\xi}{2}\right)\right. \tag{2.21}$$

$$\left. + \mathcal{F}_{1/2}(\xi)\left(-\coth\frac{\xi}{2}\right)\left(\frac{1}{2}\text{csch}^2\frac{\xi}{2}\right)\right]. \tag{2.22}$$

2.3.3.2 Band-tail: Kane DOS model

A more accurate model for the density of states in the band tail was introduced by Kane[37] which preserves the total number of available states in the conduction band. His derivation, discussed further in Refs. [38, 39], considers shifts in the density of states due to local screening of randomly positioned Coulomb potentials. This gives rise to the functional form:

$$g_{K0}(\varepsilon) = \frac{(2m^\star)^{3/2}}{2\hbar^3\pi^2}\gamma^{1/2}G_0\left(\frac{\varepsilon}{\gamma}\right) \tag{2.23}$$

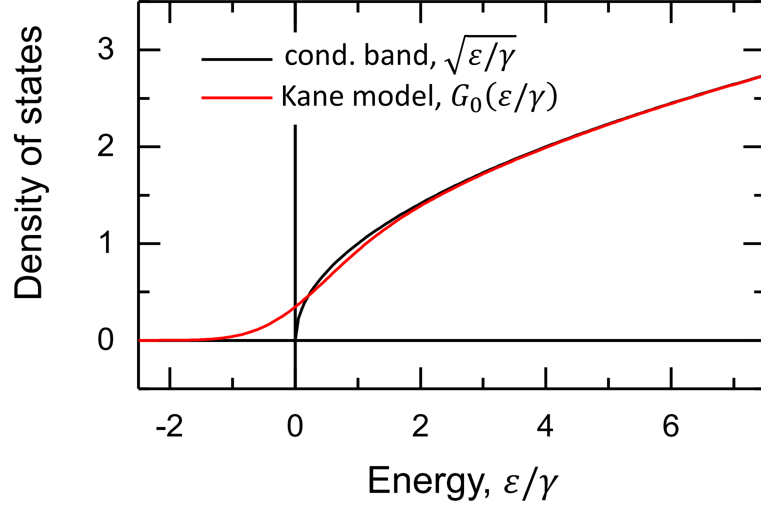

Figure 2.4: Density of states vs. energy

where G_0 is a dimensionless function given by

$$G_0(X) = \frac{1}{\sqrt{\pi}} \int_{-\infty}^{X} e^{-y^2} (X - y)^{1/2} \, dy. \tag{2.24}$$

Here γ denotes an energy scale describing the width of the disorder:

$$\gamma = \varepsilon_B 4\pi^{1/2} \left(a_B^2 r n\right)^{1/2}, \tag{2.25}$$

where the screening length r is related to the compressibility as

$$r = \left(\frac{4\pi\hbar}{m^\star a_B}\kappa\right)^{-1/2} \tag{2.26}$$

In the degenerate limit, this reduces to the usual Thomas-Fermi expression from which we obtain

$$\gamma_0 = \varepsilon_B 2\sqrt{2\pi} \left(\frac{\pi}{3}\right)^{1/12} \left(n a_B^3\right)^{5/12}. \tag{2.27}$$

The Kane DOS is compared to that of the conduction band-only model in Fig 2.4. The remaining quantities of interest may be obtained by numerical integration as

$$n_{K0} = \int_{-\infty}^{+\infty} \frac{g_{K0}(\varepsilon) \, d\varepsilon}{e^{(\varepsilon - \mu)/k_B T} + 1} \tag{2.28}$$

$$\kappa_{K0} = \int_{-\infty}^{+\infty} \frac{g'_{K0}(\varepsilon) \, d\varepsilon}{e^{(\varepsilon - \mu)/k_B T} + 1} \tag{2.29}$$

$$\frac{\partial \kappa_{K0}}{\partial \mu} = \int_{-\infty}^{+\infty} \frac{g''_{K0}(\varepsilon)\, d\varepsilon}{e^{(\varepsilon-\mu)/k_B T} + 1}. \tag{2.30}$$

Here we have utilized the results of Appendix A.1 to transfer the derivatives with respect to chemical potential inside the integration.

2.3.3.3 Band-tail: Modified Kane DOS

The Kane DOS model was derived using the Thomas-Fermi screening length which assumes perfect degeneracy. However, as the temperature increases, the system become less compressible and the ability of the carriers to screen the random Coulomb potential is diminished. To account for an arbitrary degree of degeneracy in the Kane DOS model amounts to setting γ equal to

$$\gamma = \gamma_0 \left(\frac{\kappa_{K0}}{\kappa}\right)^{1/4}, \tag{2.31}$$

where κ is the compressibility. This must be solved self-consistently, since κ itself depends on γ through the position of the chemical potential ξ.

2.4 Energy dependence of the momentum relaxation time

Because the mobility is a property derived from the non-equilibrium distribution function, calculating quantities which require an average of the momentum relaxation time *cannot* be averaged in the usual manner, i.e.

$$\langle \tau \rangle \neq \frac{1}{n} \int_{-\infty}^{\infty} \tau(\varepsilon)\, g(\varepsilon)\, f(\varepsilon - \mu)\, d\varepsilon. \tag{2.32}$$

The proper average over the Fermi surface is given by[31, 40]

$$\langle \tau \rangle = \frac{\int_{-\infty}^{\infty} \tau(\varepsilon)\, \varepsilon g(\varepsilon)\, f'(\varepsilon - \mu)\, d\varepsilon}{\int_{-\infty}^{\infty} \varepsilon g(\varepsilon)\, f'(\varepsilon - \mu)\, d\varepsilon}. \tag{2.33}$$

For a parabolic dispersion $g(\varepsilon) \propto \varepsilon^{1/2}$ and energy dependent relaxation time of the form $\tau(\varepsilon) = a\varepsilon^s$, we obtain

$$\langle \tau \rangle = a\,(k_B T)^s \frac{\Gamma\left(\frac{5}{2} + s\right) \mathcal{F}_{\frac{1}{2}+s}(\xi)}{\Gamma\left(\frac{5}{2}\right) \mathcal{F}_{\frac{1}{2}}(\xi)}. \tag{2.34}$$

This expression will be used in Sec. 3.3.2 to calculate spin lifetimes as well as in Sec. 4.8 to estimate the energy dependence of the mobility on spin diffusion rates. The prefactor a may be estimated from experimental values for either the Hall mobility or magnetoresistance mobility.

The Hall mobility ν_H is related to the drift mobility ν by[31]

$$\nu_H = r\nu = \frac{e\left\langle \tau^2 \right\rangle}{m^\star \left\langle \tau \right\rangle}, \tag{2.35}$$

where the Hall factor

$$r = \frac{\left\langle \tau^2 \right\rangle}{\left\langle \tau \right\rangle^2} = \frac{\Gamma\left(\frac{5}{2}+2s\right)\mathcal{F}_{\frac{1}{2}+2s}\left(\xi\right)}{\left[\Gamma\left(\frac{5}{2}+s\right)\mathcal{F}_{\frac{1}{2}+s}\left(\xi\right)\right]^2} \tag{2.36}$$

encodes information about the energy dependence of the scattering process. Using Eq. 2.34, we obtain

$$a = \left(\frac{m^\star \nu_H}{e}\right)\frac{\left\langle \varepsilon^s \right\rangle}{\left\langle \varepsilon^{2s} \right\rangle} = \left(\frac{m^\star \nu_H}{e}\right)\left(k_B T\right)^{-s}\frac{\Gamma\left(\frac{5}{2}+s\right)\mathcal{F}_{\frac{1}{2}+s}\left(\xi\right)}{\Gamma\left(\frac{5}{2}+2s\right)\mathcal{F}_{\frac{1}{2}+2s}\left(\xi\right)}. \tag{2.37}$$

Similar information may also be obtained from the magnetoresistance mobility ν_{MR} defined by

$$\frac{\Delta\rho}{\rho} = \left(\nu_{MR} B\right)^2 \tag{2.38}$$

It may be shown that the magnetoresistance mobility is related to the Hall mobility as[31]

$$\left(\frac{\nu_{MR}}{\nu_H}\right)^2 = \frac{\left\langle \tau^3 \right\rangle \left\langle \tau \right\rangle}{\left\langle \tau^2 \right\rangle^2} - 1 = \frac{\Gamma\left(\frac{5}{2}+3s\right)\Gamma\left(\frac{5}{2}+s\right)}{\left[\Gamma\left(\frac{5}{2}+2s\right)\right]^2}\frac{\mathcal{F}_{\frac{1}{2}+3s}\left(\xi\right)\mathcal{F}_{\frac{1}{2}+s}\left(\xi\right)}{\left[\mathcal{F}_{\frac{1}{2}+2s}\left(\xi\right)\right]^2}. \tag{2.39}$$

While ionized impurity scattering is thought to be the dominant scattering mechanism in n-GaAs at liquid nitrogen temperatures and below, Eqs. 2.36 and 2.39 provide an experimental route towards extracting the energy dependence of the momentum relaxation time $\tau \propto \varepsilon^s$. The carrier concentration is assumed to be constant as a function of temperature and that the Hall factor is unity at room temperature due to the dominance of polar optical phonon scattering[4]. This allows the Hall factor to be determined at each temperature (as shown earlier in Fig. 2.2(e)). We then solve Eq. 2.36 numerically to obtain the effective energy exponent s characterizing the dominant scattering process. The results are shown as the solid lines in Fig. 2.5 for samples with three different carrier concentrations. The same procedure may be repeated using the magnetoresistance expression in Eq. 2.39, which yields the dashed lines in Fig. 2.5. Although this has the advantage of not requiring any assumptions about the Hall factor, Eq. 2.39 is not valid for temperatures less than 40 K due to the onset of weak localization. The results shown in Fig. 2.5 indicate that (1) the

[4]The situation is more complicated than implied here. See Refs. [41, 42] for further discussion. This assumption yields results which are consistent with those plotted in [43].

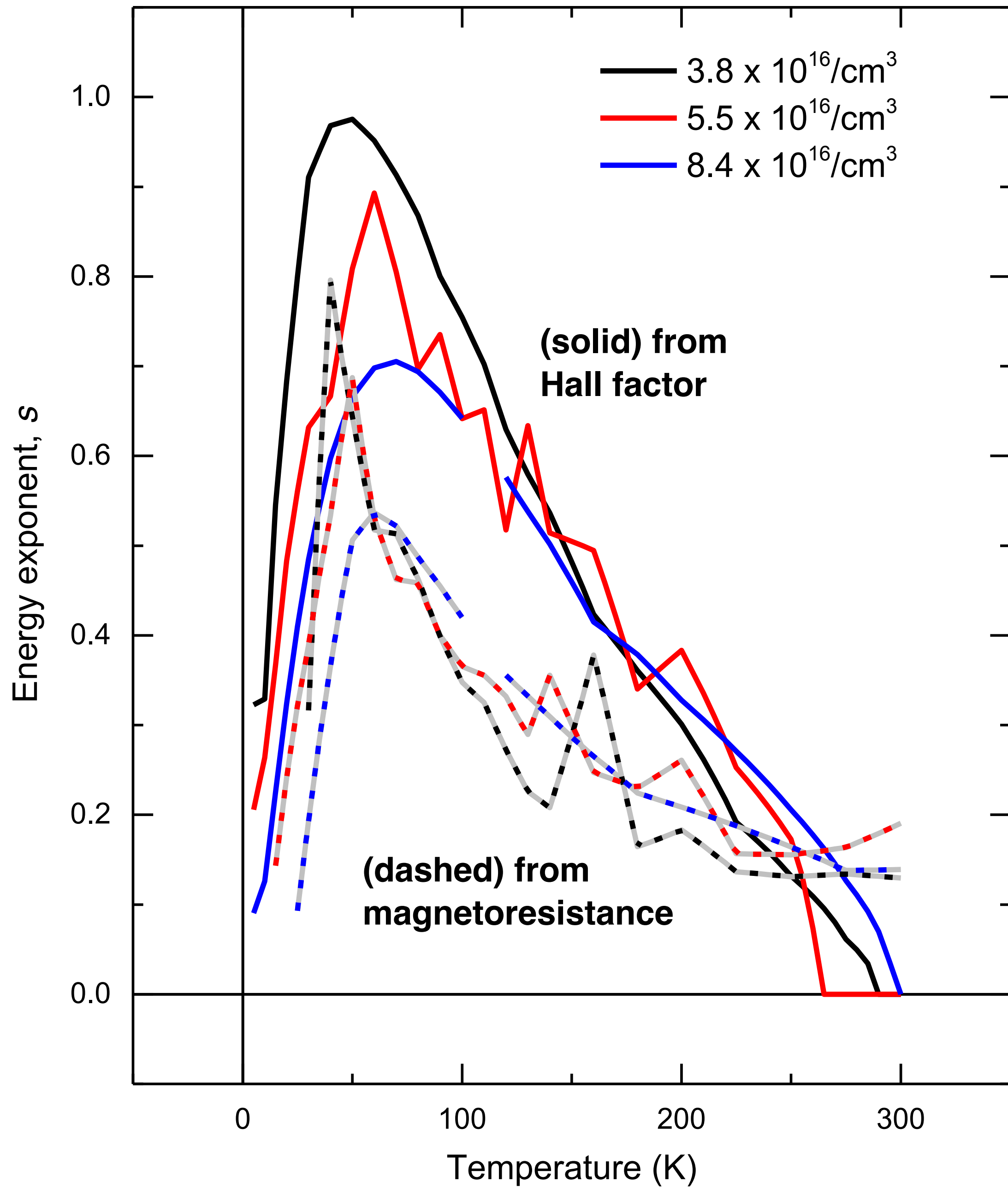

Figure 2.5: Energy exponent vs. temperature obtained from Hall factor (solid lines) and magnetoresistance (dashed lines) for three different carrier concentrations: $3.8 \times 10^{16}/\mathrm{cm}^3$ (black, sample UMN023), $5.5 \times 10^{16}/\mathrm{cm}^3$ (red, sample UMN019), $8.4 \times 10^{16}/\mathrm{cm}^3$ (blue, sample UMN026).

dominant scattering mechanism is mostly independent of doping and (2) the energy dependence of the mobility is likely weaker than $\varepsilon^{+3/2}$ assumed for ionized impurity scattering $s = +3/2$.

Chapter 3

Electrical spin injection and detection

In Sec. 3.1, we generalize the arguments of Sec. 2.3 to include the spin degree of freedom and derive a general continuity equation relating the quantities of spin currents and number polarizations. We further specify how to include the effects of an applied magnetic field. In Sec. 3.2 we present several important device models as a means of introducing the relevant physics necessary to understand our experiments. The concept of 'spin-resistances' is introduced to deal with multi-terminal devices. In Sec. 3.3 we apply these models to the case of the non-local Hanle experiment to obtain spin-lifetimes and diffusion constants in good agreement with theoretical predictions.

3.1 Theory of diffusive spin-transport

In this section we derive the primary relations governing the drift and diffusion of a spin-polarized ensemble in the semi-classical regime. While much of the relevant physics can be reproduced by simply assuming two independent copies of the drift-diffusion expression for the charge current density (Eq. 2.7), the more complete derivation presented below serves two main purposes. First, it allows us to clearly state the assumptions which are most appropriate for the systems under investigation. Second, prior derivations[44, 45, 46, 47] acknowledge yet do not include a full account of the high polarization limit, i.e. how the system evolves as the polarization is driven very far from equilibrium. Due to the machinery developed in Sec. 2.3, we are in a unique position to numerically estimate the influence of large polarizations on the relevant transport coefficients.

Large polarization effects are relevant to our systems for the following reasons. Unlike

metallic systems, semiconducting channels can sustain a substantial electric field which allows the spin polarization in the channel to be spatially redistributed. This typically results in the spin polarization being highly concentrated in the immediate vicinity of the forward biased injector contact. In combination with these drift effects, the recent development of highly spin-polarized Heusler alloy ferromagnets ($Co_2Mn_{1-x}Fe_xSi$) allows us to routinely achieve polarizations in excess of 50%, beyond which the validity of the simpler models is questionable. The language developed in this section will allow a more complete discussion in Ch. 4 where such large polarizations give rise to an additional source of electromotive force analogous to the Seebeck effect.

3.1.1 Current densities

We start by assuming a local, linear relationship between the current densities $\vec{j}_\alpha$ and *electrochemical* potentials ζ_α for each spin species ($\alpha = \uparrow$ or $\downarrow$). This may be expressed as[45]

$$e\vec{j}_\alpha = \sigma_{\alpha\beta}\vec{\nabla}\zeta_\beta, \tag{3.1}$$

where $\sigma_{\alpha\beta}$ is the low-frequency conductivity matrix of the material[1]. The *electrochemcial* potential ζ_α may be further decomposed into *chemical* and *electrostatic* contributions as

$$\zeta_\alpha = \mu_\alpha - e\phi. \tag{3.2}$$

Here, as in Sec. 2.3, we define the chemical potential μ_α of spin species α as

$$\mu_\alpha = \frac{\partial F\left(n_\uparrow, n_\downarrow\right)}{\partial n_\alpha}. \tag{3.3}$$

F denotes the local free energy density, which depends on the electron concentrations of both spin species. Using the chain rule $\vec{\nabla}\mu_\beta = \left(\partial\mu_\beta/\partial n_\gamma\right)\vec{\nabla}n_\gamma$, Eq. 3.1 can be written as

$$\vec{j}_\alpha = \sum_{\beta=\uparrow,\downarrow}\sigma_{\alpha\beta}\left[\frac{1}{e}\frac{\partial\mu_\beta}{\partial n_\gamma}\vec{\nabla}n_\gamma - \vec{\nabla}\phi\right] \tag{3.4}$$

$$= \sum_{\beta=\uparrow,\downarrow}\left[eD_{\alpha\beta}\vec{\nabla}n_\beta - \sigma_{\alpha\beta}\vec{\nabla}\phi\right], \tag{3.5}$$

[1]To be explicit, $\sigma_{\alpha\beta}$ indicates the current of α-oriented electrons which flow due to a gradient in the electrochemical potential of β-oriented electrons. Unless otherwise noted, we assume the Einstein convention of summing over repeated indices.

where the diffusivity matrix $D_{\alpha\beta}$ is defined by the generalized Einstein relation

$$e^2 D_{\alpha\beta} = \sigma_{\alpha\gamma}\frac{\partial\mu_\gamma}{\partial n_\beta} = \sigma_{\alpha\gamma}S_{\gamma\beta}. \tag{3.6}$$

The quantity $S_{\gamma\beta} = \partial^2 F/\partial n_\gamma \partial n_\beta$ is known as the spin-stiffness matrix, and allows the system to be parameterized to account for the influence of exchange ($S_{\uparrow\downarrow} \neq 0$) and spin Coulomb drag ($\sigma_{\uparrow\downarrow} \neq 0$) effects[48, 45, 47].

To simplify these expressions for the following discussion, we assume that the spin-up and spin-down channels behave completely independently, i.e. that both the conductivity and spin-stiffness matrices are diagonal:

$$\sigma_{\alpha\beta} = \delta_{\alpha\beta}\sigma_\alpha \tag{3.7}$$

$$S_{\gamma\beta} = \delta_{\alpha\beta}\frac{\partial\mu_\alpha}{\partial n_\alpha} = \delta_{\alpha\beta}e^2 D_\alpha/\sigma_\alpha. \tag{3.8}$$

This allows us to write drift-diffusion equations for each spin channel independently as

$$\vec{j}_\uparrow = eD_\uparrow\vec{\nabla}n_\uparrow - \sigma_\uparrow\vec{\nabla}\phi \tag{3.9a}$$
$$\vec{j}_\downarrow = eD_\downarrow\vec{\nabla}n_\downarrow - \sigma_\downarrow\vec{\nabla}\phi. \tag{3.9b}$$

These expressions will be used in the next section to derive relations governing the behavior of both charge and spin currents.

It is important to note here that this formalism contains the implicit assumption that the spin current is carried only by itinerant electrons. While this assumption is appropriate for our systems, as will be demonstrated in Sec. 3.3, this does not hold in general. Particularly for low doped systems, one can imagine a situation where the exchange coupling between adjacent donor-bound electrons gives rise to a significantly higher spin diffusion rate than predicted by the Einstein relation for itinerant carriers. This was one of the main conclusions of the optical pumping experiments in Ref. [33] on n-GaAs at a doping level of $n = 1.4 \times 10^{16}/\mathrm{cm}^3 \approx 1.7 n_c$. However, as we noted in Sec. 2.3.1, the authors applied the wrong form of the Einstein relation, which introduced an underestimation of their charge mobility by a factor of ≈ 3.5 at low temperatures. After correcting for the error in their calculations, it appears that at 7.5 K the spin diffusivity is still roughly twice that implied by the charge transport measurements. Our measurements are performed at slightly higher doping levels in a range of temperatures where the assumption that the charge and spin diffusivities are the same is valid.

3.1.2 Polarized drift and diffusion

To more conveniently describe the non-equilibrium state, we introduce the total carrier concentration and fractional number polarization as

$$n = n_\uparrow + n_\downarrow \tag{3.10a}$$

$$p = \left(n_\uparrow - n_\downarrow\right)/n, \tag{3.10b}$$

such that the deviation from equilibrium concentrations is simply $\delta n_\alpha = n_\alpha - n/2 = \alpha np/2$. Following Yu and Flatté [44], we write down continuity equations for $\delta n_\uparrow$ and $\delta n_\downarrow$:

$$\frac{\partial \delta n_\uparrow}{\partial t} = -\frac{\delta n_\uparrow}{\tau_{\uparrow\downarrow}} + \frac{\delta n_\downarrow}{\tau_{\downarrow\uparrow}} + \frac{1}{e}\vec{\nabla}\cdot\vec{j}_\uparrow \tag{3.11a}$$

$$\frac{\partial \delta n_\downarrow}{\partial t} = -\frac{\delta n_\downarrow}{\tau_{\downarrow\uparrow}} + \frac{\delta n_\uparrow}{\tau_{\uparrow\downarrow}} + \frac{1}{e}\vec{\nabla}\cdot\vec{j}_\downarrow. \tag{3.11b}$$

where $\tau_{\uparrow\downarrow}^{-1}$ denotes the spin-flip rate from $\uparrow$ to $\downarrow$. Upon shifting to the variables n and p and rearranging, we obtain

$$\frac{1}{2}\frac{\partial p}{\partial t} = -\frac{p}{2}\left(\frac{1}{\tau_{\uparrow\downarrow}} + \frac{1}{\tau_{\downarrow\uparrow}}\right) + \frac{1}{ne}\vec{\nabla}\cdot\vec{j}_\uparrow \tag{3.12a}$$

$$-\frac{1}{2}\frac{\partial p}{\partial t} = \frac{p}{2}\left(\frac{1}{\tau_{\downarrow\uparrow}} + \frac{1}{\tau_{\uparrow\downarrow}}\right) + \frac{1}{ne}\vec{\nabla}\cdot\vec{j}_\downarrow, \tag{3.12b}$$

where we have assumed $\partial n/\partial t = 0$. Adding and subtracting these two expressions yields

$$0 = \vec{\nabla}\cdot\left(\vec{j}_\uparrow + \vec{j}_\downarrow\right) \tag{3.13a}$$

$$\frac{\partial p}{\partial t} = -\frac{p}{\tau_s} + \frac{1}{ne}\vec{\nabla}\cdot\left(\vec{j}_\uparrow - \vec{j}_\downarrow\right). \tag{3.13b}$$

where $\tau_s^{-1} = \tau_{\uparrow\downarrow}^{-1} + \tau_{\downarrow\uparrow}^{-1}$ is the spin relaxation rate. These expressions highlight the more natural variables as being charge and spin currents, defined respectively as

$$\vec{j} = \vec{j}_\uparrow + \vec{j}_\downarrow \tag{3.14a}$$

$$\vec{q} = \vec{j}_\uparrow - \vec{j}_\downarrow. \tag{3.14b}$$

We have chosen here to express the spin current in the same units as the charge current, although (several) other conventions are possible[49]. Eq. 3.13b defines a continuity equation for spin, which includes a relaxation term in addition to the divergence of the spin current.

Under steady-state conditions ($\partial \delta n_\alpha / \partial t = 0$, i.e. $\partial p/\partial t = 0$), Eqs. 3.13a and 3.13b become

$$\vec{\nabla} \cdot \vec{j} = 0 \tag{3.15a}$$

$$\vec{\nabla} \cdot \vec{q} = nep/\tau_s. \tag{3.15b}$$

We would now like to find a relationship between $\vec{j}$ and $\vec{q}$. Using the definitions in Eqs. 3.9a and Eq. 3.9b, we may write

$$\vec{j} = (\sigma_\uparrow + \sigma_\downarrow)\, \vec{E} + eD_\uparrow \vec{\nabla} n_\uparrow + eD_\downarrow \vec{\nabla} n_\downarrow \tag{3.16a}$$

$$\vec{q} = (\sigma_\uparrow - \sigma_\downarrow)\, \vec{E} + eD_\uparrow \vec{\nabla} n_\uparrow - eD_\downarrow \vec{\nabla} n_\downarrow. \tag{3.16b}$$

In most experiments, $\vec{j}$ is held constant. Eliminating $\vec{E}$ from these two expressions and taking the local charge neutrality approximation[2] $\left(\vec{\nabla} n = 0\right)$ yields

$$\vec{q} = \left(\frac{\sigma_\uparrow - \sigma_\downarrow}{\sigma_\uparrow + \sigma_\uparrow}\right) \vec{j} + en \left(\frac{\sigma_\downarrow D_\uparrow + \sigma_\uparrow D_\downarrow}{\sigma_\uparrow + \sigma_\downarrow}\right) \vec{\nabla} p = \tilde{p}\vec{j} + en\tilde{D}\vec{\nabla} p \tag{3.17}$$

where we have defined the conductivity polarization as

$$\tilde{p} = \frac{\sigma_\uparrow - \sigma_\downarrow}{\sigma_\uparrow + \sigma_\downarrow} = \Lambda p = \frac{1+\Xi}{1+\Xi p^2} p \tag{3.18}$$

and effective diffusion constant

$$\tilde{D} = \frac{\sigma_\downarrow D_\uparrow + \sigma_\uparrow D_\downarrow}{\sigma_\uparrow + \sigma_\downarrow} = D\left(1 - \Lambda \Theta p^2\right), \tag{3.19}$$

with $D = (D_\uparrow + D_\downarrow)/2$. The parameters Ξ and Γ are described below.

Assuming a Drude form for the conductivity $\sigma_\alpha = \frac{1}{2} n (1 + \alpha p)\, e \nu_\alpha$, we have introduced Ξ to parameterize the rate at which the mobility ν changes with energy. For systems in which the mobility may be approximated as being energy-independent ($\Xi \approx 0$), the conductivity polarization is equal to the number polarization, i.e. $\Lambda \approx 1$. However, in n-GaAs, at liquid nitrogen temperatures, the dominant scattering mechanism is ionized impurity scattering which has an energy dependent momentum relaxation time of $\tau_p \propto \varepsilon^{3/2}$. The reduced scattering cross-section at higher energies means that electrons in the majority spin channel will have a higher mobility. Using the results of Sec. 2.4 for a parabolic dispersion, this can

[2] Refs. [31, 44, 48, 45] all note that to avoid a serious loss of accuracy, care must be taken not to impose this condition too early. Typically, the first step is to eliminate the $\vec{\nabla} \cdot \vec{E}$ terms appearing in the continuity Eqs. 3.11a and 3.11b. We take the more direct approach of re-writing the spin current $\vec{q}$ to depend on $\vec{j}$ rather than $\vec{E}$ *before* insertion into the continuity equations (Eqs. 3.13a and 3.13b). The end result is the same.

be expressed as (see Appendix A.3):

$$\Xi = \frac{\nu_\uparrow - \nu_\downarrow}{\nu_\uparrow + \nu_\downarrow}\frac{1}{p} \approx \frac{\partial\nu/\partial n}{\nu/n} = \frac{\mathcal{F}_{-\frac{1}{2}+s}(\xi)/\mathcal{F}_{-\frac{1}{2}}(\xi)}{\mathcal{F}_{\frac{1}{2}+s}(\xi)/\mathcal{F}_{\frac{1}{2}}(\xi)} - 1, \tag{3.20}$$

where $\xi = \mu/k_BT$ denotes the reduced chemical potential as before and s indicates the energy dependence of the momentum relaxation time $\tau_p(\varepsilon) \propto \varepsilon^s$. Following a similar procedure to obtain the energy dependence of the diffusion constant yields

$$\Theta = \frac{D_\uparrow - D_\downarrow}{D_\uparrow + D_\downarrow}\frac{1}{p} \approx \frac{e}{\nu}\frac{\partial D}{\partial\mu} = \Xi + 1 - \frac{\mathcal{F}_{1/2}(\xi)\,\mathcal{F}_{-3/2}(\xi)}{\left[\mathcal{F}_{-1/2}(\xi)\right]^2}. \tag{3.21}$$

In the non-degenerate limit, both $\Xi = 0$ and $\Theta = 0$ since $\mathcal{F}_\alpha(\xi) \to e^\xi$. In the degenerate limit where $\mathcal{F}_\alpha(\xi) \to \xi^{\alpha+1}/\Gamma[\alpha+2]$, we have

$$\Xi = \frac{\Gamma\left[\frac{5}{2}+s\right]/\Gamma\left[\frac{5}{2}\right]}{\Gamma\left[\frac{3}{2}+s\right]/\Gamma\left[\frac{3}{2}\right]} - 1 \tag{3.22}$$

$$\Theta = \frac{\Gamma\left[\frac{5}{2}+s\right]/\Gamma\left[\frac{5}{2}\right]}{\Gamma\left[\frac{3}{2}+s\right]/\Gamma\left[\frac{3}{2}\right]} - \frac{1}{3}. \tag{3.23}$$

Fig. 3.1 shows the temperature dependence of Ξ and Θ for several different concentrations. The solid curves denoting the behavior for ionized impurity scattering ($s = 3/2$) are the most relevant for our experiments.

Fig. 3.2 shows the variation of $\tilde{p}$ and $\tilde{D}$ as functions of the fractional number polarization p. Note that even in the low polarization limit ($p \ll 1$), the energy dependence of the mobility has an appreciable impact on the magnitude of the drift contribution to the spin current. We further note that these parameters have an influence on the charge transport. It is insightful to rewrite the charge current density (Eq. 3.16a) in terms of these new variables:

$$\begin{aligned} \vec{j} &= (\sigma_\uparrow + \sigma_\downarrow)\vec{E} + e\left(\frac{D_\uparrow - D_\downarrow}{2}\right)n\vec{\nabla}p && (3.24)\\ &= \sigma\left(1+\Xi p^2\right)\vec{E} + enD\Theta p\vec{\nabla}p && (3.25)\\ &= \tilde{\sigma}\vec{E} + \frac{1}{2}enD\Theta\vec{\nabla}\left(p^2\right) && (3.26) \end{aligned}$$

where $\sigma = ne\nu$ and $\tilde{\sigma}/\sigma = 1 + \Xi p^2$. Notice that the first term predicts that the charge conductivity $\tilde{\sigma}$ should increase in the presence of a spin accumulation as shown in Fig. 3.2. For the second term, we have invoked the chain rule $p\vec{\nabla}p = \frac{1}{2}\vec{\nabla}\left(p^2\right)$. This second

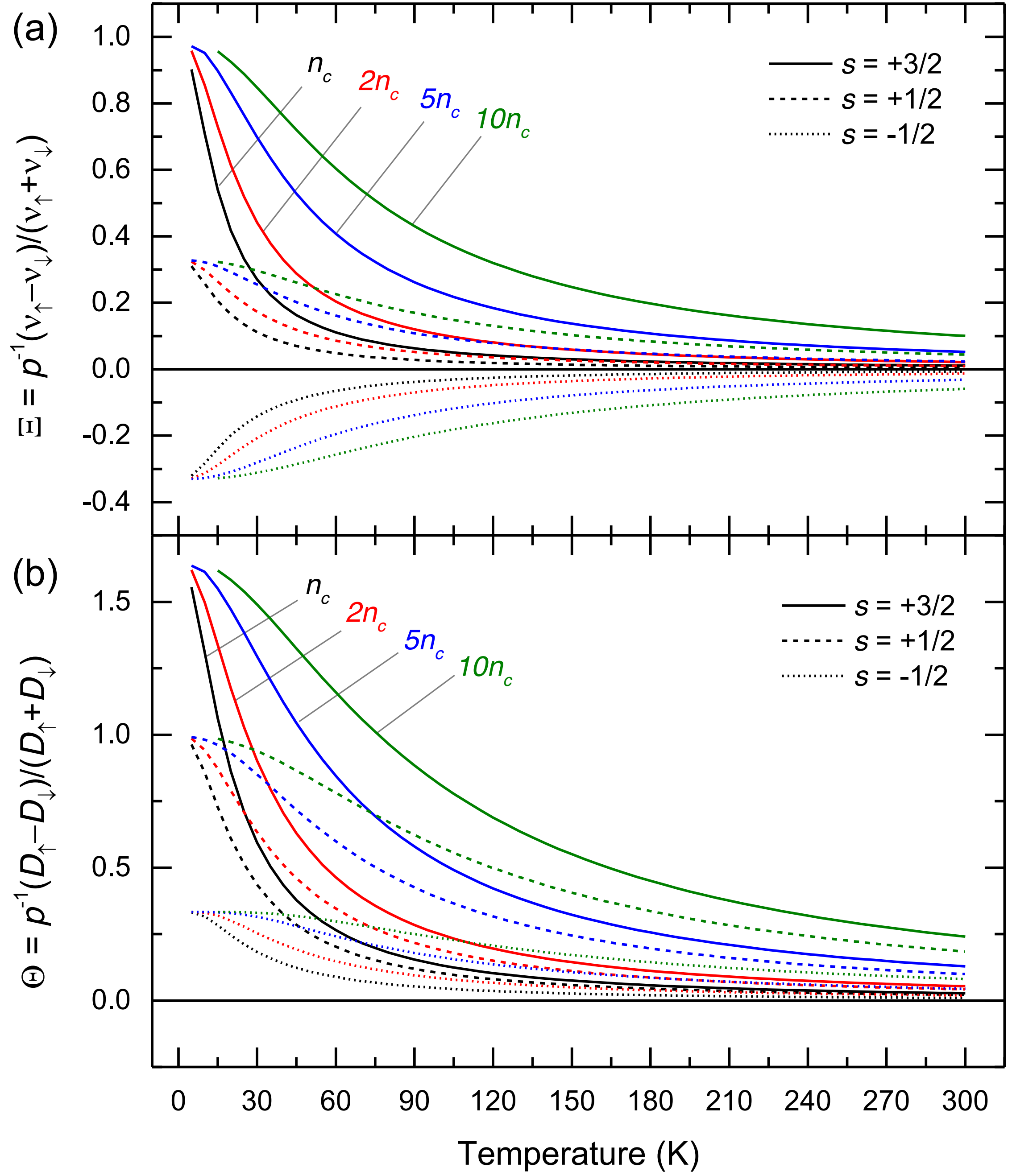

Figure 3.1: Energy dependence of the (a) mobility and (b) diffusion constant as a function of temperature, normalized by the polarization. Solid, dashed, and dotted curves correspond to scattering exponents of $+\frac{3}{2}$ (ionized impurity), $+\frac{1}{2}$ (acoustic phonon, piezoelectric), and $-\frac{1}{2}$ (acoustic phonon, deformation potential) respectively.

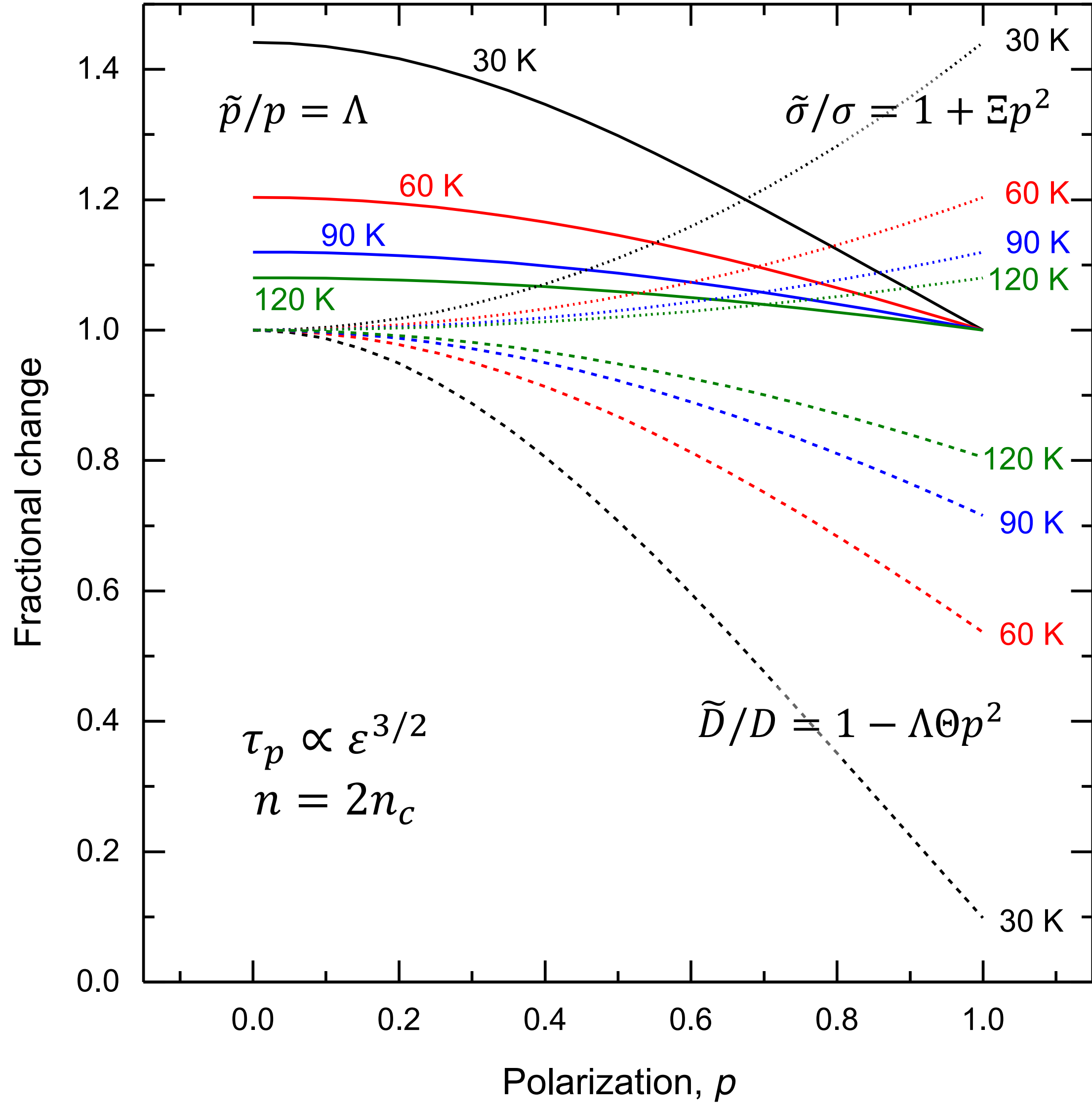

Figure 3.2: Polarization dependence of the conductivity polarization (solid), diffusion constant (dashed), and charge conductivity (dotted). These curves were evaluated at a concentration of $n = 2n_c$ assuming a scattering exponent of 3/2 (ionized impurity scattering).

term may be regarded as a source of electromotive force generated by the steady-state spin accumulation, which is the subject of Ch. 4.

3.1.3 Small polarization limit

We now take the small polarization limit of Eq. 3.17 ($\Xi = 0$, $\Gamma = 0$, $\Lambda = 1$,$\Theta = 0$) as

$$\vec{q} = p\vec{j} + enD\vec{\nabla}p \tag{3.27}$$

Inserting Eq. 3.27 into the continuity expression (Eq. 3.13b) yields

$$\frac{\partial p}{\partial t} = -\frac{p}{\tau_s} + \vec{v}\cdot\vec{\nabla}p + D\nabla^2 p, \tag{3.28}$$

where $\vec{v} = \vec{j}/ne$ is the drift velocity. Solving Eq. 3.28 involves taking the steady-state limit ($\partial p/\partial t = 0$) and applying a constant source of spin injection as a Neumann boundary condition. However, it is often useful to specify a local source of spin injection within the volume of the device. Consider a constant spin current q_0 flowing across a cross-sectional area A into a box of volume Ah. We then have

$$\left(\frac{\partial p}{\partial t}\right)_{\text{inject}} = \frac{\text{\# imbalance per unit time}}{\text{\# of electrons in volume}} = \frac{q_0 A/(-e)}{nAh} = -\frac{q_0}{neh}, \tag{3.29}$$

where h is the thickness of the volume into which the spins are injected. Note that in the presence of a magnetic field, it is also necessary to specify the orientation $\hat{\eta}$ of the injected spins.

3.1.4 Homogeneous magnetic field

We now discuss how to add the effects of an applied (or effective) magnetic field to the continuity equation. The Larmor precession term is given by

$$\left(\frac{\partial \vec{p}}{\partial t}\right)_{\text{precess}} = -\gamma\vec{B}\times\vec{p} \tag{3.30}$$

where $\gamma = -g^\star e/2m_e = -g^\star\mu_B/\hbar$ is the gyromagnetic ratio and $g^\star$ is the effective g-factor. For GaAs, $g^\star = -0.44$ and $\gamma = 6.2\ (2\pi\ \text{rad})\,\text{GHz/T}$. We ignore the influence of any associated Lorentz forces since the Hall angle is small for all field scales of interest, i.e. $\nu/\gamma\tau_s \ll 1$. We assume that the magnetic field is homogeneous across the device, and that the orientation of the injected spins has been specified as $\hat{\eta}$. This allows an orthonormal basis to be defined consisting of the three directions $\hat{B}$, $\hat{\eta}\times\hat{B}$, and $\hat{B}\times\left(\hat{\eta}\times\hat{B}\right)$. Spins

parallel to the magnetic field $\left(p_{\parallel}=\vec{p}\cdot\hat{B}\right)$ do not precess and evolve according to

$$\frac{\partial p_{\parallel}}{\partial t}=-\frac{p_{\parallel}}{\tau_s}+\vec{v}\cdot\vec{\nabla}p_{\parallel}+D\nabla^2 p_{\parallel}-\frac{q_0}{neh}\left(\hat{\eta}\cdot\vec{B}\right). \tag{3.31}$$

For spins perpendicular to the magnetic field, the two remaining orthogonal directions may be mapped to the complex plane as[3]

$$p=\vec{p}\cdot\left[\hat{B}\times\left(\hat{\eta}\times\hat{B}\right)\right]+i\vec{p}\cdot\left(\hat{\eta}\times\hat{B}\right). \tag{3.32}$$

The Larmor precession term then simplifies to

$$\left(\frac{\partial p}{\partial t}\right)_{\text{precess}}=-i\gamma Bp \tag{3.33}$$

such that the continuity equation may be written as

$$\frac{\partial p}{\partial t}=-\frac{p}{\tau_s}+\vec{v}\cdot\vec{\nabla}p+D\nabla^2 p-i\gamma Bp-\frac{q_0}{neh}\left(1-\hat{\eta}\cdot\hat{B}\right) \tag{3.34}$$

By combining the relaxation and precession terms, the magnetic field may be thought of as giving rise to a complex spin-lifetime, $\tau_s/\left(1+i\gamma B\tau_s\right)$.

For more complex situations in which an inhomogeneous magnetic field acts on the electron spin ensemble[4], the number polarization and spin current must be treated as vector and tensor quantities respectively. The continuity equation becomes

$$\frac{\partial p_j}{\partial t}-\frac{1}{ne}\frac{\partial q_{ij}}{\partial x_i}+\frac{p_j}{\tau_s}+\epsilon_{jkl}\gamma B_k p_l = 0 \tag{3.35}$$

with the spin current specified as the tensor

$$q_{ij}=j_i p_j+neD\frac{\partial p_j}{\partial x_i}. \tag{3.36}$$

Here the first index of q_{ij} specifies the flow direction and the second index the spin orientation. Repeated indices imply summation and ϵ_{jkl} is the Levi-Civita symbol.

[3]For example, if the magnetic field is applied along $\hat{z}$ and the spins are injected from a ferromagnet whose magnetization lies along $\hat{\eta}=\hat{x}$, we would have $p_{\parallel}=p_z$ and $p=p_x+ip_y$.

[4]This occurs in the presence of polarized nuclei or ferromagnetic fringe fields for example. This would also be the case for gate-induced spin-orbit fields.

3.2 Drift-diffusion models

In steady-state, Eqs. 3.31 and 3.34 can be written in the more compact form

$$\lambda_s^2 \nabla^2 p_\parallel + \lambda_s \vec{J} \cdot \vec{\nabla} p_\parallel - p_\parallel - Q_0 \frac{\lambda_s}{h} \left(\hat{\eta} \cdot \hat{B} \right) = 0 \tag{3.37}$$

$$\lambda_s^2 \nabla^2 p + \lambda_s \vec{J} \cdot \vec{\nabla} p - (1 + i\gamma B \tau_s) \, p - Q_0 \frac{\lambda_s}{h} \left(1 - \hat{\eta} \cdot \hat{B} \right) = 0 \tag{3.38}$$

where we have defined $\lambda_s = \sqrt{D\tau_s}$ as the spin diffusion length and normalized the current densities as $\vec{J} = \vec{j}/j_s$ and $Q_0 = q_0/j_s$ with the material parameter $j_s = ne\lambda_s/\tau_s = neD/\lambda_s$. Note that if the solution to Eq. 3.38 is known, the solution to Eq. 3.37 immediately follows by setting $B = 0$ and appropriately renormalizing the injection rate. Thus, the examples below only contain solutions for the transverse case (Eq. 3.38) with $\hat{\eta} \perp \hat{B}$.

3.2.1 Spin resistances

Before discussing specific applications of Eq. 3.38, it is useful to first introduce the concept of a 'spin-resistance'[5], which for a given device geometry quantifies how much spin accumulation is generated per unit of injected spin current. The spin-resistance area product $R^{(ij)}$ specifies the spin-splitting $\Delta\mu^{(i)}$ at contact (i) induced by a spin current density $q^{(j)}$ flowing across contact (j):

$$\frac{\Delta\mu^{(i)}}{-e} = R^{(ij)} q^{(j)}. \tag{3.39}$$

We have included a minus sign here so that (in most cases) $R^{(ij)}$ will turn out to be a positive quantity. This is a consequence of our choice in Sec. 3.1.2 to define j and q to have the same units. Since $\Delta\mu/e = 2Dp/\nu$ and $q = j_s Q$, we can write this in dimensionless units as

$$p^{(i)} = \frac{R^{(ij)}}{\rho\lambda_s} Q^{(j)} = -r^{(ij)} Q^{(j)} \tag{3.40}$$

where $\rho = 1/ne\nu$ is the resistivity of the material and $r^{(ij)} = R^{(ij)}/\rho\lambda_s$. To specify these quantities within a multi-terminal device model, we employ parenthetical superscripts to

[5] A word of caution is necessary here regarding addition of the prefix 'spin-' to existing terms such as resistance, voltage, current, Hall, impedance, etc. This creates an ambiguity as to whether this refers to a polarization dependence in an existing observable, or whether a new quantity is being introduced to handle the incremented dimensionality. The existing vocabulary base is often ill-equipped to handle the latter case, particularly in situations where the equilibrium state itself is polarized. (An example is the difference between the *spin-Seebeck effect* and the *spin-dependent Seebeck effect*[6].) The alternative approach of retaining full generality by replacing scalars with vectors, vectors with tensors, etc. often reduces the potency of the original analogy. In this work, we attempt to (partially) avoid this problem by restricting the scope of the discussion and making clear mathematical definitions.

avoid confusion with the subscripts reserved for specifying the flow and orientation directions. In general, $r^{(ij)}$ may depend on the applied magnetic field B, diffusion constant D, spin lifetime τ_s, as well as drift effects from the current biases $j^{(k)}$. Examples will be given in the subsequent sections.

The boundary conditions of our devices, which relate $Q^{(i)}$ to the number polarization $p^{(i)}$ at the interface, are discussed in Sec. 3.4 . These boundary conditions may be linearized to take the form

$$\text{(no summation)} \qquad Q^{(i)} = \eta^{(i)} J^{(i)} + \chi^{(i)} p^{(i)}, \tag{3.41}$$

where $\chi^{(i)}$ is the spin sinking parameter and is typically small.

Note that a more general formulation of the spin-RA product would include a dependence on the orientation $\hat{\eta}$ of the injected spin current for each individual component of the spin accumulation $\vec{p}$. For a homogeneous field, however, it is sufficient to allow p, Q, and r to be be complex scalars as described in Sec. 3.1.4 provided that the boundary conditions satisfy the functional forms $Q_\parallel = Q_\parallel\left(p_\parallel\right)$ and $Q = Q\left(p\right)$.

Combining Eqs. 3.40 and 3.41 allows us to write the matrix equation

$$p^{(i)} = -\sum_{(j)} r^{(ij)} \left[\eta^{(j)} J^{(j)} + \chi^{(j)} p^{(j)}\right]. \tag{3.42}$$

Solving for the polarizations yields

$$\sum_{(j)} \left(\mathcal{I}^{(ij)} + r^{(ij)} \chi^{(j)}\right) p^{(j)} = -\sum_{(j)} r^{(ij)} \eta^{(j)} J^{(j)}, \tag{3.43}$$

$$p^{(i)} = -\sum_{(j),(k)} \left(\mathcal{I}^{(ij)} + r^{(ij)} \chi^{(j)}\right)^{-1} r^{(jk)} \eta^{(k)} J^{(k)}, \tag{3.44}$$

where $\mathcal{I}^{(ij)} = \delta_{ij}$ denotes the identity. In matrix form, we have

$$\begin{pmatrix} p^{(1)} \\ p^{(2)} \\ \vdots \\ p^{(N)} \end{pmatrix} = \begin{pmatrix} 1 + r^{(11)}\chi^{(1)} & r^{(12)}\chi^{(2)} & \cdots & r^{(1N)}\chi^{(N)} \\ r^{(21)}\chi^{(1)} & 1 + r^{(22)}\chi^{(2)} & \cdots & r^{(2N)}\chi^{(N)} \\ \vdots & \vdots & \ddots & \vdots \\ r^{(N1)}\chi^{(1)} & r^{(N2)}\chi^{(2)} & \cdots & 1 + r^{(NN)}\chi^{(N)} \end{pmatrix}^{-1}$$
$$\times \begin{pmatrix} r^{(11)} & r^{(12)} & \cdots & r^{(1N)} \\ r^{(21)} & r^{(22)} & \cdots & r^{(2N)} \\ \vdots & \vdots & \ddots & \vdots \\ r^{(N1)} & r^{(N2)} & \cdots & r^{(NN)} \end{pmatrix} \begin{pmatrix} \eta^{(1)} J^{(1)} \\ \eta^{(2)} J^{(2)} \\ \vdots \\ \eta^{(N)} J^{(N)} \end{pmatrix}. \tag{3.45}$$

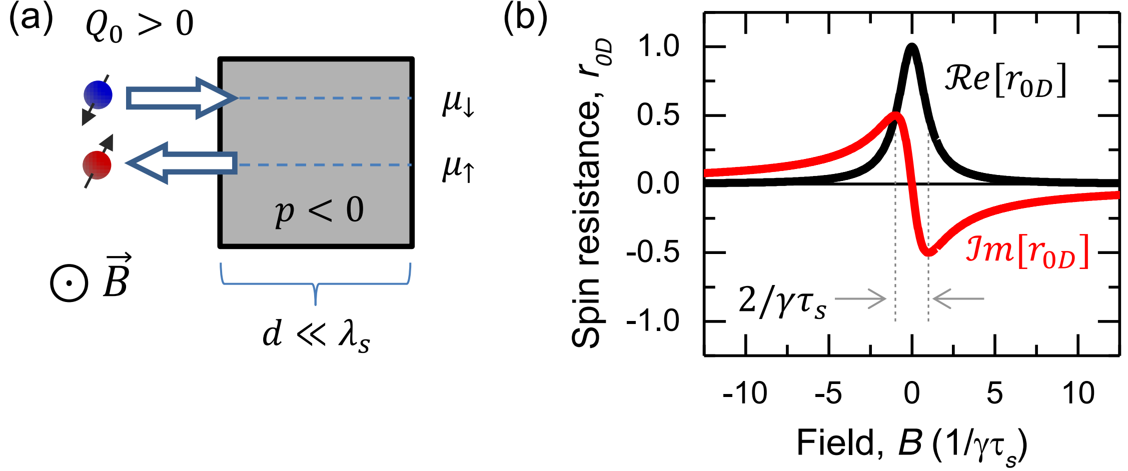

Figure 3.3: (a) Cartoon of balance between spin injection and relaxation. (b) Real and imaginary components of the spin resistance r_{0D} as a function of applied transverse field B.

For a single terminal device, the polarization at the interface is simply

$$p = -\frac{r\eta J}{1 + r\chi}. \tag{3.46}$$

Since r is a function of applied magnetic field, a non-zero value for the spin-sinking parameter χ will have an influence on the evolution of p with magnetic field.

3.2.2 0D model: Lorentzian

To begin with the simplest solution of Eq. 3.38, we simply ignore the drift and diffusion terms. This is only valid in situations where the spatial gradient of p is small. This occurs when either (1) the spin diffusion length λ_s greatly exceeds *all* confining dimensions of the device, or (2) for confining dimensions which are larger than λ_s, the spin injection rate is uniform over the entire region of interest. Under these conditions, first two terms of Eq. 3.38 will be small. We assume a constant spin injection rate Q_0 as depicted in Fig. 3.3(a), for which the continuity equation becomes

$$-(1 + i\gamma B\tau_s)\, p - Q_0\frac{\lambda_s}{h} = 0. \tag{3.47}$$

Solving for the real and imaginary components of p yields even and odd Lorentzian solu-

tions:

$$r_{0D} = -\frac{p}{Q_0} = \frac{\lambda_s/h}{1+i\gamma B\tau_s} \tag{3.48}$$

$$= \frac{\lambda_s}{h}\left(\frac{1}{1+(\gamma B\tau_s)^2} - i\frac{\gamma B\tau_s}{1+(\gamma B\tau_s)^2}\right). \tag{3.49}$$

This model is widely used for extracting spin lifetimes from Hanle measurements, often despite neither of the conditions above being fulfilled. The convenience stems from the ability to 'read off' the spin lifetime as the half-width at half height as shown in Fig. 3.3(b).

3.2.3 1D model: vertical diffusion

To go beyond the simple model presented in the previous section, we start by writing Eq. 3.38 for one dimension

$$\lambda_s^2 p'' + \lambda_s J p' - (1+i\gamma B\tau_s)\, p = 0 \tag{3.50}$$

where the primes indicate spatial derivatives. As shown in Fig. 3.4, we enforce the boundary condition that the spin current must be equal to Q_0 at the FM/n-GaAs interface located at $x = 0$. In the semiconductor ($x > 0$), we look for exponentially decaying solutions of the form

$$p = p_0 e^{-x/\lambda}, \tag{3.51}$$

where λ denotes an effective spin diffusion length which may differ from λ_s in the presence of a drift current ($J \neq 0$). Insertion into Eq. 3.50 yields the following condition on the effective spin diffusion length λ:

$$\frac{\lambda_s}{\lambda} = \frac{J}{2} + \sqrt{\left(\frac{J}{2}\right)^2 + 1 + i\gamma B\tau_s}. \tag{3.52}$$

The spin current is given by

$$Q = Jp + \lambda_s p' = \left(J - \frac{\lambda_s}{\lambda}\right) p \tag{3.53}$$

$$= \left(\frac{J}{2} - \sqrt{\left(\frac{J}{2}\right)^2 + 1 + i\gamma B\tau_s}\right) p. \tag{3.54}$$

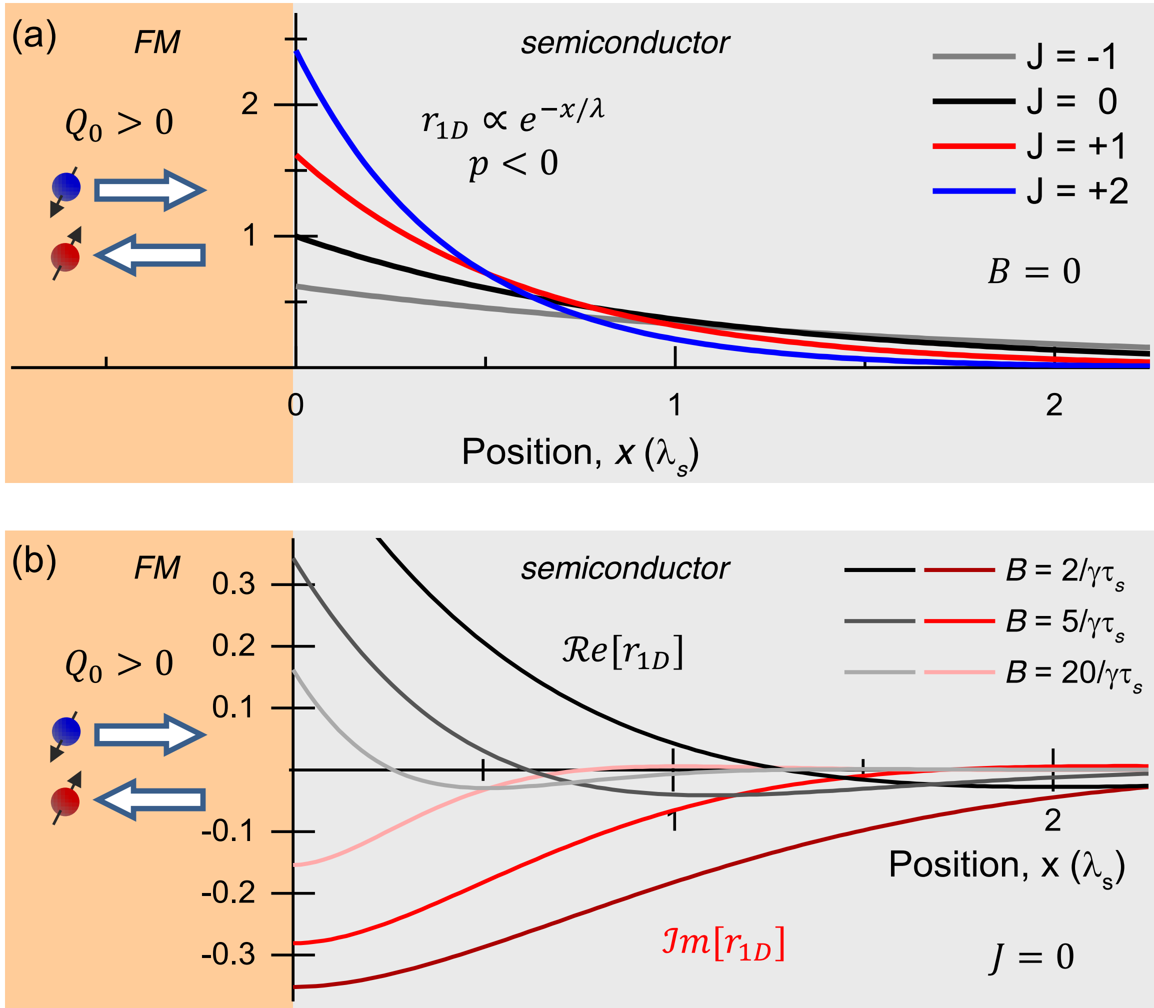

Figure 3.4: Spins allowed to diffuse into a one-dimensional channel.

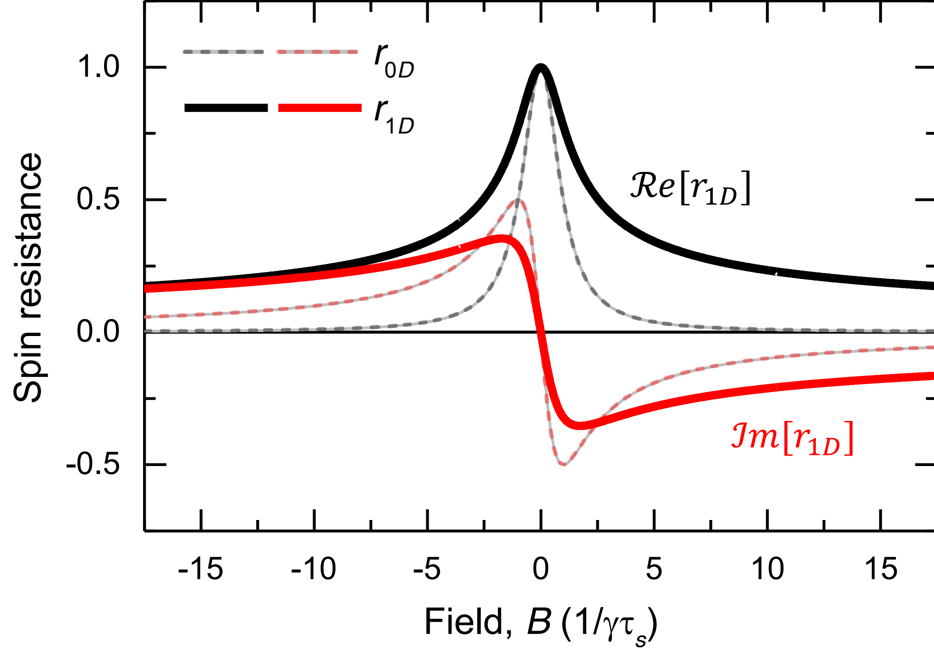

Figure 3.5: Comparison of Hanle line-shapes for the 0D and 1D models.

This allows us to write the spin resistance of the system as a function of position x and applied magnetic field B:

$$r_{1D} = -\frac{p}{Q_0} = \left(J - \frac{\lambda_s}{\lambda}\right)^{-1} e^{-x/\lambda} = \frac{\lambda_s/\lambda}{1 + i\gamma B\tau_s} e^{-x/\lambda} \tag{3.55}$$

The real part of r_{1D} is shown in Fig. 3.4(a) for several values of the charge current density J. Under forward bias ($J > 0$), which corresponds to electrons tunneling from n-GaAs into the Fe, the drift and diffusive terms oppose each other. This causes the spin diffusion length λ to contract. Due to the boundary condition requiring the spin current at the interface to remain constant, the polarization must increase. Under reverse bias ($J < 0$), the opposite situation is encountered. The drift and diffusive contributions to the spin current have the same sign, λ is elongated, and the polarization is distributed over a broader spatial region.

Upon application of a magnetic field, the polarization oscillates and rapidly decays as a function of x as shown in Fig. 3.4(b). The polarization at the interface is given by

$$r_{1D}\,(x = 0) = \frac{\lambda_s/\lambda}{1 + i\gamma B\tau_s} \tag{3.56}$$

It is insightful to compare this with the results obtained for the 0D case (Eq. 3.48). Here the confining dimension is given in the numerator as the spin diffusion length λ rather than

h. Further taking the diffusive limit ($J \to 0$) yields:

$$[r_{1D}(x=0)]_{J=0} = \frac{1}{\sqrt{1+i\gamma B\tau_s}}. \tag{3.57}$$

This means that in the absence of a magnetic field ($B = 0$), the dimensionless spin-RA product is unity, i.e. $p_0 = -Q_0$. For small magnetic fields ($\gamma B\tau_s \ll 1$), we have

$$[r_{1D}(x=0)]_{J=0,|\gamma B\tau_s|\ll 1} \approx \frac{1}{1+i\gamma B(\tau_s/2)} \tag{3.58}$$

In comparison to Eq. 3.48 above, this implies that ignoring the effects of diffusion underestimates the spin-lifetime by a factor of two. A comparison between the 0D and 1D models is shown in Fig. 3.5. For large fields, both the real and imaginary components of r_{1D} decay very slowly as

$$[r_{1D}(x=0)]_{J=0,\gamma B\tau_s\gg 1} \approx \frac{1+i}{\sqrt{\gamma B\tau_s}}. \tag{3.59}$$

Experimentally, this slowly decaying component is often discarded during the background subtraction process meant to eliminate magnetoresistive contributions to the observed signal. Since the maximum applied magnetic field B is typically a fixed quantity, the domain of the variable $\gamma B\tau_s$ decreases at higher temperatures as the relaxation rate $1/\tau_s$ increases. This will introduce systematic errors into the extraction of spin lifetimes and magnitudes unless the proper fitting procedure is employed.

We now consider the behavior of the magnitude of the polarization as a function of the current density. Assuming a fixed current polarization across the interface, i.e. $Q_0 = \eta J$, the polarization is given by

$$p_0 = -r_{1D}(x=0)\,Q_0 = -\eta J\lambda_s/\lambda \tag{3.60}$$

$$= -\eta J\left[\frac{J}{2}+\sqrt{\left(\frac{J}{2}\right)^2+1}\right] \tag{3.61}$$

This is shown in Fig. 3.6(a) for several values of $\eta = Q_0/J$. For large reverse bias ($J < 0$), the number polarization and current polarization saturates at the same value:

$$\lim_{J\to-\infty} p_0 = \eta. \tag{3.62}$$

However, a much more dramatic situation occurs for large forward bias ($J > 0$). As the spin diffusion length contracts, the polarization continues to increase in accordance with the boundary condition. At some point, the predicted polarization will exceed the physical limit

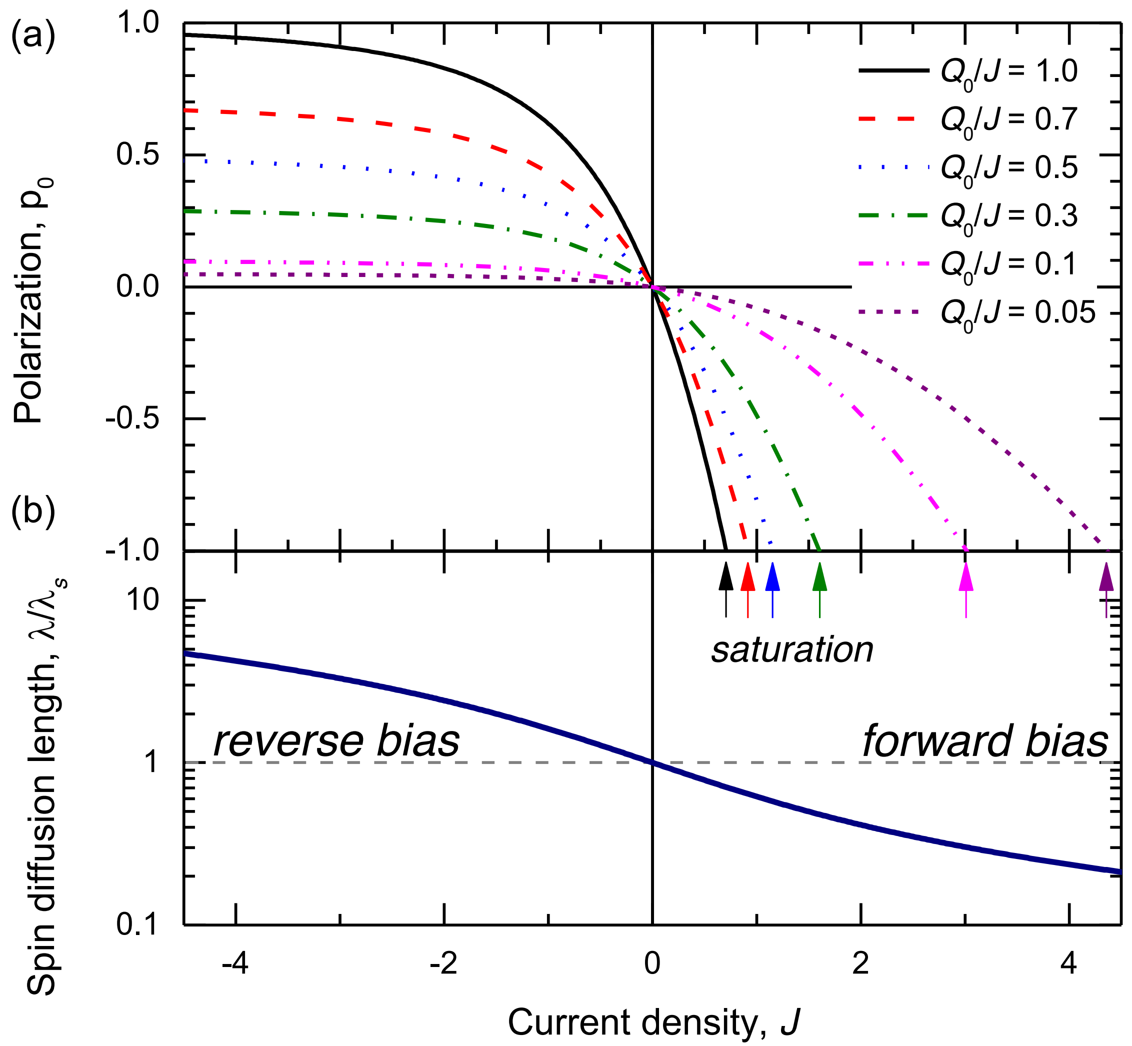

Figure 3.6: Bias dependence of (a) polarization at interface and (b) spin diffusion length.

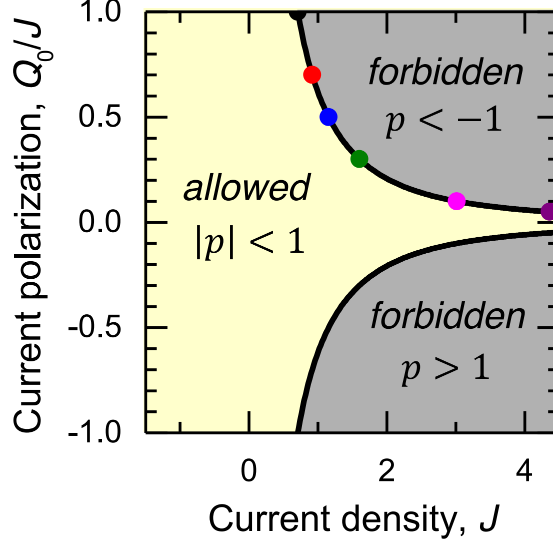

Figure 3.7: Phase diagram of current polarization vs. current density. Colored dots correspond to the arrows indicating saturation points in Fig. 3.6(a).

of unity where some other physical process must take over and cause p_0 to saturate. Note that if we were to include the large polarization parameters of Sec. 3.1.2, this saturation point would occur for even smaller values of J due to the decreased magnitude of the diffusive term relative to the drift term[46]. Setting $p_0 = \pm 1$ in Eq. 3.61 allows construction of the 'phase diagram' shown in Fig. 3.7. For forward biases exceeding $J = 1/\sqrt{2} \approx 0.7$, certain current polarizations are physically disallowed. Typical parameters for n-GaAs channels at 30 K with a doping twice the Mott criterion ($n \approx 2n_c$) are $\lambda_s \approx 5$ µm and $D \approx 2$ µm^2/ns, yielding a characteristic current density of $j_s = neD/\lambda_s \approx 250$ A/cm^2. This corresponds to experimentally accessible values of $J = j/j_s$ ranging from -1 to $+4$.

This indicates that spin signals observed under large forward current biases must have a small value of the injected current polarization, regardless of the initial polarization of the ferromagnet. In the language of Sec. 3.2.1, this may be parameterized as a non-zero value for the spin-sinking parameter χ at the interface. Further discussion of the appropriate boundary conditions is given in Sec. 3.4.

3.2.4 1D model: lateral diffusion

To model a more realistic device, we assume a piecewise continuous lateral geometry shown in Fig. 3.8 for which the continuity condition in each region reads

$$\lambda_s^2 p'' + \lambda_s (Jp)' - (1 + i\gamma B\tau_s)\, p - Q_0 \frac{\lambda_s}{h} = 0. \tag{3.63}$$

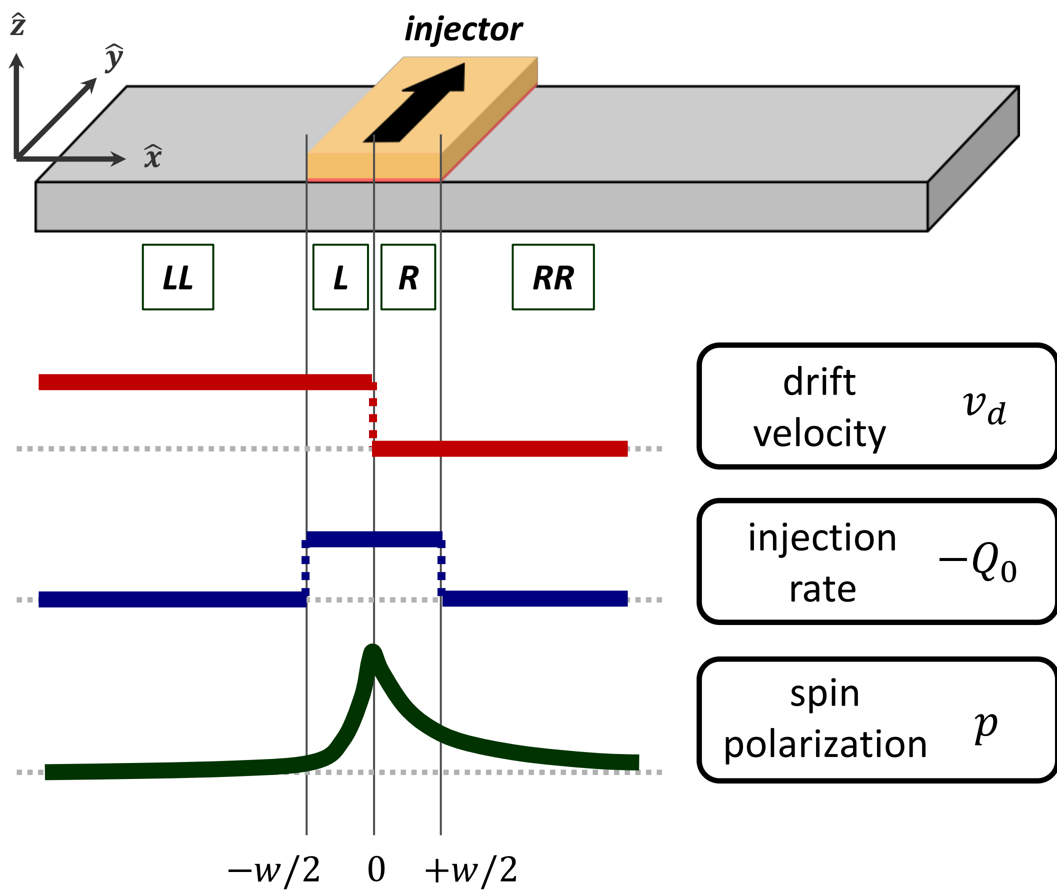

Figure 3.8: 1D lateral spin-valve model divided into four regions.

This has solutions in each region of the form

$$p = p^{+}e^{+x/\lambda_{+}} + p^{-}e^{-x/\lambda_{-}} - \frac{Q_0\left(x\right)\lambda_s/h}{1+i\gamma B\tau_s} \tag{3.64}$$

where

$$\frac{\lambda_s}{\lambda_{\pm}} = \frac{J}{2} \mp \sqrt{\left(\frac{J}{2}\right)^2 + 1 + i\gamma B\tau_s}. \tag{3.65}$$

Here λ_+ and λ_- denote the down-stream and up-stream spin diffusion lengths[44] for spins diffusing with or against the drift current respectively (for $J > 0$). When $J = 0$, we have $\lambda_{\pm} = \lambda_s$. Note the magnetic field dependence in the last term of Eq. 3.64, which is closely related to the 0D Lorentzian solution found in Sec. 3.2.2.

For the geometry shown in Fig. 3.8, with $Q_0\left(x\right) = Q_0\theta\left(\frac{w}{2} - |x|\right)$ and $J\left(x\right) = J\theta\left(-x\right)$, we write the following form for the spatial profile of the spin accumulation:

$$p\left(x\right) = \begin{cases} p_{LL}e^{+x/\lambda_+} & x < -w/2 \\ p_L^{+}e^{+x/\lambda_+} + p_L^{-}e^{-x/\lambda_-} - \frac{Q_0\lambda_s/h}{1+i\gamma B\tau_s} & -w/2 < x < 0 \\ p_R^{+}e^{+x/\lambda_s} + p_R^{-}e^{-x/\lambda_s} - \frac{Q_0\lambda_s/h}{1+i\gamma B\tau_s} & 0 < x < +w/2 \\ p_{RR}e^{-x/\lambda_s} & x > +w/2 \end{cases}. \tag{3.66}$$

w denoted the width of the injector region. Integrating Eq. 3.63 across the boundaries separating each region yields the conditions necessary to determine the constants p_{LL}, p_L^+, p_L^-, p_R^+, p_R^-, and p_{RR} in terms of the spin injection rate $Q_0\lambda_s/h$. In general, while the spin accumulation $p\left(x\right)$ is required to be continuous, its first derivative $p'\left(x\right)$ will have a discontinuity whenever the drift current J itself is discontinuous:

$$\lim_{x\to 0^-} p\left(x\right) = \lim_{x\to 0^+} p\left(x\right) \tag{3.67}$$

$$\lim_{x\to 0^+} p'\left(x\right) - \lim_{x\to 0^-} p'\left(x\right) = -\frac{p\left(0\right)}{\lambda_x}\left[\lim_{x\to 0^+} J\left(x\right) - \lim_{x\to 0^-} J\left(x\right)\right]. \tag{3.68}$$

The full solution for the spin resistance $r_{1DL} = -p\left(x\right)/Q_0$ is too verbose to include here. It is, however, although well within the computational capabilities of any modern computer algebra system. Retaining the full analytic solution is advantageous for the purposes of fitting experimental data and assigning uncertainties to the extracted parameters.

Figure 3.9 shows the spin resistance as a function of position for a typical case in which $w = \lambda_s$. As pointed out in Ref. [50], even though no charge current flows in the non-local region ($x > w/2$, $J = 0$), the magnitude of the spin polarization may be enhanced (reduced)

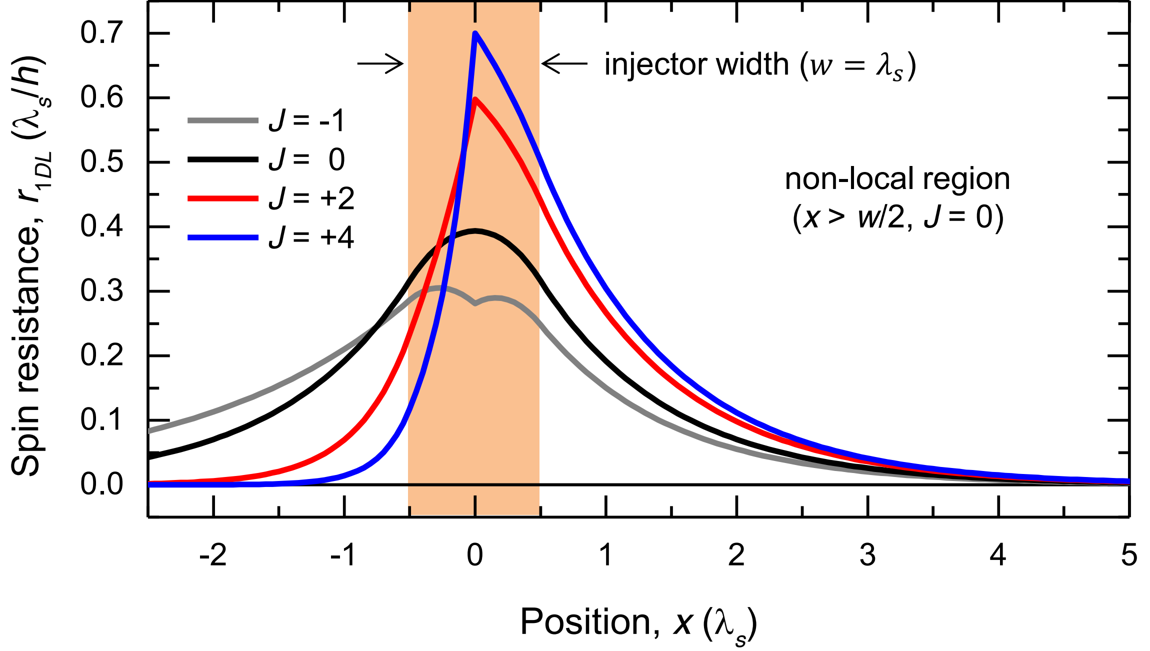

Figure 3.9: Spin resistance vs. position for the 1D lateral diffusion model for four different values of the drift current J.

in this region due to the forward (reverse) bias current flowing to the left of the injector.

3.3 Non-local Hanle fitting

The lateral diffusion model of the previous section may be used to extract spin lifetimes from the non-local Hanle experiment depicted in Fig. 3.10(a). The main difference with the experiment presented in Sec. 1.1 is that instead of applying the magnetic field in the plane of the device, the field is now swept parallel to the normal of the device. This causes the injected spins to precess and eventually dephase due to the diffusive nature of their motion. A non-local spin valve device with two central ferromagnetic contacts, each of dimensions 5 μm × 52.5 μm and a center-to-center distance of 10 μm. A constant current bias is applied to the injector contact with the counter-electrode[6] of the current source on the left-side of the device. The detector contact is placed outside of the charge current path to minimize magnetoresistive contributions to the spin-independent background signal. These contributions are removed from each Hanle curve by subtracting a low-order polynomial background ($N \leq 4$). Typical results as a function of bias and temperature are shown in

[6]Although the counter-electrodes are colored differently in Fig. 3.10(a) to indicate their passive role, they often consist of the same ferromagnetic stack as the central contacts.

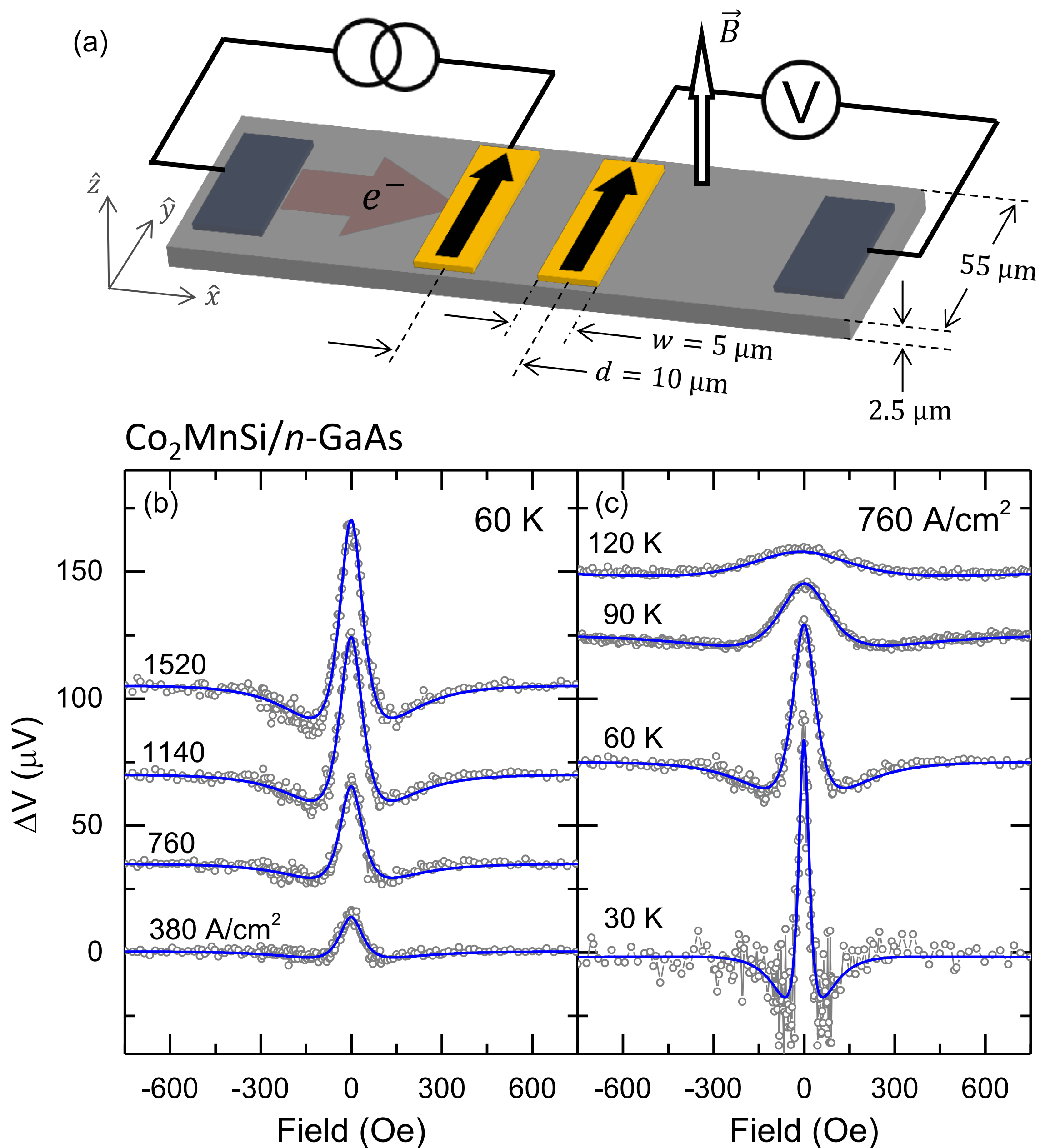

Figure 3.10: (a) Non-local spin valve with field applied out-of-plane. (b) Bias and dependence of non-local Hanle signal. (c) Temperature dependence of non-local Hanle signal. Gray open circles are the experimental data (after background subtraction) and the blue solid lines the result of fitting with the model presented in Sec. 3.2.4. (Sample UMN022-01B)

Figs. 3.10(b) and 3.10(c) respectively. As expected, the Hanle curve width increases at higher temperatures as the spin lifetime becomes shorter.

3.3.1 Temperature dependence of D

At each temperature, non-local Hanle data was acquired at multiple biases and fit simultaneously with a single set of parameters consisting of the spin lifetime τ_s, the diffusion constant D, as well as a quantity to absorb any experimental field offset B_0. The magnitude and vertical offset for each bias was allowed to vary independently. The real part of the 1D lateral diffusion model presented in Sec. 3.2.4 was integrated over the finite width of the detector contact to yield the proper fitting function:

$$\Delta V_{fit} \propto \mathcal{R}e\left[\int_{d-w/2}^{d+w/2} r_{1DL}\left(x\right) dx\right]. \tag{3.69}$$

The uncertainty in the extracted value of D was only small for curves which exhibit 'lobes', i.e. points along the Hanle curve which corresponding to a net rotation of the entire spin ensemble by π radians during transit from the injector to detector. Fig. 3.11(a) compares the results of allowing D to be a fitting parameter with the expected value from the Einstein relation:

$$D = \nu\frac{k_B T}{e}\frac{\mathcal{F}_{1/2}\left(\xi\right)}{\mathcal{F}_{-1/2}\left(\xi\right)}. \tag{3.70}$$

The excellent agreement with the Einstein relation confirms that (1) the charge and spin diffusion constants are equivalent at this doping and (2) the parabolic dispersion model described in Sec. 2.3.2 provides an accurate description of the compressibility of the system. The uncertainty in the extracted value of D increases dramatically at higher temperatures where the 'lobes' of the Hanle curves are not as prominent. However, having verified that the Einstein relation is appropriate for determining the spin diffusion constant in our samples, we now assume the validity of Eq. 3.70 for all temperatures. This allows the spin lifetime to be reliably extracted across the entire temperature range as shown in Fig. 3.11(a). The corresponding spin diffusion length $\lambda_s = \sqrt{D\tau_s}$ is shown in Fig. 3.11(b).

3.3.2 Temperature dependence of τ_s

The main source of spin relaxation in n-GaAs channels doped above the metal-insulator is the Dyakonov-Perel mechanism[51, 52]. In-between momentum scattering events, the electrons precess about the spin-orbit field given by the Dresselhaus term $\vec{\Omega}_D$ in Eq. 2.2. This may be modeled as a random walk process, whereby at each step the spins acquire

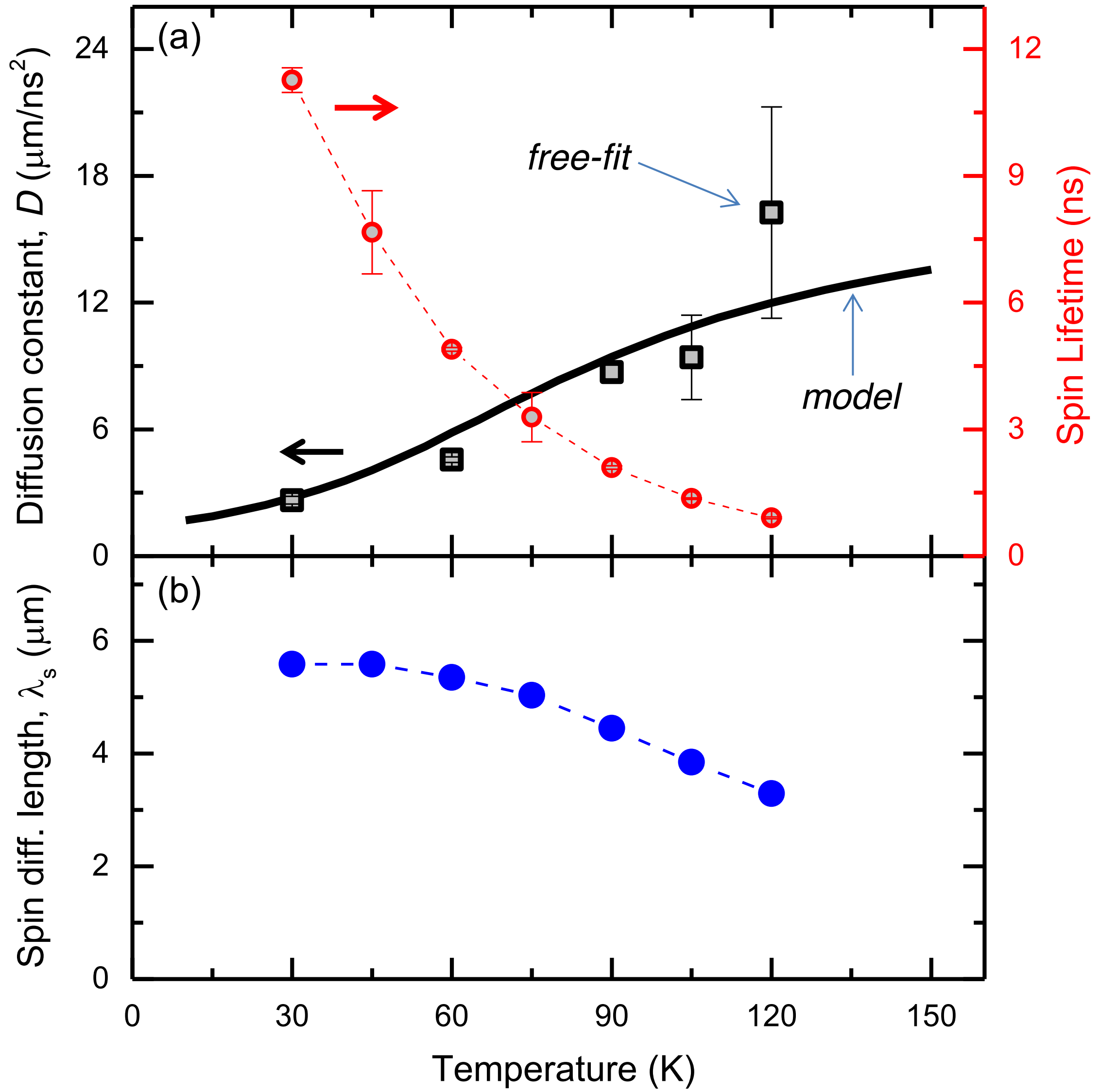

Figure 3.11: (a) Diffusion constant extracted from non-local Hanle fitting (black points) in comparison with values predicted from the Einstein relation (solid line). The extracted spin lifetimes are shown as red points and correspond to the right axis. (b) Spin diffusion length λ_s as a function of temperature.

Table 3.1: Momentum scattering factor γ_3 for each scattering mechanism

Scattering mechanism	γ_3	Energy exponent, $\tau_p \propto \varepsilon^s$
ionized impurity scattering	1/6	+3/2
polar optical phonon scattering	6/41	+1/2
acoustic phonon scattering, deformation potential	1	−1/2

a phase $\Omega_D \tau_p$. Here Ω_D is the magnitude of the Dresselhaus field and τ_p denotes the momentum relaxation time. We estimate the spin relaxation time τ_s as the time after which the spins have wandered 1 radian away from their initial orientation. Since the number of steps is τ_s/τ_p, this can be expressed as

$$1 \approx \sqrt{(\Omega_D \tau_p)^2 \left(\frac{\tau_s}{\tau_p}\right)}, \tag{3.71}$$

which yields a spin relaxation rate of

$$\frac{1}{\tau_s} = \Omega_D^2 \tau_p. \tag{3.72}$$

The most frequently cited characteristic of this relaxation mechanism is the inverse dependence on the momentum relaxation time τ_p, i.e. dirtier samples exhibit longer spin lifetimes. The results of this crude estimation correspond to the more rigorous approach given in Ref. [51], with the exception of an additional numerical prefactor, denoted γ_3, characterizing the ability of a given scattering process to 'randomize' the velocities after each collision. Table 3.1 lists[7] γ_3 for several common scattering mechanisms along with the appropriate exponent characterizing the energy dependence of τ_p. The magnitude of the Dresselhaus term for a given energy ε may be estimated as

$$\left\langle \Omega_D^2 \right\rangle = \frac{1}{3} \int_0^{2\pi} \int_0^{\pi} \frac{\sin\theta d\phi d\theta}{4\pi} \Omega_D\left(\vec{k}\right) \cdot \Omega_D\left(\vec{k}\right) \tag{3.73}$$

$$= \left(\frac{2\beta}{\hbar}\right)^2 \frac{4}{105} k^6 = \left(\frac{2\beta}{\hbar}\right)^2 \left(\frac{2m^\star}{\hbar^2}\right)^3 \frac{4}{105} \varepsilon^3. \tag{3.74}$$

The resulting spin relaxation rate for electrons at an energy ε is then

$$\frac{1}{\tau_s} = \left(\frac{2\beta}{\hbar}\right)^2 \left(\frac{2m^\star}{\hbar^2}\right)^3 \frac{4}{105} \gamma_3 \tau_p \varepsilon^3. \tag{3.75}$$

[7]Note that a typo in Ref. [51] incorrectly lists the value for ionized impurity scattering value as $\gamma_3 = 6$. The energy exponent of 1/2 given for the case of polar optical phonon scattering is likely only valid within the scope of this calculation. Since optical phonon scattering is neither elastic nor velocity randomizing, it cannot be accurately described by a momentum scattering time as discussed in Ref. [40].

Averaging over the Fermi surface yields

$$\left\langle \frac{1}{\tau_s} \right\rangle = \left(\frac{2\beta}{\hbar}\right)^2 \left(\frac{2m^\star}{\hbar^2}\right)^3 \frac{4}{105}\gamma_3 \frac{\int \tau_p \varepsilon^3 g(\varepsilon) f'(\varepsilon-\mu)\, d\varepsilon}{\int g(\varepsilon) f'(\varepsilon-\mu)\, d\varepsilon}. \tag{3.76}$$

As in Sec. 2.4, we assume a form for the momentum scattering time as $\tau_p(\varepsilon) = a\varepsilon^s$, where the exponent s is determined by the dominant scattering mechanism. Using Eq. 2.37 for a, we obtain the following expression for the spin relaxation rate

$$\begin{aligned} \frac{1}{\tau_s} &= \left(\frac{2\beta}{\hbar}\right)^2 \left(\frac{2m^\star}{\hbar^2}\right)^3 \frac{4\gamma_3}{105} \left(\frac{m^\star \nu_H}{e}\right) (k_B T)^3 \times \\ & \left[\frac{\Gamma\left[\frac{5}{2}+s\right] \mathcal{F}_{\frac{1}{2}+s}(\xi)}{\Gamma\left[\frac{5}{2}+2s\right] \mathcal{F}_{\frac{1}{2}+2s}(\xi)}\right] \left[\frac{\Gamma\left[\frac{9}{2}+s\right]}{\Gamma\left[\frac{3}{2}\right]} \frac{\mathcal{F}_{\frac{1}{2}+s}(\xi)}{\mathcal{F}_{-\frac{1}{2}}(\xi)}\right], \end{aligned} \tag{3.77}$$

where ν_H is the Hall mobility obtained from experiment.

Fig. 3.12 compares the experimental values of τ_s extracted from non-local Hanle data with the theoretical prediction given by Eq. 3.77. Considering that no free parameters were used to generate the theoretical curves, the agreement at high temperatures is quite good. Below 60 K, however, some other spin relaxation mechanism appears to dominate across. This saturation of the spin lifetime at lower temperatures may also be seen in the plots of Refs. [53, 54]. A new relaxation mechanism will be introduced in Chap. 5 based on inhomogeneities in the nuclear polarization.

3.4 Boundary conditions

In this section we investigate how to properly parameterize the FM/n-GaAs interface for use with the models described previously. While a growing body of work does exist on the phenomenon of electrical spin injection [55, 56, 57, 46, 58, 59], much less has been written about electrical detection with ferromagnetic contacts[60, 61, 62, 63].

3.4.1 Transparent interfaces

Let us first consider the case where the metal-semiconductor contacts form a fully-transparent Ohmic interface. In this case, the spin-splitting $\Delta\mu$ at the interface may be assumed to be the same in the semiconductor as well as the FM. This will drive a diffusive spin current on both sides as depicted in Fig. 3.13. However, because of the (much) lower spin-resistance of the ferromagnet, for the same applied 'spin voltage', the spin current in the ferromagnet will be much larger. The fraction of the initial spin current jP_{fm} which

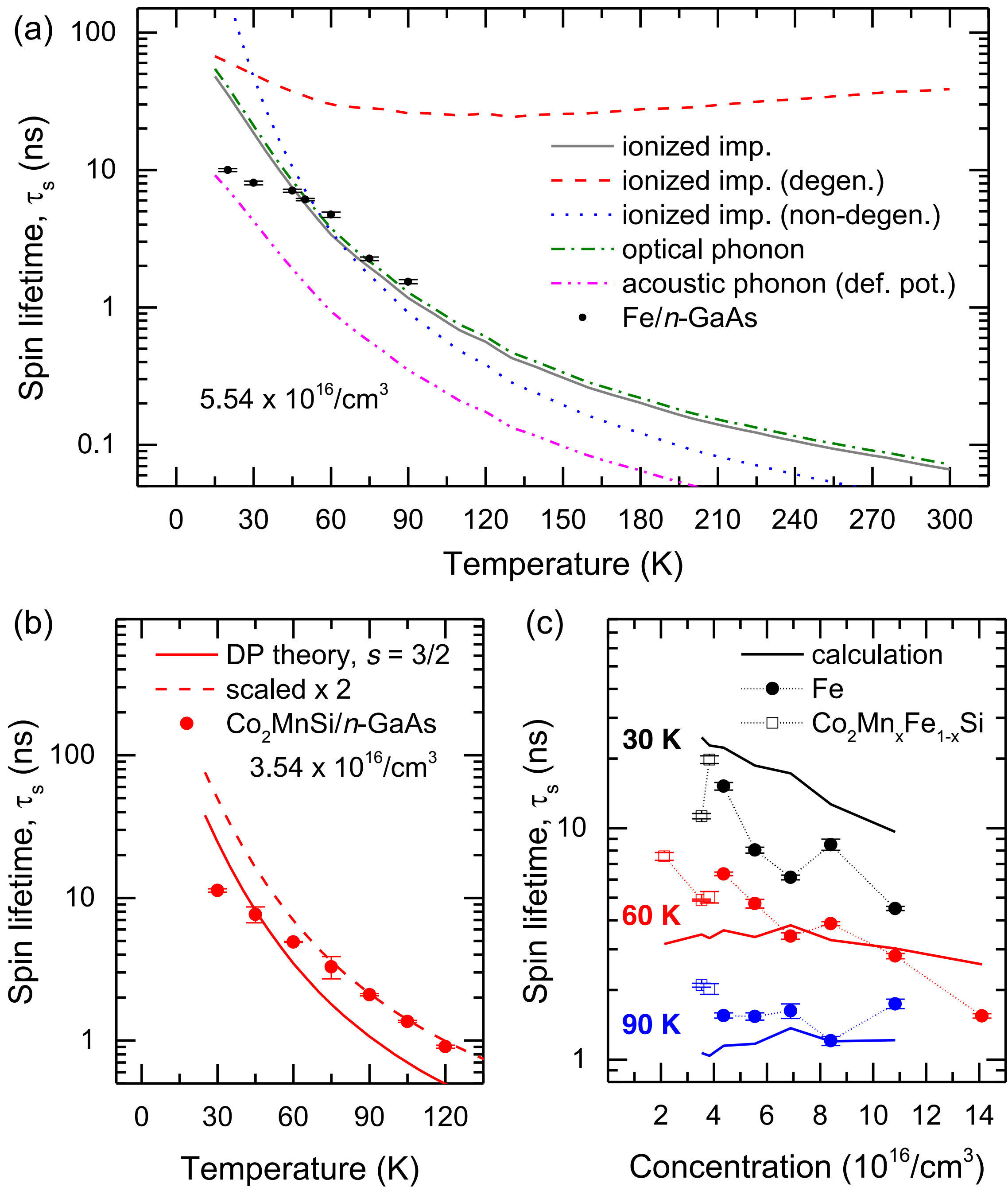

Figure 3.12: Temperature dependence of τ_s extracted from non-local Hanle measurements for (a) an Fe/n-GaAs sample (UMN019-04B) and (b) a Co_2MnSi/n-GaAs sample (UMN022-01B). (c) Doping dependence of τ_s for 30 K, 60 K, and 90 K.

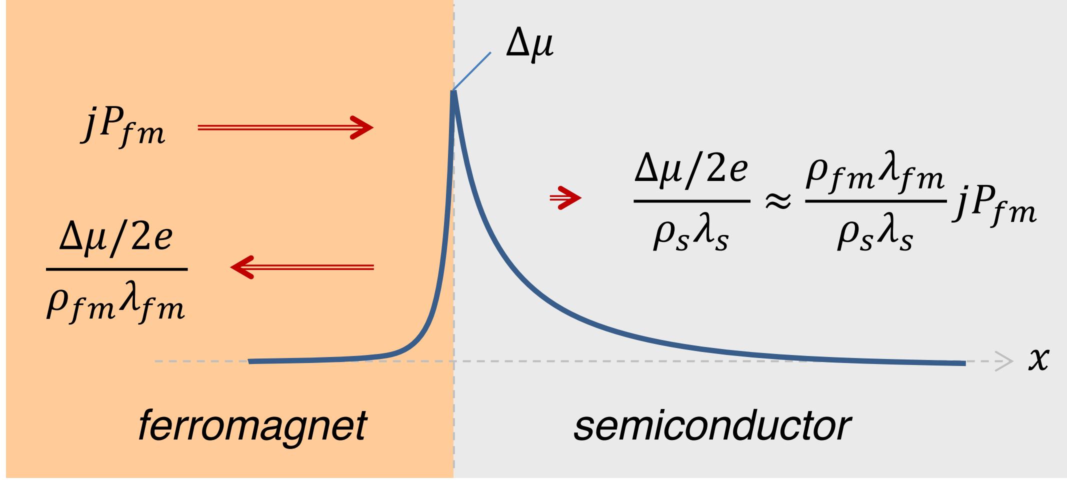

Figure 3.13: Spin currents at a transparent interface between a ferromagnet (FM) and non-magnetic semiconductor (S). Egregiously not to scale.

gets injected into the semiconductor may be estimated as

$$\frac{1/\rho_s\lambda_s}{1/\rho_s\lambda_s + 1/\rho_{fm}\lambda_{fm}} \approx \frac{\rho_{fm}\lambda_{fm}}{\rho_s\lambda_s} \approx 4 \times 10^{-7} \tag{3.78}$$

where we have used typical material parameters of $\rho_s = 26$ mΩ, $\lambda_s = 5$ μm for the semiconductor and $\rho = 12$ $\mu\Omega$ cm, $\lambda_{fm} = 4$ nm for the ferromagnet. The non-equilibrium spin currents in the ferromagnet are effectively being driven against an impenetrable barrier. This problem has come to be known as the 'conductivity mismatch' problem, although it should be noted that imbalance in either the charge resistivities *or* spin diffusion lengths contributes to the low efficiency. In the present example, both contributions are roughly equal.

3.4.2 FM/n-GaAs interface

To solve the problem of such a low injection fraction of the spin current into the semiconductor, Rashba[55] proposed the insertion of a tunnel barrier at the interface to limit the back diffusion of injected spins. This allows the spin-splitting $\Delta\mu$ on the semiconductor side to be independent of the splitting in the FM. While an oxide tunnel barrier can be used for such a purpose[64], a more elegant solution exists which utilizes the Schottky barrier formed naturally at the interface between a metal and semiconductor.

The behavior of the chemical potential at the interface between GaAs and vacuum or GaAs and a metal is dominated by the presence of surface states. These surface states pin

the chemical potential (Fermi level) in the middle of the gap of the semiconductor. This causes the formation of a depletion region near the interface, which in the case of a metallic contact serves as a barrier to electron transport. The width of this barrier, denoted w, may be estimated by assuming that all electrons within the barrier region have been moved elsewhere (i.e. occupy the surface states). This leads to a space charge in this region equal to equilibrium density n. By Poisson's equation, the curvature of the electrochemical potential is simply ne/ϵ. For a barrier height $\Delta\varepsilon$, this curvature implies a barrier width of

$$w = \sqrt{\frac{2\epsilon\Delta\varepsilon}{e^2 n}}. \tag{3.79}$$

For a typical channel doping of $n \approx 4\times10^{16}/\text{cm}^3$ and barrier height[8] $\Delta\varepsilon = \varepsilon_g/2 \approx 0.7$ eV, the depletion width is ≈ 160 nm. This decrease in the effective thickness should be accounted for in calculations which depend on the device geometry.

However, the Schottky barrier which forms at these doping levels is too thick to permit efficient spin injection or detection. In addition to the problems of Joule heating and Johnson noise associated with the increased resistivity, a large electric field would be required to improve over the transparent interface scenario described in Sec. 3.4.1. At such large fields, hot electron effects and inter-valley scattering processes would severely attenuate the spin lifetime in the semiconductor.

For this reason, we use a graded doping scheme to 'thin' out the barrier[66, 67] while still maintaining the long spin lifetime in the bulk of the device associated with lower doping levels. By increasing the donor concentration near the interface by a factor of $\sim 10^2$, this causes the barrier width to decrease by a factor of 10 as implied by Eq. 3.79. This scheme has an added advantage of producing localized two-dimensional states within the highly degenerate region as depicted in Fig. 3.14.

3.4.3 Tunneling currents – interface conductances

We start by writing down the tunneling current for each spin orientation as being proportional to the difference in electrochemcial potentials across the interface. In the absence of any spin accumulation in the semiconductor[9], this is given simply by

$$j_{\uparrow,0} = G_{\uparrow}(V_0)\ \left(\zeta_0 - \zeta_{fm,0}\right)/e \tag{3.80a}$$

$$j_{\downarrow,0} = G_{\downarrow}(V_0)\ \left(\zeta_0 - \zeta_{fm,0}\right)/e \tag{3.80b}$$

[8] Typical barrier heights at room temperature for metallic contacts (including Fe) on GaAs typically fall in the range 0.8 eV to 0.9 eV. See Ch. 3 of Ref. [65] for more information.

[9] As might be the case upon application of a sufficiently large transverse magnetic field such that $\gamma B\tau_s \gg 1$.

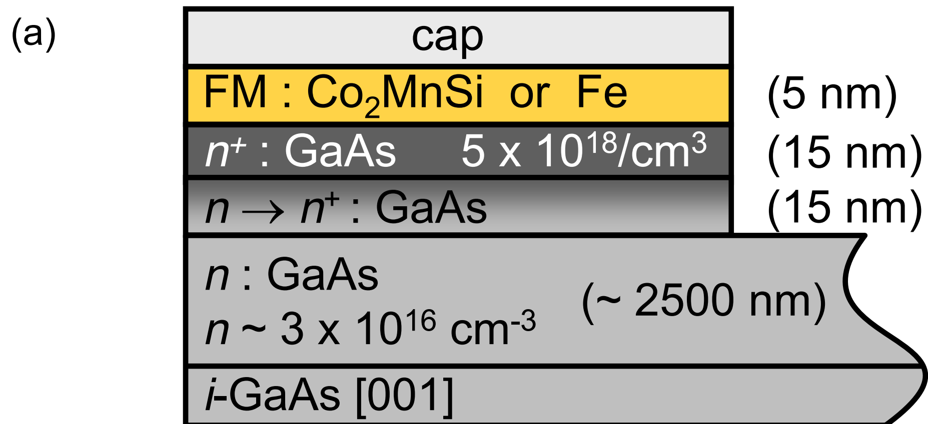

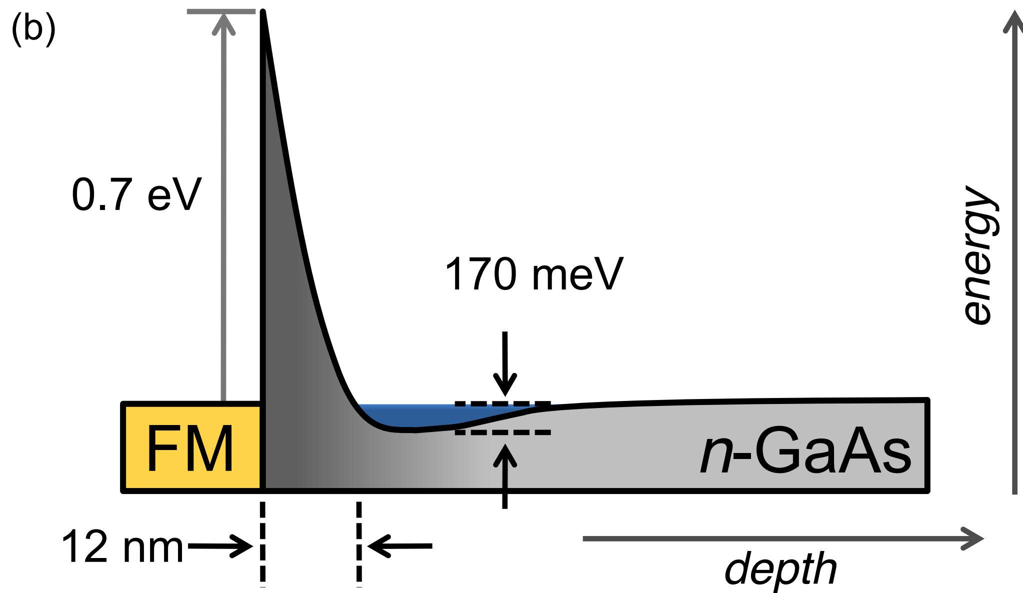

Figure 3.14: (a) Material structure of FM/n-GaAs heterostructure (b) Schottky tunnel barrier and localized quantum well states at interface.

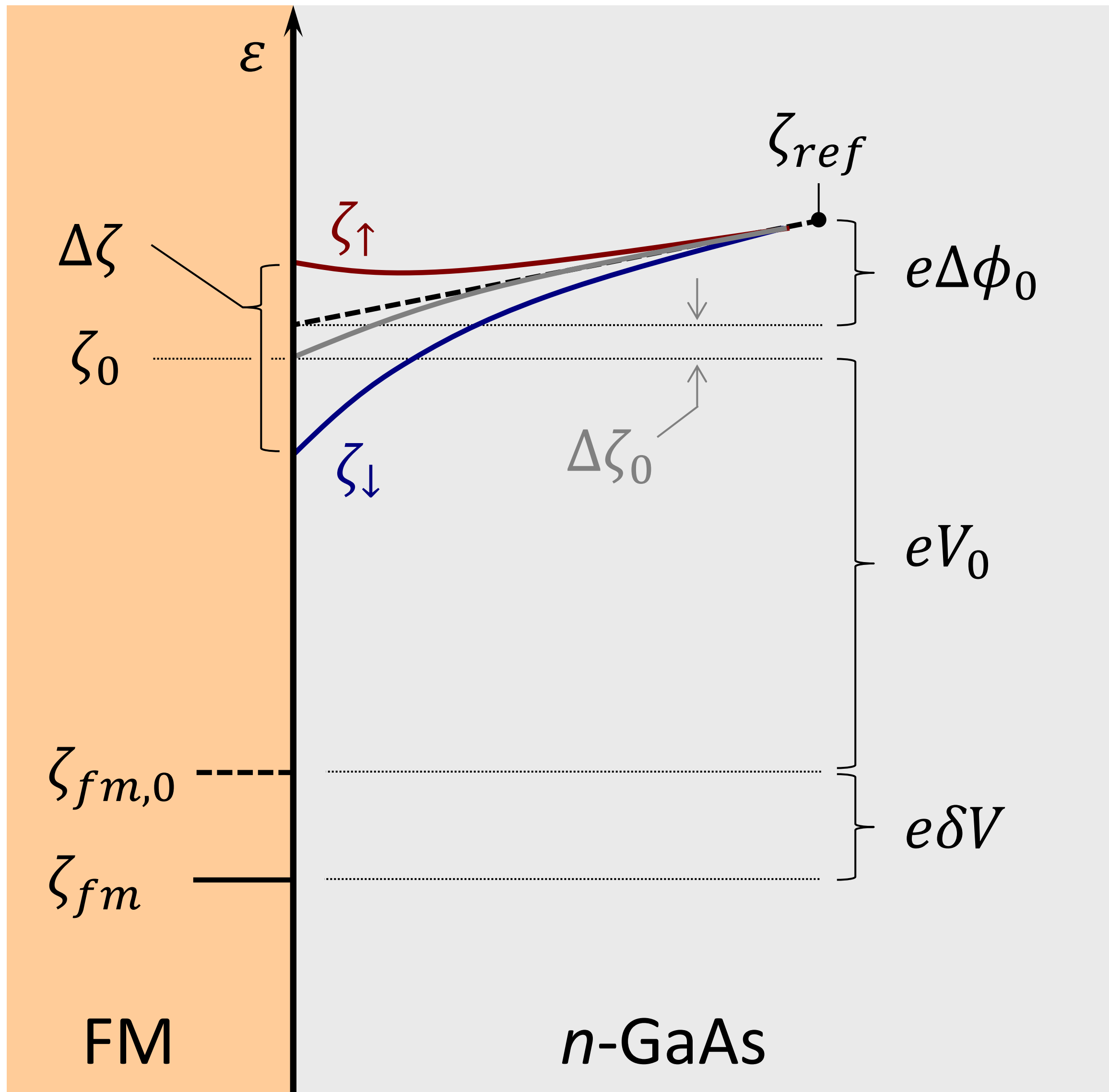

Figure 3.15: Potential levels near a forward biased FM/n-GaAs heterojunction. The thick dashed lines indicate the electrochemical potential in the absence of a spin accumulation.

Here $G_\uparrow$ and $G_\downarrow$ denote the tunneling conductances for spin-up and spin-down respectively evaluated at the interface voltage drop $V_0 = \zeta_0 - \zeta_{fm,0}$. As depicted in Fig. 3.15, ζ_0 is the electrochemical potential in the semiconductor and $\zeta_{fm,0}$ is the electrochemical potential level in the FM. Along with Refs. [44, 46, 60, 59], we assume that for all cases of interest, the spin-splitting in the metallic FM will be negligible compared to both the interfacial voltage drop as well as the spin splitting in the semiconductor. As was seen in Sec. 3.4.1, this is a consequence of the comparatively small spin-resistance in the FM. This may not necessarily be the case for non-metallic FMs, such as Mn-doped GaAs[63].

Due to the polarization of the FM, $G_\uparrow \neq G_\downarrow$, causing a net spin current to flow which establishes a steady-state spin accumulation ($\Delta\zeta \neq 0$) in the semiconductor[10]. Under this situation we have

$$j_\uparrow = G_\uparrow (V_0 + \delta V) \ (\zeta_\uparrow - \zeta_{fm}) / e \tag{3.81a}$$

$$j_\downarrow = G_\downarrow (V_0 + \delta V) \ (\zeta_\downarrow - \zeta_{fm}) / e. \tag{3.81b}$$

$\zeta_\uparrow$and $\zeta_\downarrow$ denote the electrochemical potentials for spin-up and spin-down in the semiconductor. Note that here we have specified the tunneling conductances $G_\uparrow$ and $G_\downarrow$ to be functions of the interface voltage *only*, and not the spin-splitting. While it is tempting to write the functional form as $G_\alpha = G_\alpha \left[(\zeta_\alpha - \zeta_{fm}) / e \right]$ this would be incorrect. Most of the voltage dependence of the tunneling conductances originates from the change in width of the depletion region near the interface. Since spin-splitting on the semiconductor side is expected to maintain charge neutrality, it should have a negligible effect on the width of the barrier. As such, the voltage dependence of the conductance extracted from the interface j-V curve cannot be used to parameterize a dependence of G_α on $\zeta_\alpha - \zeta_{fm}$. Instead, we factor out the dependence on bias as

$$G_\uparrow (V) = G (V) \left(\frac{1+\eta}{2} \right) \tag{3.82a}$$

$$G_\downarrow (V) = G (V) \left(\frac{1-\eta}{2} \right), \tag{3.82b}$$

where $\eta = (G_\uparrow - G_\downarrow) / (G_\uparrow + G_\downarrow)$ indicates the polarization or 'finesse' of the tunneling conductances[59]. We assume that while η depends strongly on the interface voltage V_0, it is slow varying for changes on the order of δV. This allows Eqs. 3.81a and 3.81b to be

[10] These expressions remain valid if the source of spin accumulation originates elsewhere, such as a source of optical injection or an additional remote FM injector contact (Fig. 1.2).

linearized as

$$j_{\uparrow} = \left[G\left(V_0\right) + \frac{\partial G}{\partial V}\delta V\right]\left(\frac{1+\eta}{2}\right)\left[\underbrace{\left(\zeta_0 + \frac{1}{2}\Delta\zeta\right)}_{\zeta_{\uparrow}} - \underbrace{\left(\zeta_{fm,0} - e\delta V\right)}_{\zeta_{fm}}\right]/e \quad (3.83a)$$

$$j_{\downarrow} = \left[G\left(V_0\right) + \frac{\partial G}{\partial V}\delta V\right]\left(\frac{1-\eta}{2}\right)\left[\underbrace{\left(\zeta_0 - \frac{1}{2}\Delta\zeta\right)}_{\zeta_{\downarrow}} - \underbrace{\left(\zeta_{fm,0} - e\delta V\right)}_{\zeta_{fm}}\right]/e. \quad (3.83b)$$

Taking the sum and difference yields the charge and spin currents tunneling across the interface:

$$j = \left[G\left(V_0\right) + \frac{\partial G}{\partial V}\delta V\right]\left[\left(\zeta_0 - \zeta_{fm,0} + e\delta V\right) + \frac{1}{2}\eta\Delta\zeta\right]/e \quad (3.84a)$$

$$q = \left[G\left(V_0\right) + \frac{\partial G}{\partial V}\delta V\right]\left[\eta\left(\zeta_0 - \zeta_{fm,0} + e\delta V\right) + \frac{1}{2}\Delta\zeta\right]/e. \quad (3.84b)$$

For experiments in which the current bias is held contstant, the sum of Eqs. 3.80a and 3.80b gives

$$j = j_{\uparrow,0} + j_{\downarrow,0} = G\left(V_0\right)\left(\zeta_0 - \zeta_{fm,0}\right)/e \quad (3.85)$$

allowing us to simplify Eqs. 3.84a and 3.84b. Keeping only terms linear[11] in δV and $\Delta\zeta$ and rearranging, we have

$$\delta V = -\frac{\eta\Delta\zeta/2e}{1 + \frac{j}{G^2(V_0)}\frac{\partial G}{\partial V}} = -\eta\left(\frac{j/V_0}{\partial j/\partial V_0}\right)\frac{\Delta\zeta}{2e} \quad (3.86a)$$

$$q = j\left[\eta + \left(1-\eta^2\right)\frac{\Delta\zeta/2e}{V_0}\right]. \quad (3.86b)$$

We highlight several important aspects of these two relations below.

Eq. 3.86b indicates that the spin injection process remains relatively uneffected by the spin accumulation in the semiconductor. The second term in the brackets is very small, even for maximal values of these junctions under forward bias ($\Delta\zeta \approx 1$ meV, $V_0 \approx 400$ mV). The polarization of the current flowing across the interface is, therefore, to very good approximation simply $q/j \approx \eta$.

This point was overlooked in the analysis of the spin detection process by Smith and

[11] Here we are assuming δV and $\Delta\zeta$ are small compared to V_0. Even in the small bias (non-local) regime where $eV_0 \ll \Delta\zeta$, this causes no significant loss of accuracy since in that limit we may assume a linear response such that $\left(\partial G/\partial V\right)\delta V \ll G\left(V_0\right)$.

Chantis [60], who proposed that the observed voltage shift should be proportional to the *spin current* at the detection contact rather than the *spin accumulation.* Starting with Eqs. 3.81a and 3.81b (with $\partial G/\partial V = 0$), they expressed δV in terms of the spin current q rather than the spin-splitting $\Delta\zeta$. In our nomenclature, this becomes

$$\delta V = -\frac{\eta}{1-\eta^2}\frac{\partial V}{\partial j}\left(q - \eta j\right) \tag{3.87}$$

As a measure of the spin detection efficiency, they evaluated the shift in the drift and diffusive components of $q = jp + neDp'$ induced by a remote spin injection source. However, this approach incorrectly assumes that the detector contact will sink the additional spin current δq provided by the remote source. The proper boundary condition is given by Eq. 3.86b, which implies that an additional source of spins diffusing towards a biased detector contact pile up at the interface such that, to good approximation, $\delta q \approx 0$.

From Eq. 3.86a, we see that in this model, the spin detection efficiency is given by

$$\frac{\delta V}{\Delta\zeta/e} = -\frac{\eta}{2}\left(\frac{j/V_0}{\partial j/\partial V_0}\right) \tag{3.88}$$

which *does not* scale with the interface conductance. The importance of whether $\delta V \propto q/G$ or $\delta V \propto \eta p$ lies in the implied scaling relationship with the junction resistance. If $\delta V \propto q$, then interfaces with a higher tunneling resistance will exhibit larger spin signals.

First, Eq. 3.86a expresses the shift in interface voltage expected to due the presence of a spin accumulation in the semiconductor. $\Delta\zeta$ is typically modulated via the application of a magnetic field, either due to the Hanle effect as described in the models of Sec. 3.2, or by reversal of the magnetization of a remote contact. Note that the voltage shift δV is independent of the resistance of the junction. It is, however, surpressed by the ratio of the differential conductance to the absolute conductance.

In Fig. 3.15, we have also included the possibility that the average electrochemical potential $\zeta_0 = \left(\zeta_\uparrow + \zeta_\downarrow\right)/2$ may also shift by an amount $\Delta\zeta_0$ in the presence of a spin accumulation. This effect is known as the spin-generated electromotive force (EMF) and is discussed further in Ch. 4.

We finally note that the spin sinking effect implied by the boundary conditions above is extremely small:

$$\chi = \left(1-\eta^2\right)\left(\frac{j}{j_s}\right)\left(\frac{D/\nu}{V_0}\right) = \left(1-\eta^2\right)G_0\rho\lambda_s \tag{3.89}$$

3.4.4 Tunneling currents – localized states

One of the main shortcomings of approach in the previous section is that we neglected the presence of the interfacial quantum well states which are responsible for most of the tunneling current under high forward bias[59]. This can be accounted for in the following manner. Following Ref. [59], we write

$$j_{\uparrow} = \frac{eN_{\uparrow}}{\tau_{esc,\uparrow}} \quad (3.90a)$$

$$j_{\downarrow} = \frac{eN_{\downarrow}}{\tau_{esc,\downarrow}} \quad (3.90b)$$

where now the bias dependence of the tunneling currents is encoded within the escape time for each spin channel. We now make the following change of variables as before

$$N_{\uparrow} = N\left(\frac{1+P}{2}\right), \qquad N_{\downarrow} = N\left(\frac{1-P}{2}\right) \quad (3.91)$$

$$\frac{1}{\tau_{esc,\uparrow}} = \frac{1}{\tau_{esc}}\left(\frac{1+\eta}{2}\right), \qquad \frac{1}{\tau_{esc,\downarrow}} = \frac{1}{\tau_{esc}}\left(\frac{1-\eta}{2}\right) \quad (3.92)$$

This allows us to write

$$j_{\uparrow,0} = \frac{eN}{2\tau_{esc}}\left(\frac{1+\eta}{2}\right) = \frac{j_0}{2}\left(\frac{1+\eta}{2}\right) \quad (3.93a)$$

$$j_{\downarrow,0} = \frac{eN}{2\tau_{esc}}\left(\frac{1-\eta}{2}\right) = \frac{j_0}{2}\left(\frac{1-\eta}{2}\right). \quad (3.93b)$$

Following the same approach as before, we write small variations in the currents as

$$j_{\uparrow} = \left(j_0 + \frac{\partial j}{\partial V_0}\delta V\right)\left(\frac{1+\eta}{2}\right)(1+P) \quad (3.94a)$$

$$j_{\downarrow} = \left(j_0 + \frac{\partial j}{\partial V_0}\delta V\right)\left(\frac{1-\eta}{2}\right)(1-P) \quad (3.94b)$$

Changing variables to j and q yields

$$j = \left(j + \frac{\partial j}{\partial V_0}\delta V\right)(1+\eta P) \quad (3.95a)$$

$$q = \left(j + \frac{\partial j}{\partial V_0}\delta V\right)(\eta + P) \quad (3.95b)$$

Solving for δV yields

$$\delta V = \frac{-\eta P j}{1+\eta P}\frac{\partial V_0}{\partial j} = -\frac{\eta P}{1+\eta P}\left(\frac{j/V_0}{\partial j/\partial V_0}\right)V_0. \tag{3.96}$$

For a 2D degenerate system we have assumed

$$\left(\frac{1}{n}\frac{\partial n}{\partial \mu}\right)_{QW} = \frac{1}{n}\left(\frac{\partial \varepsilon_{F,QW}}{\partial n}\right)^{-1} = \frac{1}{n}\left(\frac{\varepsilon_{F,QW}}{n}\right)^{-1} = \varepsilon_{F,QW}. \tag{3.97}$$

Taking $|\eta P| \ll 1$, Eq. 3.96 yields gives the detection efficiency as

$$\frac{\delta V}{\Delta\zeta/e} = -\frac{\eta}{2}\left(\frac{j/V_0}{\partial j/\partial V_0}\right)\frac{V_0}{\varepsilon_{F,QW}} \tag{3.98}$$

Note that this expression contains an extra factor of $V_0/\varepsilon_{F,QW}$ in comparison with the detection efficiency of the previous section given in Eq. 3.88. This implies that under large forward bias, the detection efficiency *is* proportional to the resistivity of the tunnel barrier.

The spin current is given by

$$q \quad = \quad j\left(\frac{\eta+P}{1+\eta P}\right) \tag{3.99}$$

such that the current polarization is simply

$$q/j \approx \eta + P. \tag{3.100}$$

Since P and η are of opposite sign under forward bias, this expression implies that the current polarization shuts off when the polarization becomes large. This represents an attractive way of dealing with the saturation regime required by Fig. 3.7.

It is possible now to relate the polarization in the quantum well P with the polarization p in the bulk by assuming a constant electrochemical potential splitting across the interface:

$$P = \frac{\Delta\zeta}{2e}\left(\frac{1}{n}\frac{\partial n}{\partial \mu}\right)_{QW} = \frac{\Delta\zeta/e}{2\varepsilon_{F,QW}} = \theta p \tag{3.101}$$

where $\theta = (D/\nu)/(\varepsilon_{F,QW}/e)$. However, this conversion ignores the possibility of spin relaxation within the quantum well itself, which may be substantial. The spin-current sunk into the quantum well can be estimated as $q_{QW} = N\theta p/e\tau_s$, where as the spin current tunneling across the interface is $q = \eta N/e\tau_{esc}$. From the structure shown in Fig. 3.14, we can make a rough estimate of the areal density as $N \approx \left(5\times10^{18}/\text{cm}^2\right)\times(15\text{ nm}) \approx$

$7.5 \times 10^{12}/\text{cm}^2$. For a typical bias of $j = 760$ A/cm^2, this implies an escape time of $\tau_{esc} = eN/j \approx 1.6$ ns. For the spin relaxation in the quantum well, we take $p/\eta \approx 1$, and $\theta \approx 1/30$ (at 60 K) to obtain the minimum allowable relaxation time in the well:

$$\left(\tau_{s,QW}\right)_{min} = \left(\theta p/\eta\right) \tau_{esc} \approx 50 \text{ ps}. \tag{3.102}$$

Unfortunately, typical relaxation rates in these quantum wells are estimated to be below this threshold[68, 69]. Thus, further measurements are required to more fully characterize the behavior of the injection and detection efficiencies to determine the appropriate model for the boundary conditions.

Chapter 4

Spin-generated electromotive force (EMF)

In this chapter we examine a new spin-to-charge conversion which develops in the regime of large spin polarization. We start our discussion by analogy to the Seebeck effect. As shown in Fig. 4.1(a), applying a heat source to one end of a semiconducting rod will cause a voltage to develop between the two ends which is proportional to the temperature difference ΔT. The magnitude of the voltage $\Delta V = -S\Delta T$ is given by the Seebeck coefficient S, which for n-GaAs is on the order of ≈ -300 μV/K [70]. In this chapter we present measurements of an analogous process in which spin injection is used to pull the system out of equilibrium rather than heat, as shown in Fig. 4.1(b). The increase in local free energy density (see Eq. 3.3) required to establish a steady-state non-equilibrium spin accumulation may be regarded as a source of electromotive force (EMF). Under open circuit conditions, this EMF will be observed as a potential difference proportional to the magnitude of the polarization squared, i.e. $\Delta V = kp^2$. (Under closed circuit conditions, this EMF will drive a current.) The coefficient k in our devices is on the order of ≈ 600 μV. Note that the inverse process corresponding an analog of the Peltier effect (i.e. charge-to-spin) was already discussed in Sec. 3.2.3 within the context of the elongation and contraction of the effective spin diffusion length in the presence of an electric field.

This effect has several advantages over the more traditional ferromagnetic (FM) detection methods described in Ch. 3. First, this source of EMF may be detected by both ferromagnetic and normal metal electrodes alike. This allows for more flexibility in device design and choice of contact materials to minimize noise. Second, because this effect scales quadratically with the polarization, the magnitude of this effect is comparable to and may even exceed the detection efficiency achievable with the non-local FM detection techniques.

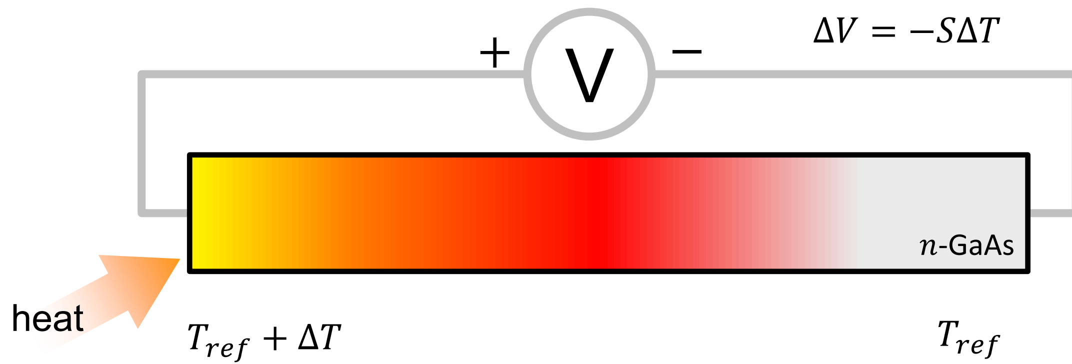

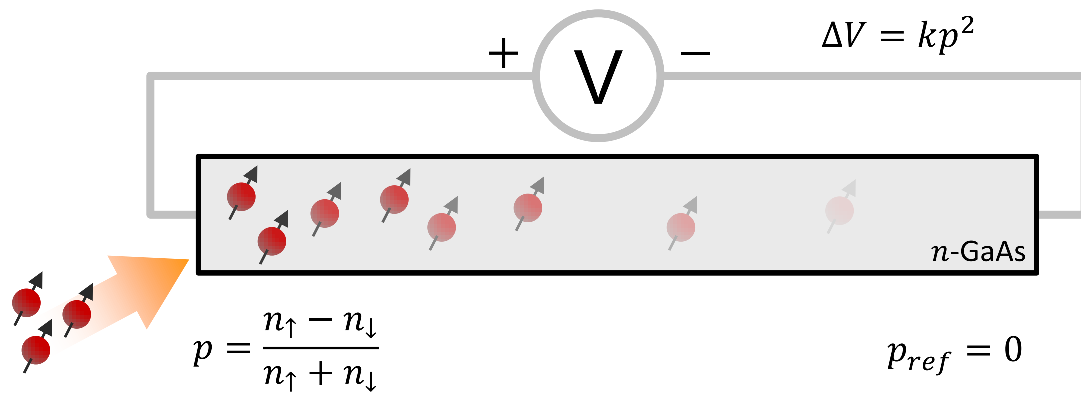

Figure 4.1: Introduction of the spin-generated EMF by analogy to the Seebeck effect.

Third, because the coefficient k depends soley on experimentally accessible parameters of the bulk semiconductor, this allows the polarization to be quantified in absolute terms with very few assumptions. One of the disadvantages of this approach is the lack of any information about the *sign* of the injected polarization.

The possibility of observing such an effect was first demonstrated by Vera-Marun *et al.* [71, 72] in graphene nanostructures as a small voltage shift in non-magnetic contacts adjacent to two ferromagnetic injectors. They interpreted these results in terms of an energy-dependence of the conductivity, causing an asymmetry in the transport of majority and minority carriers. In the sections that follow, we show that for degenerately doped n-GaAs, this effect is greatly enhanced in the regime of large spin polarization and may exceed the magnitude of the signals observed by traditional ferromagnetic detection techniques. We further provide the first comprehensive phenomenology of this effect in which both the energy-dependence of the conductivity *and* the density of states are taken into account.

In Sec. 4.1 we present a phenomenological model of the spin-generated EMF using the notation and methods developed in the previous chapters. In Sec. 4.2, the shorted-Hall measurement geometry is introduced. Sec. 4.3 and 4.4 provide further experimental proofs that this effect occurs as a direct result of the spin accumulation present in the channel of the device. Sec. 4.5 established the quadratic scaling relationship by comparing the magnitude of the spin-generated EMF measurements with the more traditional non-local spin-valve measurements. In Sec. 4.6 we show how the magnitude of the spin-generated EMF may be used to quantify the spin accumulation in absolute terms, independent of assumptions about the spin-dependent tunneling at the interfaces. Both number and current polarizations as a function of temperature are discussed in Sec. 4.7. Finally, in Sec. 4.8 we discuss situations which require further corrections to the phenomenology of Sec. 4.1.

4.1 Phenomenological model of the spin-generated EMF

We start with the drift-diffusion expressions (Eqs. 3.9a and 3.9b) presented in Sec. 3.1.2:

$$\vec{j}_\uparrow = eD_\uparrow \vec{\nabla} n_\uparrow - \sigma_\uparrow \vec{\nabla}\phi \tag{4.1}$$

$$\vec{j}_\downarrow = eD_\downarrow \vec{\nabla} n_\downarrow - \sigma_\downarrow \vec{\nabla}\phi. \tag{4.2}$$

Writing the number densities in terms of the fractional polarization as $n_\alpha = \frac{1}{2}n\,(1+\alpha p)$ and assuming variations in the background concentration to be small (i.e. $\vec{\nabla} n \approx 0$) yields

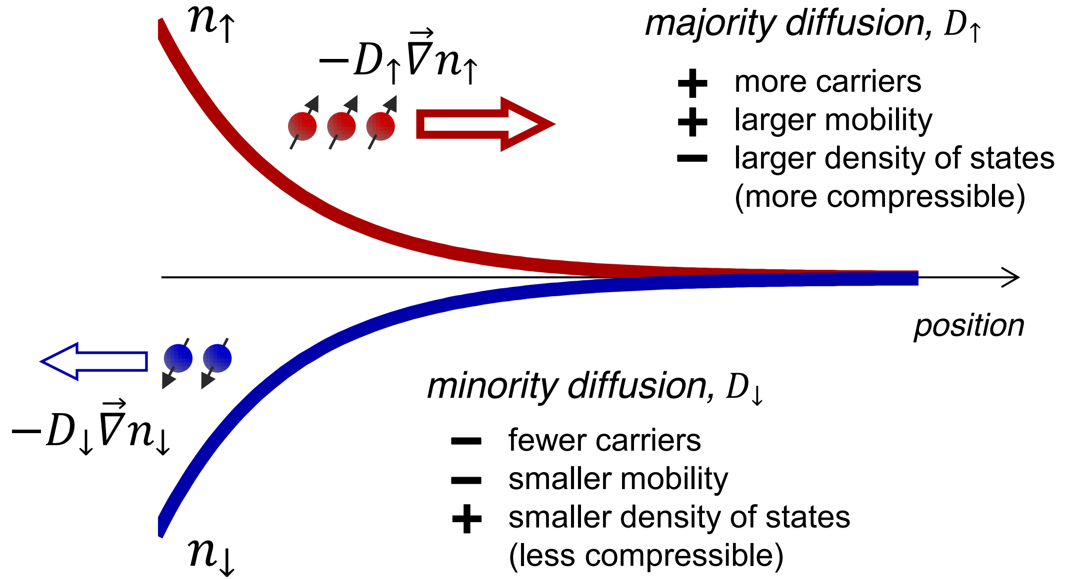

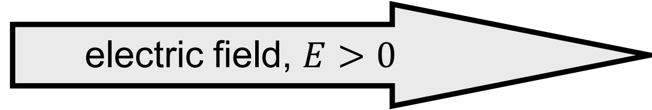

Figure 4.2: Physical origin of the spin-generated EMF as a difference in diffusion rates.

the following expression for the charge current density:

$$\vec{j} = e\left(\frac{D_\uparrow - D_\downarrow}{2}\right) n\vec{\nabla} p - \tilde{\sigma}\vec{\nabla}\phi. \tag{4.3}$$

The second term is simply Ohm's law with $\tilde{\sigma} = \sigma_\uparrow + \sigma_\downarrow$. The first term represents an additional contribution to the charge current from gradients in the spin accumulation whenever the diffusion rates of the majority and minority carriers are inequivalent. The Einstein relation tells us that the diffusion constant for each spin orientation is proportional to the carrier concentration n, mobility ν, and inverse compressibility $\kappa^{-1} = \partial\mu/\partial n$ of the system:

$$eD_\alpha = n_\alpha \nu_\alpha \kappa_\alpha^{-1}, \tag{4.4}$$

where $\alpha =\uparrow$ or $\downarrow$. All three of these quantities are in general energy-dependent, and are therefore sensitive to the polarization via shifts in the positions of $\mu_\uparrow$ and $\mu_\downarrow$. This is

shown schematically in Fig. 4.2 for a typical exponential decay of the polarization. Here the diffusive current of majority carriers exceeds that of the minority carriers traveling in the opposite direction due to the excess carriers and increased mobility (assuming $\tau_p \propto \varepsilon^s$ with $s > 0$). The magnitude of this effect receives an additional *negative* correction due to the energy dependence of the compressibility. Adding carriers becomes easier at higher energies, which has the effect of suppressing the diffusion rate as per Eq. 4.4.

In the presence of a non-equilibrium spin accumulation, therefore, the diffusivities of each band will in general be different ($D_\uparrow \neq D_\downarrow$). This generates an extra contribution to the charge current under closed circuit conditions, and causes an electrostatic potential to develop under open circuit conditions. This behavior is the very definition of a source of electromotive force, which in this case is being sustained by the continual input of angular momentum into the system. Since this process may be described as occurring while in contact with a fixed thermal reservoir, we prefer the simple term 'spin-generated EMF' as opposed to other possibilities based on analogies with thermoelectric phenomena[1].

Eq. 4.3 above may be further simplified by Taylor-expanding the diffusion constant relative to small changes in the number polarization:

$$D_{\uparrow(\downarrow)} \approx D_0 + (-) \frac{\partial D}{\partial n} np. \tag{4.5}$$

This allows us to re-write Eq. 4.3 as

$$\vec{j} \;=\; \frac{e}{2}\frac{dD}{dn} n^2 \vec{\nabla}\left(p^2\right) - \tilde{\sigma}\vec{\nabla}\phi \tag{4.6}$$

where we have used the chain rule $p\vec{\nabla}p = \frac{1}{2}\vec{\nabla}\left(p^2\right)$. Since we are interested in only the leading order term of the spin-generated EMF, we assume $\tilde{\sigma} \approx \sigma$ and that the prefactor of the first term is independent of position. This allows everything to be brought inside the gradient to obtain

$$\vec{j} = \sigma\vec{\nabla}\left(kp^2 - \phi\right) \tag{4.7}$$

with the prefactor given by

$$k = \frac{n}{2\nu}\frac{dD}{dn} = \frac{D}{2\nu}\frac{\partial D/\partial n}{D/n} = \frac{D}{2\nu}\Theta. \tag{4.8}$$

Θ is the parameter defined earlier in Sec. 3.1.2 to denote the energy dependence of the diffusion constant. Note that the first term of Eq. 4.7 means that a pure non-local spin

[1] One recent theoretical work[73] refers to this effect as a 'spin heat accumulation' in the context of spin-dependent tunneling across a FM/semiconductor interface.

current $\left(\vec{j}=0\right)$ cannot be achieved without establishing a non-zero electrostatic potential gradient equal proportional to the square of the polarization.

Further insight into the contributions to the magnitude of the spin-generated EMF may be obtained by substituting the Einstein relation $D = (n\nu/e)(\partial\mu/\partial n)$ into Eq. 4.8:

$$k = \frac{1}{2e}\left[\frac{\partial\mu}{\partial n}n + \frac{\partial^2\mu}{\partial n^2}n^2 + \frac{\partial\mu}{\partial n}n\frac{\partial\nu/\partial n}{\nu/n}\right] \quad (4.9)$$

$$= \frac{1}{2e}\left[\frac{\partial\mu}{\partial n}n(1+\Xi) + \frac{\partial^2\mu}{\partial n^2}n^2\right] \quad (4.10)$$

where $\Xi = (\partial\nu/\partial n)/(\nu/n)$ characterizes the energy dependence of the mobility as discussed in Sec. 3.1.2. In the sections that follow, we assume an energy-independent mobility ($\Xi = 0$) to simplify the interpretation and analysis of our experimental results. The magnitude of the systematic error that this introduces is discussed in Sec. 4.8. It is straightforward to show then that the prefactor k takes on a value of $\frac{2}{9}\varepsilon_F/e$ in the degenerate case and vanishes in the non-degenerate limit.

The first term of Eq. 4.10 appears as a consequence of the imbalance in the number of carriers in the two spin sub-bands and is formally equivalent to the contribution discussed in Ref. [71]. This contribution has the effect of 'pushing' electrons away from regions of large spin polarization. The second term in Eq. 4.10 is due to the non-constant density of states as depicted for a degenerate Pauli gas in Fig. 4.3(a). This contribution is analogous to the first-order term in the Sommerfeld expansion used to analyze the Seebeck effect[74, 75]. Note that in the presence of a spin accumulation, the chemical potentials for spin-up and spin-down must shift asymmetrically relative to the unpolarized state. This causes a decrease in the average chemical potential $\Delta\mu_{avg} = (\mu_\uparrow + \mu_\downarrow)/2 - \mu_0$ which tends to 'pull' electrons back towards the polarized regions. Thus, the two terms of Eq. 4.10 are, for our systems, of opposite sign with the first term representing the dominant contribution.

The dashed lines in Fig. 4.3(b) show the asymmetric nature of $j_\uparrow$ and $j_\downarrow$ for a typical polarization profile $p = p(0)e^{-x/\lambda_s}$ at 30 K ($p(0) = 0.6$, $\lambda_s = 5.6$ µm) in the absence of an electrostatic potential gradient $\left(\vec{\nabla}\phi = 0\right)$. Here x denotes the (non-local) position to the right of the injector contact. The solid lines indicate the steady-state condition after taking into account the spin-generated EMF. Typical values for Φ and $\Delta\mu_{avg}$ are shown in Fig. 4.3(c) for a concentration of $n = 3\times10^{16}$ cm^{-3} (Fermi energy, $\varepsilon_F = 5.3$ meV) at 30 K.

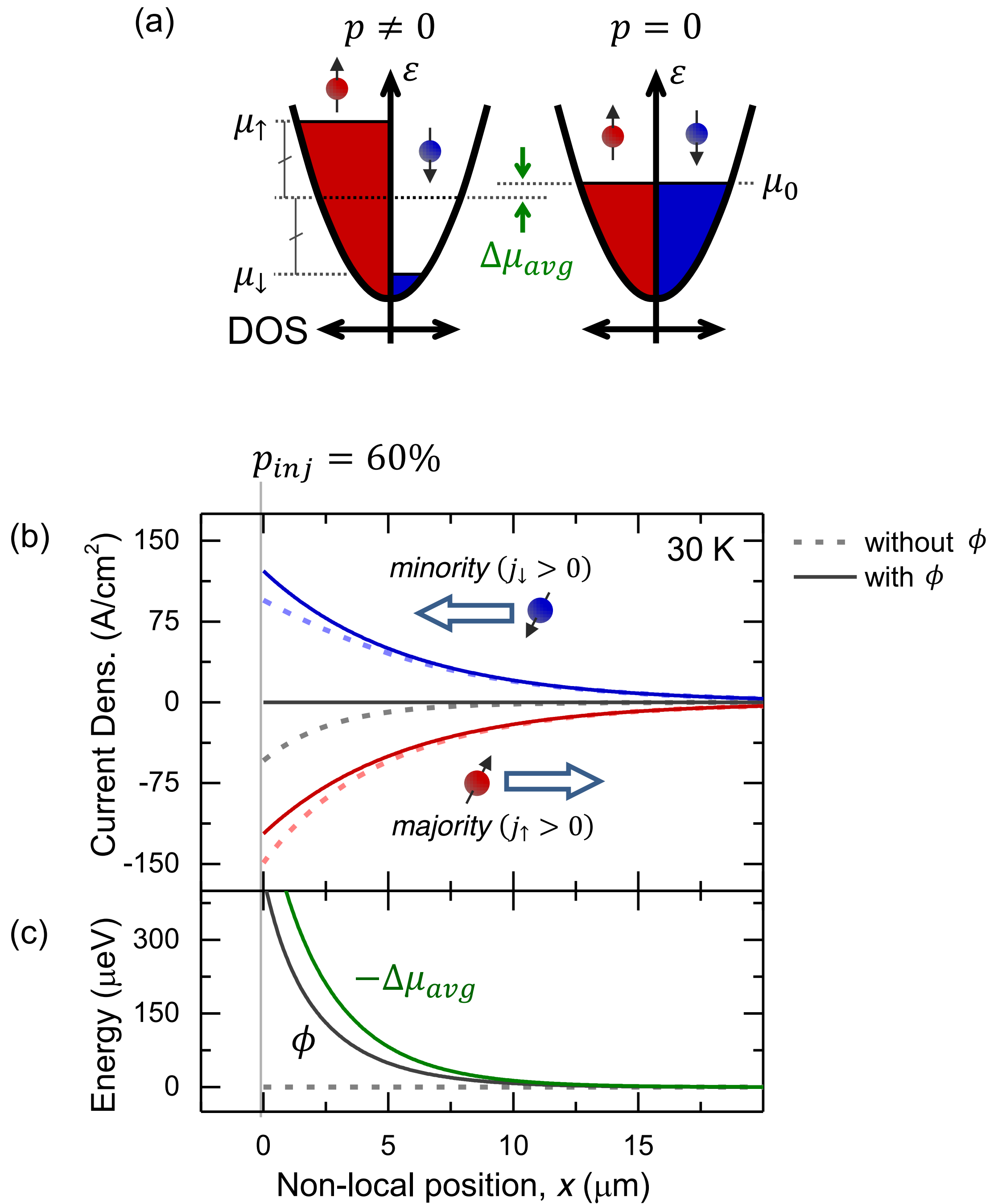

Figure 4.3: (a) Diagram of chemical potentials in the presence (left) and absence (right) of spin accumulation. (b) Current density as a function of non-local position for each spin band (↑ red, ↓ blue) and their total (black). Dotted (solid) curves exclude (include) the contribution from the steady-state potential ϕ. (c) Magnitude of ϕ and average chemical potential shift $\Delta\mu_{avg}$ vs. non-local position.

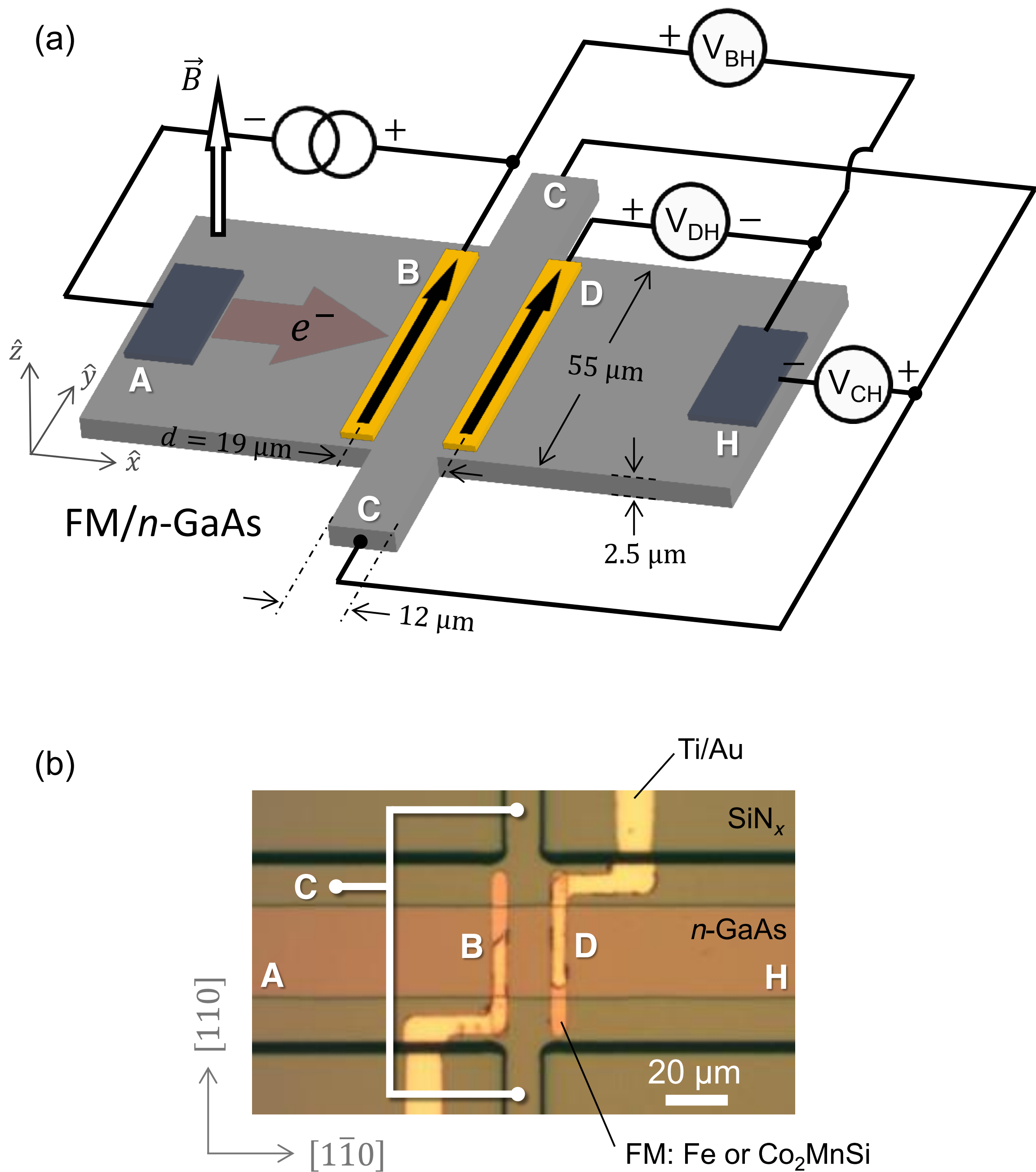

Figure 4.4: (a) Cartoon of shorted Hall device allowing three independent spin detection methods. (b) Micrograph of a Co_2MnSi/n-GaAs lateral spin valve device (sample UMN023-02D) with shorted central Hall arms for electrostatic detection of spin accumulation.

4.2 Shorted-Hall measurements

To observe this effect experimentally, several Co_2MnSi/n-GaAs and Fe/n-GaAs heterostructures were grown on semi-insulating GaAs (001) by molecular beam epitaxy and consisted of a 2.5 µm thick Si-doped channel ($n = 3 - 5 \times 10^{16}$ cm^{-3}), highly doped Schottky barrier ($15 - 18$ nm, $n^+ = 5 \times 10^{18}$ cm^{-3}), and 5 nm FM layer[10]. Standard lithographic and etching techniques were used to subtractively process lateral spin-valve devices with the configuration shown in Fig. 4.4(a). The n^+ layer was etched away from all regions except directly under the FM contacts. An additional PECVD-grown SiN_x layer was added to electrically isolate the Ti/Au leads from the channel. A micrograph of one of our finished devices is shown in Fig. 4.4(b).

Two ferromagnetic contacts, labeled B and D, were positioned on either side of a central Hall cross for the purposes of electrical spin injection and non-local ferromagnetic detection. Fig. 4.5(a) shows typical non-local spin valve and Hanle effect curves observed at contact D for both the parallel and antiparallel configurations with a forward current bias of 760 A/cm^2 applied to contact B. Low-order polynomials ($N \leq 4$) were subtracted from all curves displayed in Fig. 4.5 using points outside the regions of interest to eliminate ordinary magnetoresistive contributions. At 75 K, the $d = 19$ µm center-to-center separation between the contacts corresponds to approximately four spin diffusion lengths ($\lambda_s = 4.9$ µm) as determined from standard charge and spin transport measurements on companion devices[10]. The current and voltage counter-electrodes, labeled A and H respectively, are located 240 µm away (actual contacts not shown). These data establish the presence of a net spin current flowing into the channel and that contact D functions properly as a polarized detector of only one component of the non-equilibrium spin accumulation.

This spin accumulation was also detected as a common voltage shift in the central Hall arms, labeled C. These arms, each of length 170 µm, were shorted together into a single contact to eliminate any contributions from charge- or inverse spin-Hall effects. Fig. 4.5(b) shows a large spin-dependent signal at contact C obtained under identical conditions as the Hanle curves in Fig. 4.5(a) with the magnetic field swept normal to the plane of the device. In contrast to the signal observed at ferromagnetic detector D, the spin-dependent signal at contact C does not reverse sign upon reversal of the magnetization state of the injector (contact B). A Hanle effect of the same sign (not shown) was also observed when contact D was used as the injector for both magnetization states. These observations indicate that unlike the case of detection with a ferromagnet, which is sensitive to a single component of the polarization, the potential shift at contact C depends only on the total magnitude of the spin accumulation in the channel, but not its overall sign. This is supported by the observation that while the width of the line-shape in Fig. 4.5(b) matches the decay envelope

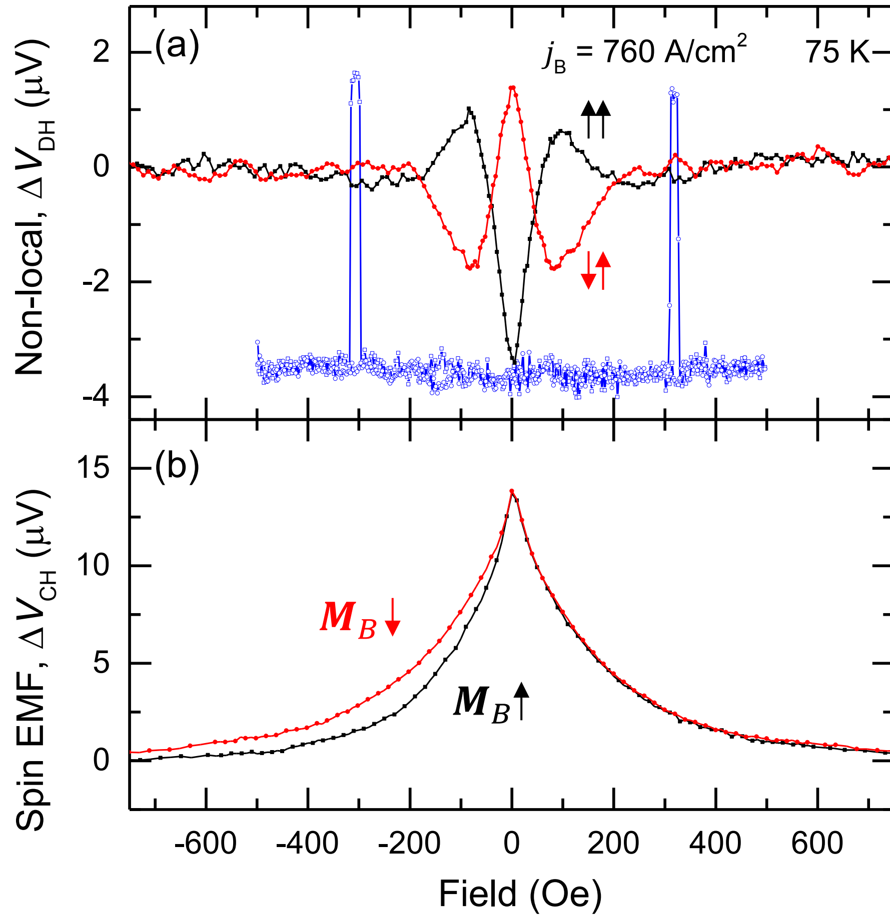

Figure 4.5: (a) Non-local spin valve (field in-plane) and Hanle effect (field out-of-plane) measured at contact D with forward current bias on contact B. (b) Hanle effect observed at contact C under identical conditions as panel (b) for both magnetization directions of contact B.

of the Hanle curve shown in Fig. 4.5(a), it lacks the precessional oscillations characteristic of a polarized measurement.

Fig. 4.6(b) shows typical raw data obtained at 60 K, 75 K, and 90 K on a Co_2MnSi/n-GaAs device with a forward current bias of $j_B = 760$ A/cm^2 applied to ferromagnetic injector contact B. Fig. 4.6(c) shows the same data after subtracting a third-order polynomial background. The background was fit using only those points for which the field magnitude was larger than 1250 Oe. The dotted gray lines in Fig. 4.6(c) show the magnitude of only the cubic term in the polynomial background. The physical origin of this cubic component has not yet been confirmed, although we speculate that it may be due to Lorentz deflection of the spin-EMF induced eddy currents described in Sec. 4.6 below.

4.3 Dual-injector experiment

To further demonstrate that the observed potential shift depends on the total magnitude of the spin accumulation in the channel (although not its overall sign), two separate 380 A/cm^2 forward current biases were applied simultaneously to contacts B and D with contact A serving as the counter-electrode for both current sources. With both ferromagnetic contacts functioning as spin injectors, the total magnitude of the spin accumulation in the channel was increased (decreased) by aligning the magnetization of the two contacts parallel (anti-parallel) to each other[72]. As shown in Fig. 4.7(b), this allows observation of a spin valve effect at non-magnetic probe C when a magnetic field is swept along the in-plane ferromagnetic easy axis [110]. The switching events occurring at ≈ 300 Oe are the same as those observed in Fig. 4.5(a).

Fig. 4.7(c) shows the corresponding Hanle curves obtained by sweeping the magnetic field normal to the plane of the device. The difference between the parallel and anti-parallel Hanle curves at 0 Oe equals that of the spin valve signal, demonstrating that the signal at contact C is sensitive to the superposition of the spin accumulation arising from both ferromagnetic injectors B and D. The Hanle line-shape broadens at higher temperatures as expected due to an increased spin relaxation rate, with both Hanle curves trending to zero at higher applied field.

4.4 Oblique Hanle measurements

The additional low-field features in Fig. 4.7(b) at low temperatures are caused by hyperfine interactions with dynamically polarized nuclei, which exert large effective Overhauser fields on the electron spin dynamics[30, 76]. This necessitates a more complex interpretation of

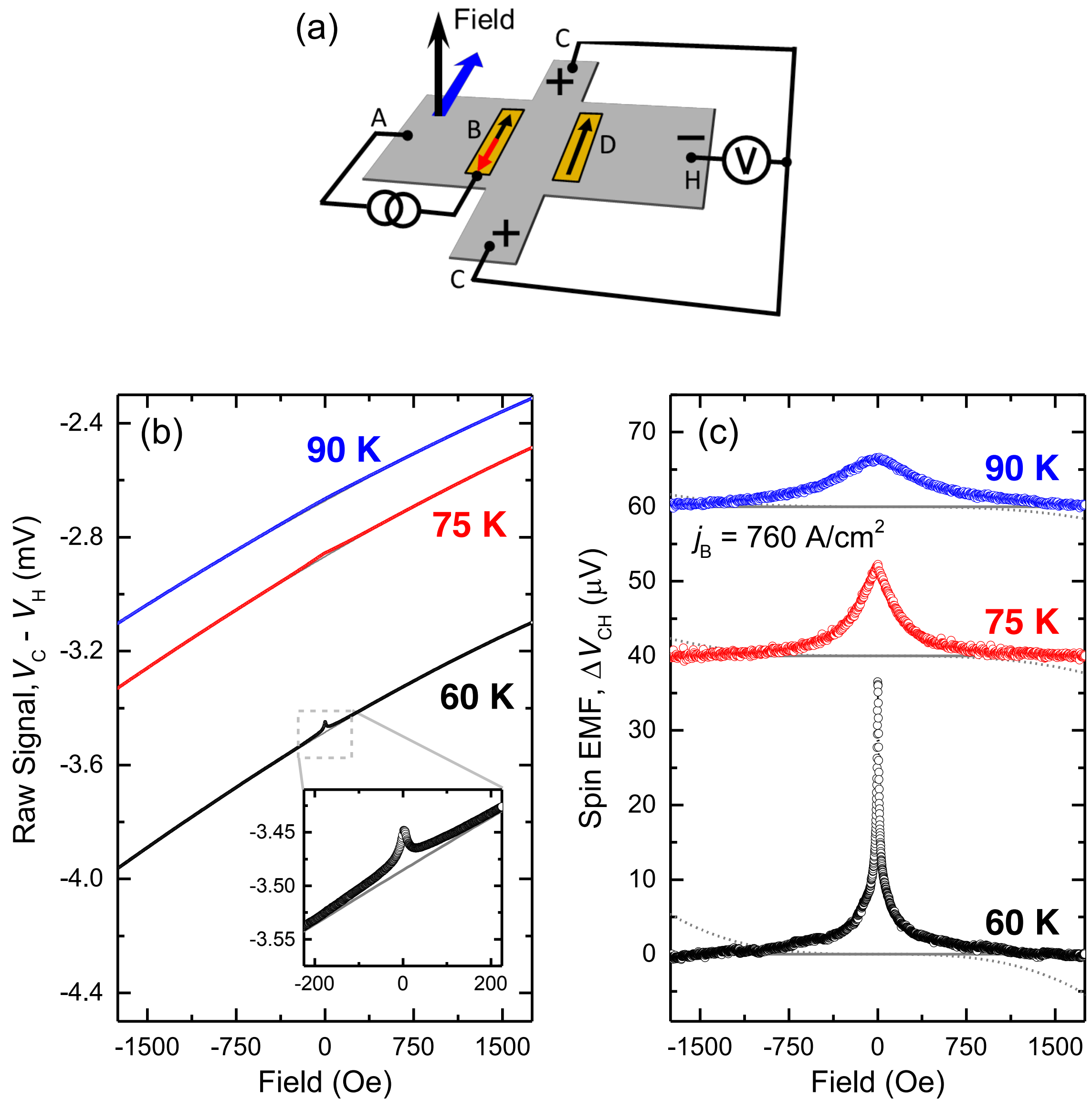

Figure 4.6: (a) Wiring diagram for the spin-EMF measurement. (b) Raw voltages measured between contacts C and H at 60 K, 75 K, and 90 K. Solid gray lines indicate 3rd-order polynomial background. No offset applied. (c) Same data as (b), but with third-order polynomial background subtracted and offset for clarity. Dotted gray lines indicate magnitude of cubic background term only.

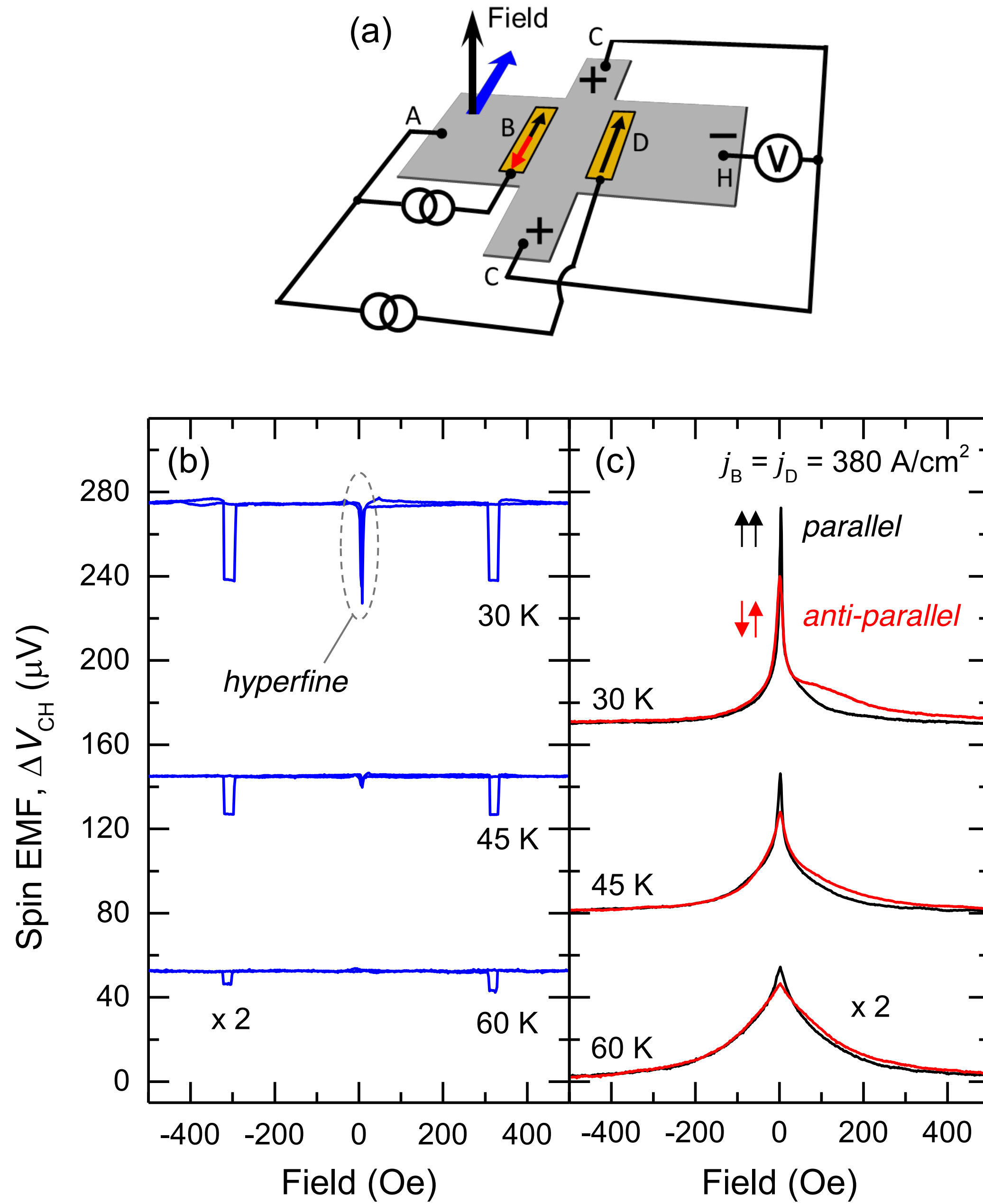

Figure 4.7: (a) Wiring diagram for the dual-injector experiment. (b) Spin valve and (c) Hanle effect data measured at contact C with identical current biases applied simultaneously to contacts B and D.

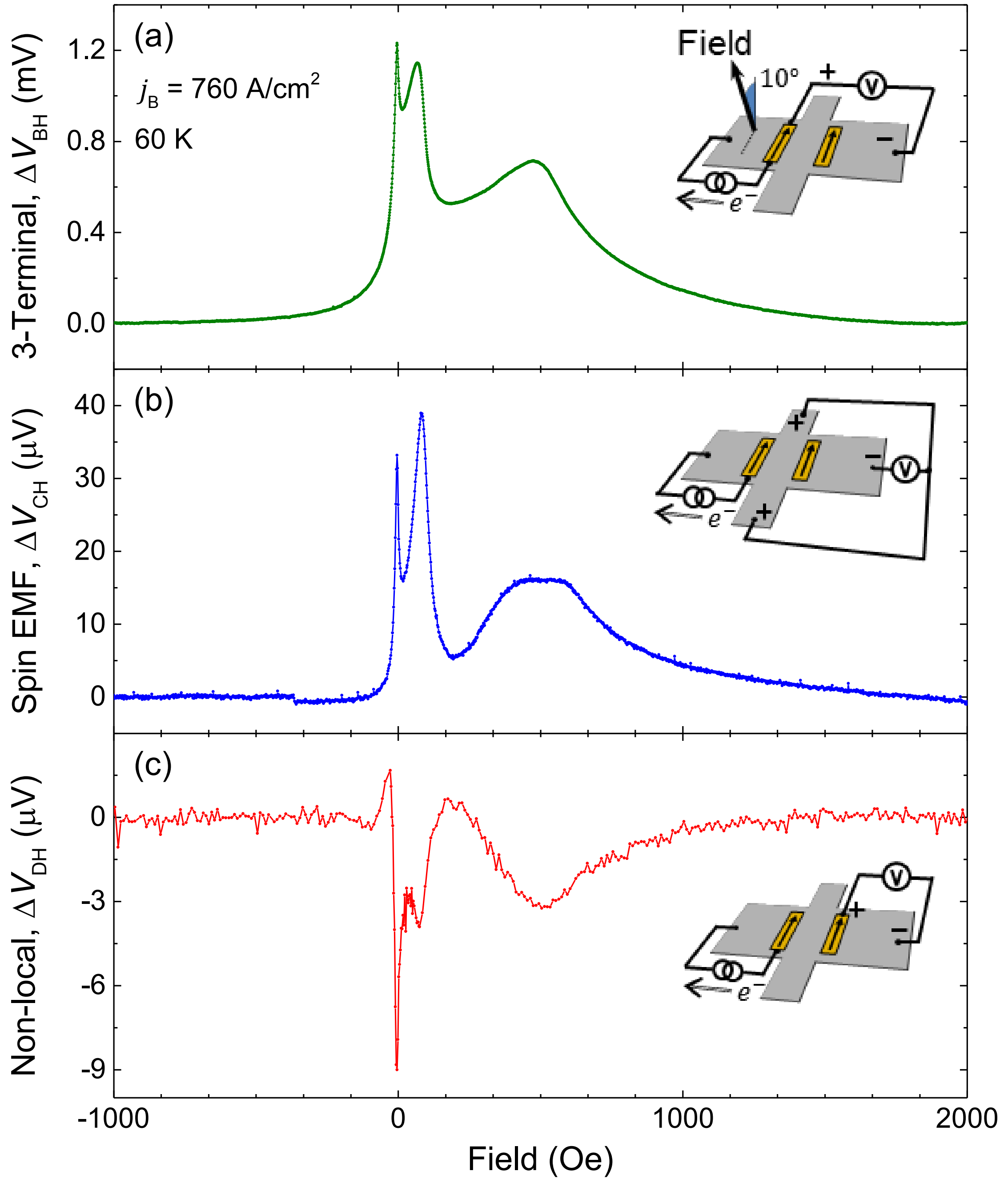

Figure 4.8: Oblique Hanle effects observed at (a) ferromagnetic injector B (three-terminal), (b) semiconducting arms C (spin-generated EMF), and (c) remote ferromagnetic detector D (non-local) under identical conditions with forward current bias on contact B.

Hanle line-shapes[77], yet also makes possible a robust test of whether a particular signal originates from spin-dependent processes. In the oblique Hanle geometry shown in Fig. 4.8, the magnetic field is applied at an intermediate angle between the device normal and the ferromagnetic easy axis. In this configuration, two additional satellite peaks appear at field values where the Overhauser field partially or wholly cancels the applied field. This cancellation reduces the Hanle dephasing effect and allows the electron spin ensemble to re-polarize. Fig. 4.8(a), (b) and (c) show the voltage measured on a second Co_2MnSi device at contacts B (three-terminal), C (spin-generated EMF), and D (non-local) respectively as the field is swept at a constant 10° orientation from the device normal. The appearance of satellite peaks at comparable positions in all three measurements provides conclusive evidence that the voltage shift observed at contact C is a direct measure of the spin accumulation in the channel. Since the sign of the Overhauser field in bulk GaAs is known[29], the position of the satellite peaks at positive field indicates majority spin accumulation in the channel. Note that the sign of the Hanle curve in Fig. 4.8(a) is opposite that of Fig.4.8(c) due to the inverted sign of the ferromagnetic detection efficiency at high forward bias[61].

4.5 Comparison with non-local data: quadratic scaling

In the non-local region where $j = 0$, Eq. 4.7 gives the electrostatic potential as $\Phi = kp^2$ which scales *quadratically* with the spin accumulation. This is in contrast to the non-local spin valve signal which scales *linearly*: $e\Delta V_{DH} = \eta\left(\mu_\uparrow - \mu_\downarrow\right) \approx 2\eta\frac{\partial\mu}{\partial n}p$, where η is the FM spin detection efficiency. Fig. 4.9 shows the Hanle and spin valve magnitudes observed at contacts C and D plotted against each other on a log-log plot while varying the current bias applied to injector contact B. The data at low bias confirm the predicted slope of two. The departure from quadratic behavior at high bias is caused by drift currents which redistribute more of the polarization toward the interfacial region which, as discussed below, sets the boundary condition for observing the spin-generated EMF at contact C. The onset of this drift effect occurs when the effective spin diffusion length[44] becomes smaller than the channel thickness t, i.e. drift velocity $v_d = j/ne \approx D/t$ as indicated by the vertical dashed lines in Fig. 4.9.

4.6 Modeling

To extract an absolute polarization from the magnitude of the electrostatic potential shift observed at contact C, we first determine the spin accumulation profile in the channel by discretizing the standard spin drift-diffusion relations in three dimensions. Expressing the

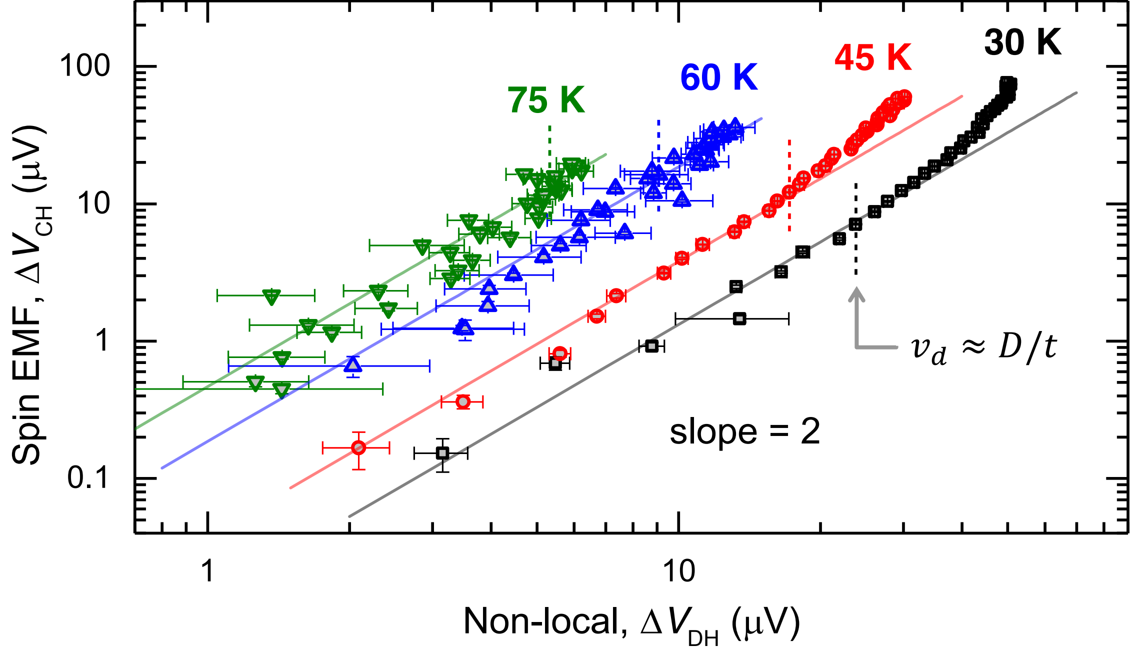

Figure 4.9: Log-log plot of the spin-generated EMF observed at contact C vs. (ferromagnetic) non-local spin-valve magnitude at contact D showing a quadratic dependence at low biases. Solid lines have a slope of 2.

results of Sec. 3.2 in experimental units yields:

$$\frac{\vec{j}}{ne} \cdot \vec{\nabla} p + D\nabla^2 p + p/\tau_s = 0. \tag{4.11}$$

A comparison between the planar projection of our simulation geometry and actual device micrograph is shown in Fig. 4.10(a). The simulation volume was 55 µm x 108 µm x 2.25 µm with a cell size of 1 µm x 1 µm x 0.25 µm. Eq. 4.11 is solved using a forward Euler approach assuming a constant current polarization $\alpha = (j_\uparrow - j_\downarrow)/j$ at the injector contact B. The spin lifetime $\tau_s = \lambda_s^2/D$ at each temperature was determined by fitting non-local Hanle curves obtained from companion spin valve devices on the same chip. The diffusion constant was obtained from the Einstein relation $eD = n\nu\,(\partial\mu/\partial n)$ as before. Fig. 4.10(b) shows typical results of the calculation for kp^2 at 60 K where the spin diffusion length was determined to be $\lambda_s = \sqrt{D\tau_s} = 5.6$ µm. Since Eq. 4.11 is linear, its solution may be directly scaled so that the corresponding electrostatic shift at contact C, as determined below, matches the experimentally observed value denoted by ΔV_{CH}. The overall magnitude of the spin accumulation profile may then be characterized by the injector polarization p_{inj}, defined as the average of the fractional number polarization p over the spacial extent of injector

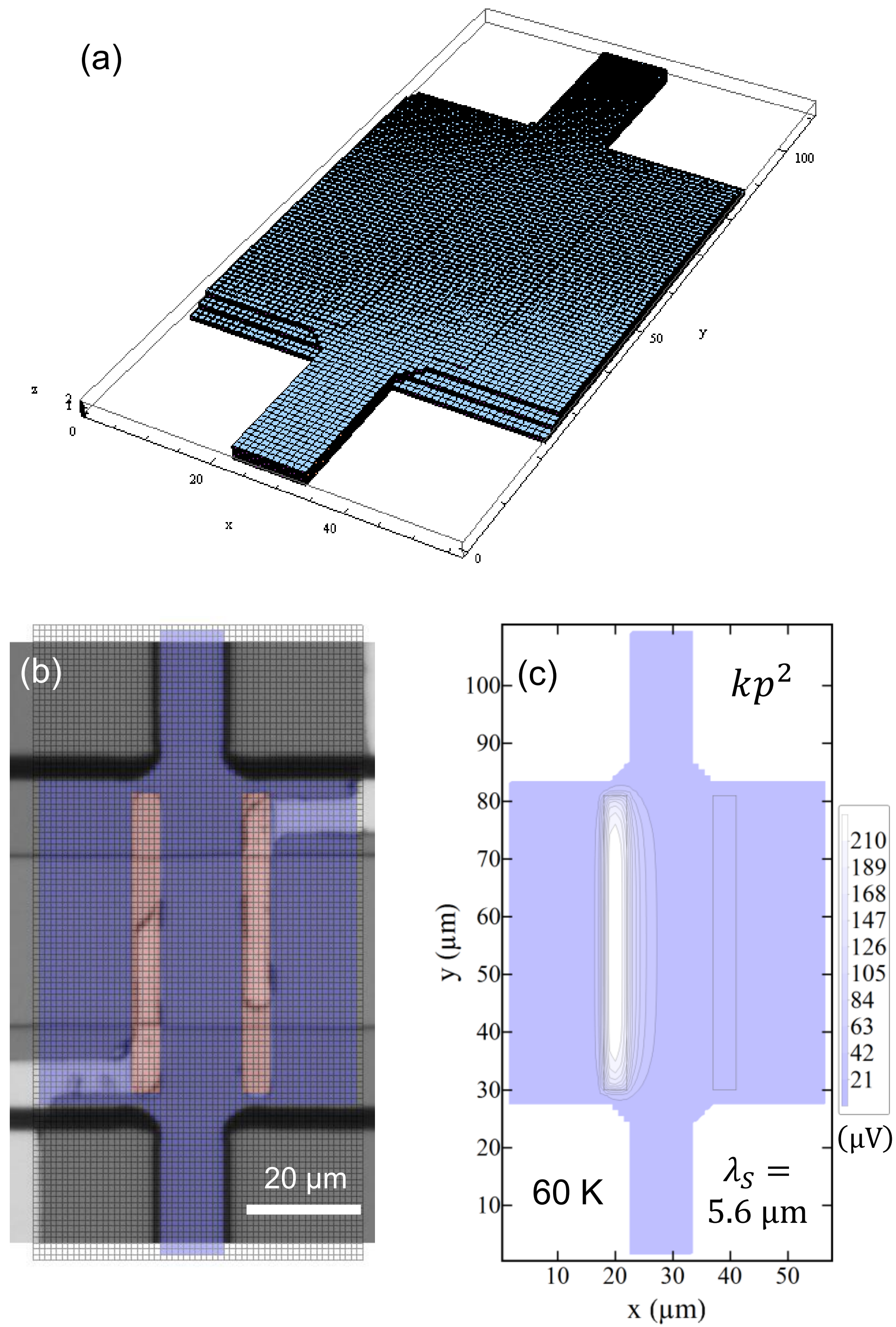

Figure 4.10: (a) Three-dimensional simulation geometry. (b) Simulation geometry overlaid on top of micrograph of device. Blue (red) indicates channel (interface) region. (c) Contour plot of kp^2 obtained from simulation at 60 K.

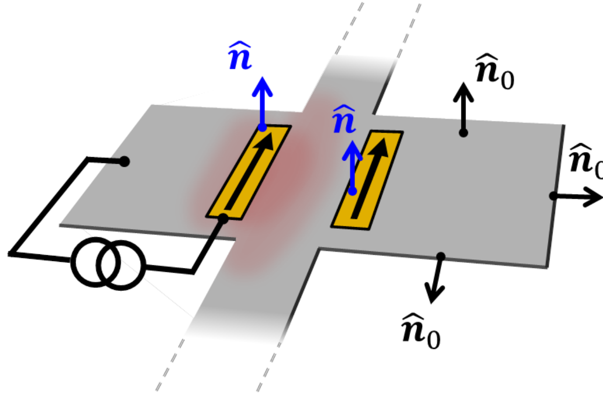

Figure 4.11: Definitions of vectors $\hat{n}_0$ normal to all surfaces of the device and $\hat{n}$ normal to the contact regions.

contact B.

Under steady-state conditions ($0 = -\partial\rho/\partial t = \vec{\nabla}\cdot\vec{j}$), Eq. 4.7 becomes

$$\nabla^2\Phi = \nabla^2\left[k\left(p\right)p^2\right]. \tag{4.12}$$

Using $\hat{n}_0$ to denote the unit vector normal to any given point on the surface of the device, the constraint on current density is expressed as

$$\hat{n}_0\cdot\vec{j} \quad = \quad j_0 \tag{4.13}$$

to match the applied current bias j_0. For surface regions which are not part of the source or drain contacts, $j_0 = 0$. Within the highly doped n^+ regions, denoted by normal unit vector $\hat{n}$, the in-plane components of the electric field must vanish:

$$\hat{n}\times\vec{\nabla}\Phi = \vec{0}. \tag{4.14}$$

The vectors $\hat{n}_0$ and $\hat{n}$ are shown in Fig. 4.11. The electrostatic potential satisfying the conditions imposed by Eqs. 4.12, 4.13, and 4.14 may be written as:

$$\phi = \phi_0 + k\left(p\right)p^2 + \phi_b. \tag{4.15}$$

The variable ϕ_0 represents the electrostatic potential required to exactly satisfy Eq. 4.13 in the *absence* of a spin accumulation, i.e. $\hat{n}\cdot\vec{\nabla}\phi_0 = -j_0/\sigma$. The second term arises as a result

of the spin-generated EMF when $p \neq 0$. While these two terms alone satisfy conditions given in Eqs. 4.12 and 4.13, they do not satisfy the boundary condition in Eq. 4.14 which requires each contact to remain at an equipotential. For this reason we include an additional term ϕ_b to represent the additional shift in the electrostatic potential due to the presence of the highly doped regions. The physical significance of this term is further discussed below.

Using Eq. 4.15, the problem may be redefined in terms of Laplace's equation with Neumann boundary conditions as

$$\nabla^2 \phi_b = 0 \tag{4.16}$$

$$\hat{n}_0 \cdot \vec{\nabla} \phi_b = 0 \tag{4.17}$$

$$\hat{n} \times \vec{\nabla} \phi_b = -\hat{n} \times \vec{\nabla} \left[k(p) \, p^2 \right] \tag{4.18}$$

corresponding to Eqs. 4.12, 4.13, and 4.14 respectively. It is instructive to convert this last expression from a tangential Neumann boundary condition to a Dirichlet boundary condition by performing a line integral of Eq. 4.18 along the surface denoted by $\hat{n}$. Up to an arbitrary integration constant which may be neglected, we obtain

$$\left[\phi_b = -k(p) \, p^2 \right]_{\hat{n}} . \tag{4.19}$$

This means that the effect of the highly doped contact regions is to enforce a voltage profile equal to $-kp^2$ to cancel the spin-generated EMF and maintain the entire contact region at an equipotential. From Eqs. 4.16, 4.17, and 4.19, the value of ϕ_b in the bulk of the device may be determimed by standard Laplace relaxation techniques. Fig. 4.12(a) shows the results of performing such a calculation on the spin accumulation profile shown in Fig. 4.10(b). Fig. 4.12(b) shows the sum of both contributions, i.e. $k(p) \, p^2 + \phi_b$, which is constant within the contact regions as required.

The significance of $\phi_b \neq 0$ is two-fold. First, it means that the spin-generated EMF causes an electrostatic potential shift even in regions where $p = 0$. As shown in Fig. 4.12(b), the large aspect ratio of the contacts (1:11) causes the potential drop *across* the width of the channel to be different than *along* its length. This results in an observable voltage difference between the Hall arm contacts C and the remote counter-electrode H. Second, a non-zero ϕ_b gives rise to (divergenceless) eddy currents as can be seen by substituting Eq. 4.15 into Eq. 4.7 to obtain:

$$\vec{j}_b = \vec{j} + \sigma \vec{\nabla} \phi_0 = -\sigma \vec{\nabla} \phi_b . \tag{4.20}$$

These eddy currents, denoted by $\vec{j}_b$, flow along the length of the contact and circulate into the bulk. The vectors in Fig. 4.12(a) show the path of the eddy currents as determined

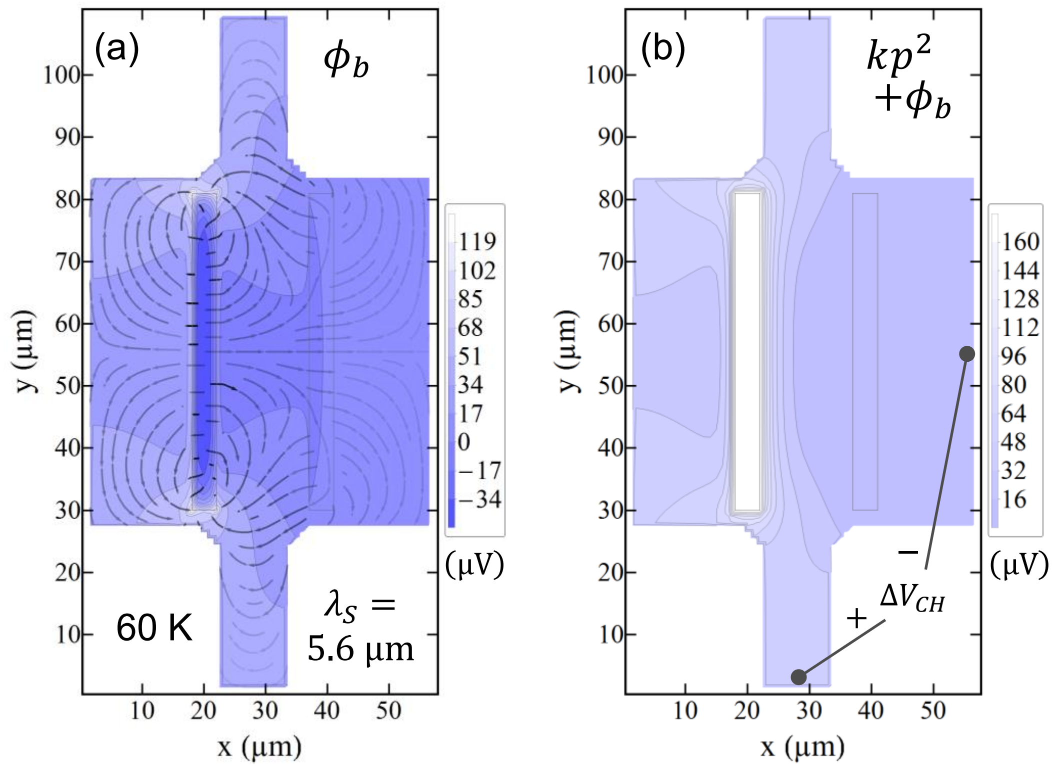

Figure 4.12: (a) Contour plot of ϕ_b obtained from Laplace relaxation. Vectors show spin-EMF induced eddy currents $\propto \vec{\nabla}\phi_b$. (b) Contour plot of $kp^2 + \phi_b$ showing the equipotential in the contact regions and potential drop between Hall arm contacts C and remote counter-electrode H.

from simulation. The influence of the eddy currents on the profile of the spin accumulation is negligible since $kp^2 \ll D/\nu$.

Since the Hall arms constituting contact C and the counter-electrode H are both located many spin diffusion lengths away from the injection region, we may take $p \approx 0$ when evaluating the potential difference between these two points. This means that $\phi - \phi_0 \approx \phi_b$ is the relevant quantity for comparison to the experimentally observed Hanle magnitude. For small polarizations, the prefactor k is independent of p, allowing the spin accumulation profile determined from Eq. 4.11 to be directly scaled to match the experimental value ΔV_{CH} without further calculation. For large polarizations ($p \gtrsim 0.3$), however, the coefficient k itself may be a function of p. In this case, since $k(p)$ depends (weakly) on position, it is necessary to iteratively repeat the Laplace relaxation after each rescaling of the polarization profile until converge is attained.

4.7 Temperature dependence

The procedure outlined above allows p_{inj} to be determined from the experimentally observed electrostatic shift ΔV_{CH} with no adjustable parameters. The only parameter assumed from literature is the electron effective mass $m^\star_{\mathrm{GaAs}} = 0.067 m_0$ used to define the density of states for calculation of both $k(p)$ and the diffusion constant. All other inputs to the model are quantified experimentally.

Fig. 4.13(a) shows p_{inj} as a function of temperature for both a Co_2MnSi device (3×10^{16} cm^{-3}) and an Fe device (5×10^{16} cm^{-3}). Notably, these polarization values were obtained solely from bulk semiconductor parameters and are independent of any assumptions about the efficiency of spin-dependent tunneling at the heterojunctions.

The current polarization required to generate the observed electrostatic potential shift ΔV_{CH} at each temperature is shown in Fig. 4.13(b). Note that although the Co_2MnSi/n-GaAs device generates a larger spin accumulation at the injector than the Fe/n-GaAs device, the current polarizations are roughly equal. Because of the slightly higher channel doping of the Fe/n-GaAs device, an equivalent spin injection rate corresponds to a smaller fractional polarization. (The spin diffusion lengths in both devices did not differ appreciably. At 60 K, λ_s was 5.6 µm for the Co_2MnSi/n-GaAs device and 4.9 µm for the Fe/n-GaAs device.) This highlights the importance of properly accounting for the channel properties when evaluating device performance. The fact that both ferromagnetic materials generate the same injected current polarization supports the idea of a saturation regime as discussed earlier in Sec. 3.2.3.

We finally note that the spin-generated EMF will also contribute to the traditional FM

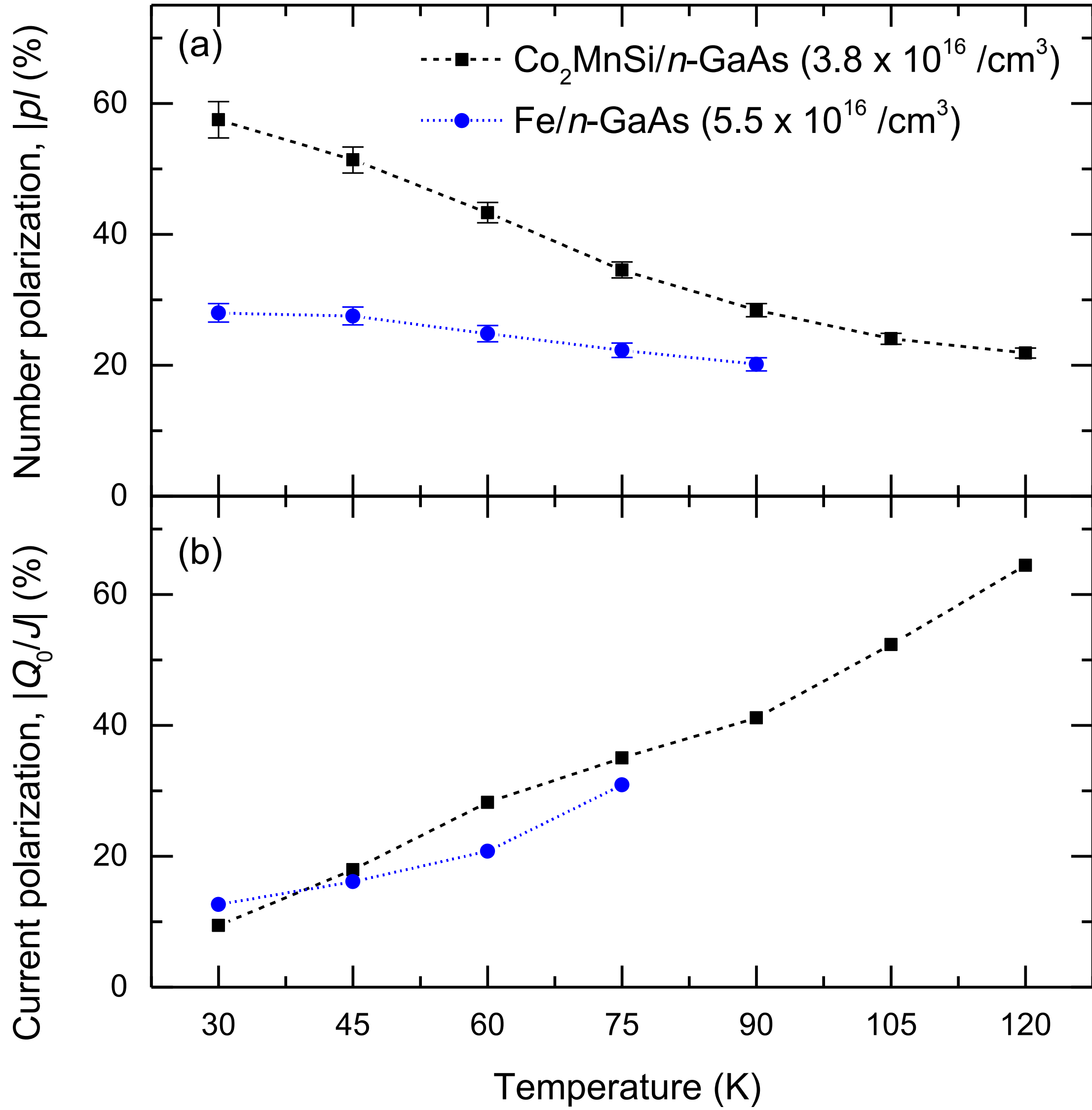

Figure 4.13: (a) Number polarization and (b) current polarization vs. temperature at injector contact B determined from the magnitude of the spin-generated EMF (Co_2MnSi: black squares, Fe: blue circles).

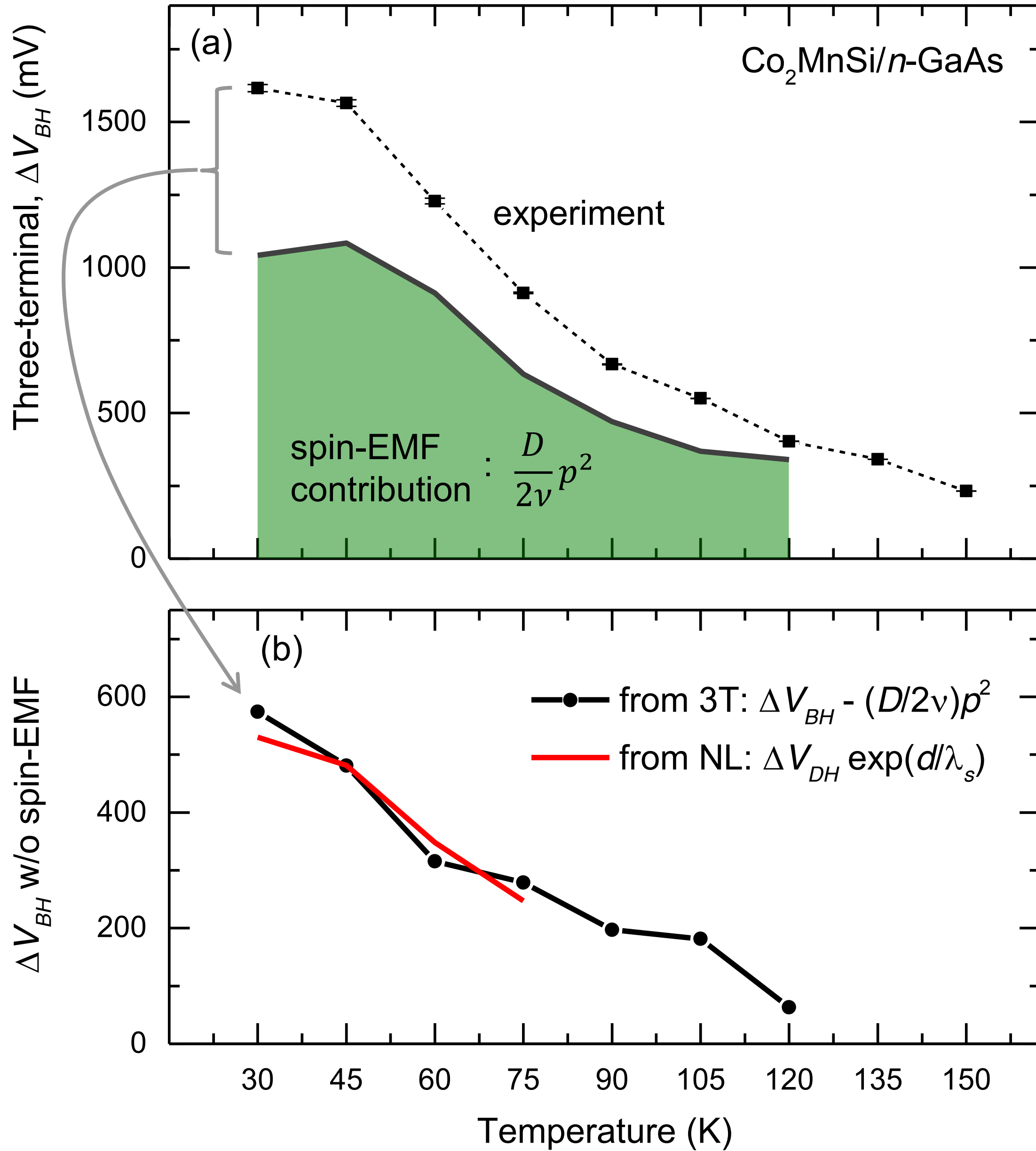

Figure 4.14: (a) Magnitude of 3T signal as a function of temperature. Green shaded region indicates the estimate contribution from the spin-EMF. (b) 3T magnitude after subtracting the contribution from the spin-EMF. Red line shows the expected contribution determined from (ferromagnetic) non-local measurements.

detection signals, the three-terminal Hanle signal[78, 73] in particular. As was shown in Sec. 3.4, the potential difference observed between a tunneling electrode and a remote reference contact will include a contribution which depends the *average* electrochemical potential (as opposed to the *weighted* average). At any given point within the device, we can express this shift as

$$\begin{aligned} \Delta\zeta_{avg} &= \frac{\zeta_\uparrow + \zeta_\downarrow}{2} - \zeta_0 && (4.21) \\ &= \Delta\mu_{avg} - e\left(\phi - \phi_0\right) && (4.22) \end{aligned}$$

where $\zeta_{\uparrow(\downarrow)} = \mu_{\uparrow(\downarrow)} - e\phi$ denotes the electrochemical potential for each spin orientation as before. We assume the influence of the eddy currents on the potential at the interface to be small, such that $\phi - \phi_0 \approx kp^2$. Using the expression for k above (Eq. 4.10), as well as Taylor-expanding the chemical potentials within $\Delta\mu_{avg}$ yields

$$\phi - \phi_0 \approx \frac{1}{2e}\left(\frac{\partial\mu}{\partial n}n + \frac{\partial^2\mu}{\partial n^2}\right)p^2 \tag{4.23}$$

and

$$\Delta\mu_{avg} \approx \frac{1}{2}\frac{\partial^2\mu}{\partial n^2}p^2 \tag{4.24}$$

Note that the contribution originating from the non-constant density of states drops out of the expression for the average electrochemical potential:

$$\Delta\zeta_{avg} = -\frac{1}{2e}\frac{\partial\mu}{\partial n}n = -\frac{D}{2\nu}p^2 \tag{4.25}$$

The magnitude of the three-terminal (3T) signal may thus be decomposed as

$$\Delta V_{\mathrm{BH}} \approx (D/\nu)\left(\eta p_{inj} + p_{inj}^2/2\right) \tag{4.26}$$

The first term originates from the usual spin-dependence of the interfacial tunneling conductance discussed in 3.4. The second term is the contribution from the spin-generated EMF given in Eq. 4.25 (note the sign change as per Fig. 3.15). This contribution must be taken into account when interpreting FM detection signals in the regime of large spin polarization, i.e. when $p \gtrsim \eta$.

Fig. 4.14(a) compares the experimental magnitude of the 3T signal with the expected contribution from the spin-generated EMF. At higher temperatures in particular, the spin-EMF constitutes the dominant contribution. The remainder of the signal magnitude is attributable to the first term of Eq. 4.26, and is shown by the black points in Fig. 4.14(b).

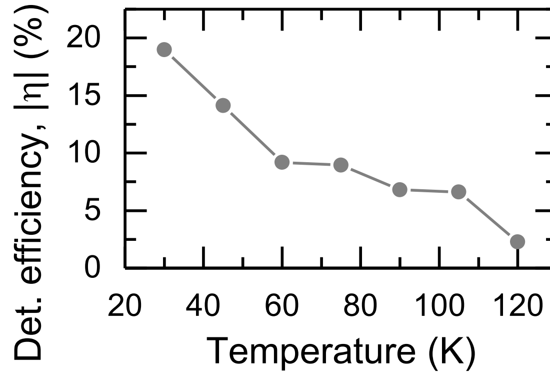

Figure 4.15: Detection efficiency as a function of temperature extracted from Eq. 4.26.

For comparison, the red line shows the magnitude of the non-local signal multiplied by $\exp(d/\lambda_s)$ at each temperature. The agreement in magnitude[2] as a function of temperature provides compelling evidence that the decomposition presented in Eq. 4.26 is correct.

It is worth further noting that estimating the calculated spin-EMF contribution to the 3T signal magnitude in this manner is extremely robust against systematic errors in the prefactor k. The relationship between the shorted-Hall signal ΔV_{CH} and the spin-EMF contribution to the 3T signal depends only the geometry of the device and the profile of the spin accumulation. The magnitude of the prefactor only influences the calculation when the polarization is large such that k itself becomes a function of p and thereby of position, as discussed in the next section.

Knowing p_{inj} from the shorted-Hall measurements of ΔV_{CH} and the magnitude of the 3T signal ΔV_{BH} allows us to extract the magnitude[3] of the detection efficiency η from Eq. 4.26 as

$$|\eta| = \frac{\Delta V_{BH}}{D/\nu} \frac{1}{p_{inj}} - \frac{p_{inj}}{2}. \tag{4.27}$$

Fig. 4.15 shows the extracted value of $|\eta|$ as a function of temperature. While the slight decrease at higher temperatures is not perhaps a surprising result, it provides a stark contrast to the behavior of the injected current polarization in Fig. 4.13(b) which *increases* at higher temperatures.

[2]Although no additional scaling was performed, the agreement here is fortuitous. We are mostly interested in the trend with temperature. As noted earlier, the sign of η inverts under the large forward bias conditions where these 3T measurements were taken. The results shown in Fig. 4.26(b) demonstrate that the detection efficiency has a nearly identical magnitude in both the biased and unbiased cases, despite having an opposite sign.

[3]As derived in Sec. 3.4, the sign of p_{inj} itself depends on η. The overall ambiguity in sign may be resolved by the oblique Hanle measurements presented in Sec. 4.4.

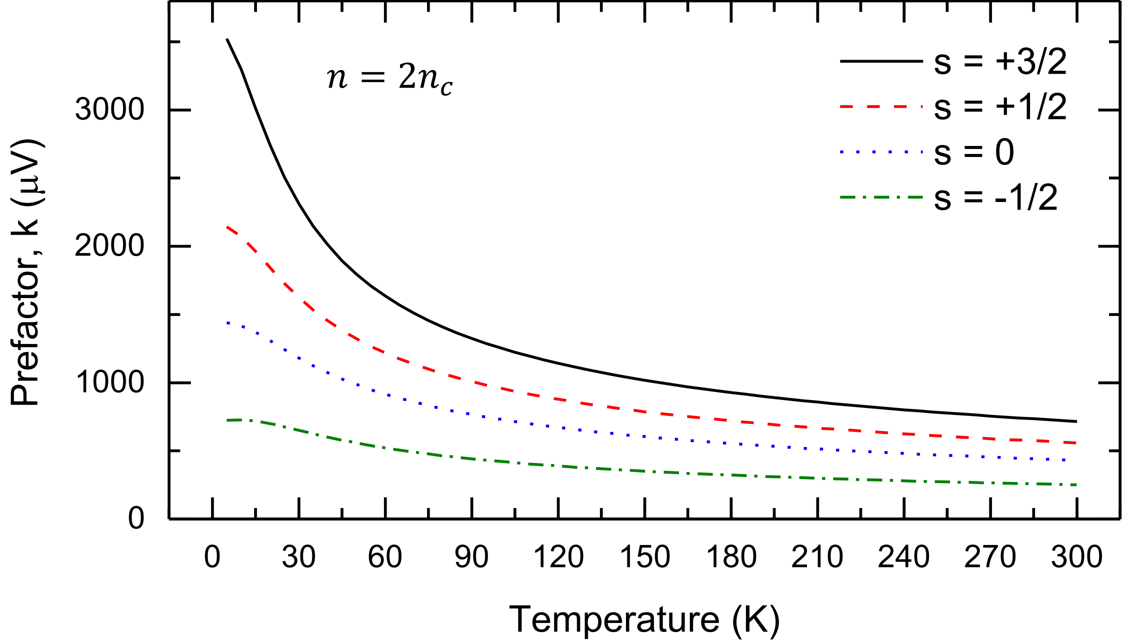

Figure 4.16: Spin-EMF prefactor for different scattering mechanisms.

4.8 Corrections

In this section we provide a few additional comments on further corrections to the theory of the spin-generated EMF presented in Sec. 4.1. For the polarization values presented in Fig. 4.13, we estimate the combined influence to be no larger than ≈ 15%. The primary utility in discussing these further contributions is to identify under what circumstances the systematic errors introduced will influence interpretation of experimental trends vs. temperature, bias, doping, etc.

We first examine the effect of allowing the mobility to be energy dependent such that $\nu \propto \varepsilon^s$ as before. Assuming a parabolic dispersion, the expression for the prefactor k may then be written as

$$k = \frac{D}{2\nu}\Theta = \frac{k_B T}{2e}\left[\frac{\mathcal{F}_{\frac{1}{2}}(\xi)}{\mathcal{F}_{-\frac{1}{2}}(\xi)}\right]^2\left[\frac{\mathcal{F}_{-\frac{1}{2}+s}(\xi)}{\mathcal{F}_{\frac{1}{2}+s}(\xi)} - \frac{\mathcal{F}_{-\frac{3}{2}}(\xi)}{\mathcal{F}_{-\frac{1}{2}}(\xi)}\right]. \tag{4.28}$$

Fig. 4.16 shows the magnitude of k for several values of the energy exponent s. The black solid line corresponds to ionized impurity scattering ($s = +3/2$) which is the mechanism most applicable to our samples over the temperature range measured. Including this contribution roughly doubles the magnitude of the spin-EMF compared to the blue dotted line ($s = 0$). However, as noted in Sec. 2.4, Hall and magnetoresistance measurements on these

samples indicate a weaker energy dependence than implied by ionized impurity scattering.

As noted in Ch. 2, band-tail corrections to the density of states may become significant at lower temperatures. This is illustrated in Fig. 4.17 where we have plotted the spin-EMF prefactor k as a function of temperature for the four models discussed in Sec. 2.3. With the notable exception of the Blakemore model (which gives the wrong sign), the only significant deviation occurs for temperatures $k_B T \lesssim \varepsilon_F$. At low temperatures, including states in the band tail causes an overall increase in the compressibility of the system, thereby decreasing the magnitude of the spin-generated EMF.

For large polarizations ($p \gtrsim 0.3$), the expansion leading to Eq. 4.10 is insufficient, and it becomes necessary to include the polarization dependence of the prefactor k. In this sense, the polarization dependence of k is analogous to the Thomson effect in which the Seebeck coefficient itself is allowed to vary with temperature. If we assume $\partial\mu_{diff}/\partial p$ to be a slow varying function of position, it can be shown that

$$k\left(p\right) = \frac{1}{2}\frac{\partial\mu_{diff}}{\partial p} + \frac{\Delta\mu_{avg}}{p^2}, \tag{4.29}$$

where $\Delta\mu_{avg} = \frac{1}{2}\left(\mu_\uparrow + \mu_\downarrow\right) - \mu_0$ and $\mu_{diff} = \frac{1}{2}\left(\mu_\uparrow - \mu_\downarrow\right)$. The functional dependence of the chemical potentials $\mu_\uparrow$ and $\mu_\downarrow$ on the polarization may be obtained by numerically inverting the relation $n_\alpha = \frac{1}{2} n_Q\left(\xi_\alpha\right)\mathcal{F}_{1/2}\left(\xi_\alpha\right)$. As the polarization approaches unity, chemical potential of the minority species is pushed far into the band gap of the semiconductor, causing a large (negative) value of $\Delta\mu_{avg}$ which eventually reverses the sign of the spin-generated EMF.

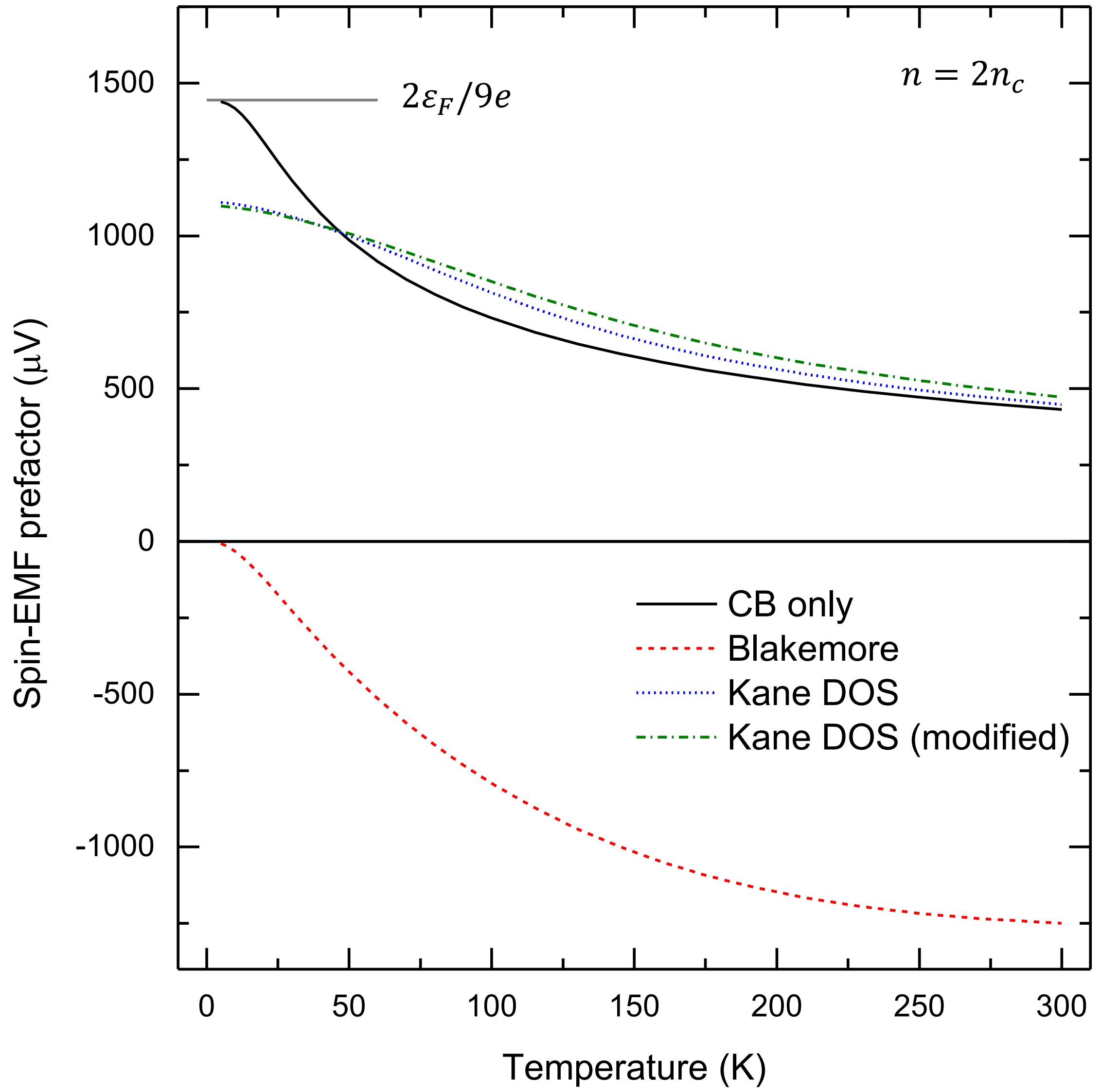

Figure 4.17: Prefactor for the spin-generated EMF as a function of temperature for the four models discussed in Sec. 2.3.

Chapter 5

Hyperfine-induced spin relaxation and a Hall effect

While the previous chapter focused on what may be called a *longitudinal* asymmetry in the transport of spin-up and spin-down electrons, this chapter examines spin-dependent Hall effects which appear a result of *transverse* asymmetries in the transport parameters. In particular, we present measurements of a large spin-dependent Hall effect which develops in the regime of large spin polarization as a result of hyperfine interactions with dynamically polarized nuclei. An additional manifestation of this effect is the presence of an additional source of anisotropic spin-relaxation.

It is well-established that spin-orbit coupling in GaAs leads to an equal yet opposite deflection of spin-up and spin-down currents, thus converting a fraction of every longitudinal charge currents into a transverse spin current and vice-versa. The former process is known as the (direct) spin Hall effect and the latter is the inverse spin-Hall effect (ISHE). The ISHE may be written in a concise phenomenological form[49] as

$$j_i^H = \gamma \epsilon_{ijk} q_{jk} \tag{5.1}$$

where j_i^H denotes i-th component the Hall current generated by the spin current tensor q_{jk}. As in Sec. 3.1.4, the first index of q_{jk} indicates the direction of flow and the second index indicates the spin orientation. ϵ_{ijk} denotes the anti-symmetric Levi-Civita symbol. The phenomenological prefactor γ is known as the spin-Hall ratio (or spin-Hall angle). For n-GaAs, the dominant source of spin-dependent deflection arises due to Mott-scattering from ionized impurities. Both theory[79, 80] and experiment[81, 82, 83, 84, 85] yield spin-Hall ratios on the order of $\gamma \approx 10^{-3}$.

As we demonstrate below, the spin-Hall ratio may be greatly enhanced in the presence of

hyperfine interactions with polarized nuclei. Not unlike the story developed in the previous chapter, devices operating in the large polarization regime exhibit additional experimental signatures when the chemical potential splitting becomes comparable to other energy scales in the problem. In Sec. 5.1 we describe the local Hall device geometry used to identify spin-dependent transport asymmetries. We highlight the rather significant deviation from expectations based on the Mott scattering picture mentioned above. Sec. 5.2 introduces a pulsed measurement technique which allows the degree of nuclear polarization to be controlled independently of the electron spin polarization. We employ this technique to clearly illustrate the central role of the nuclear polarization in generating the enhanced transport asymmetry. In Sec. 5.4, we present a mechanism to explain the enhancement which also predicts the existence of an additional source of spin relaxation. This is used to reproduce several of the intricate signatures observed in the oblique Hanle measurements of Sec. 5.5.

5.1 Device design: local Hall geometry

Fig. 5.1(a) shows the geometry of our local Hall devices. A single ferromagnetic (FM) contact is positioned over the center of a pair of long semiconducting Hall arms. A spin accumulation is generated in the center of the device by applying a current bias between the central FM contact and *both* counter electrodes as indicated by the gray arrows in Fig. 5.1(a). Balancing current between both of the side channels helps cancel unwanted charge-based contributions to the voltage difference observed along the Hall arms. We may also use this device to observe a three-terminal signal as shown in the wiring diagram of Fig. 5.1(b) where the central FM contact functions simultaneously as both an injector and detector of spin accumulation. In this configuration, both Hall arms are shorted together to form the reference electrode for the voltmeter. The advantage of this approach over a lateral non-local geometry is the larger signal and simpler interpretation.

Fig. 5.1(c) shows a micrograph of a completed Fe/n-GaAs device. Note that the alignment tolerance is more critical here than in the case of the lateral spin-valve devices. The size of the central contact is nominally 5 µm x 52.5 µm. The magnetization of the central contact may be fabricated[1] to lie either parallel or perpendicular to the Hall arms as shown in Fig. 5.2(a) and (b) respectively. The spin current flow is predominately along the vertical direction normal to the plane of the device. This is set by the boundary condition of the current bias being applied to the central contact (Sec. 3.4). The Hall arms detect

[1] The dominant component of the magnetic anisotropy is a uniaxial contribution coming from the epitaxial interface with GaAs. Even for large aspect ratios, the contribution from the in-plane shape anisotropy is negligible.

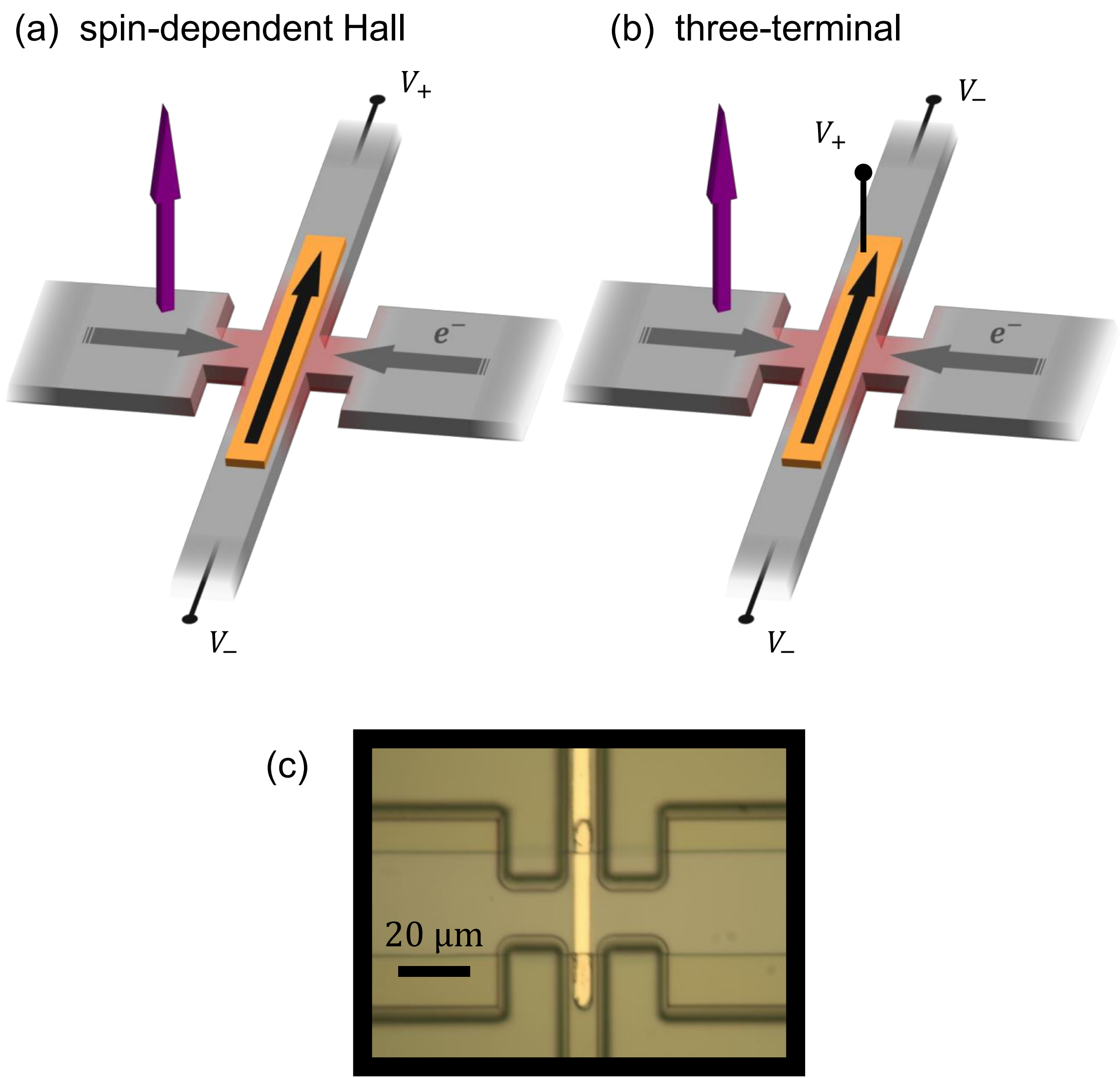

Figure 5.1: Local Hall geometry wired for (a) spin-dependent Hall and (b) three-terminal measurements. (c) Micrograph of Fe/n-GaAs sample (UMN019-02I).

one component of the transverse deflection as a voltage. Applying an out-of-plane magnetic field rotates the spin ensemble and gives rise to a Hanle effect in the local Hall arms.

Eq. 5.1 allows us to make a crude estimate of the expected magnitude and line-shape of the Hanle curves we would expect to observe. Ignoring drift effects on the spin diffusion length allows us to write the spin current as simply

$$Q = \lambda_s p'. \tag{5.2}$$

We impose the following boundary conditions at the top ($z = 0$) and bottom ($z = t$) of the device:

$$Q\left(z=0\right) = Q_0 \tag{5.3}$$

$$Q\left(z=t\right) = 0 \tag{5.4}$$

and look for a solution of the form

$$p\left(z\right) = p^{+} \exp\left(x\sqrt{1+i\gamma B\tau_s}\right) + p^{-} \exp\left(x\sqrt{1+i\gamma B\tau_s}\right). \tag{5.5}$$

We are interested in the average vertical spin current flowing in the device. It can be shown that the solution to the boundary conditions above yields

$$\bar{Q} = \frac{1}{t}\int_0^t Q\left(z\right) dz = Q_0 \frac{\tanh\left(\frac{t}{2\lambda_s}\sqrt{1+i\gamma B\tau_s}\right)}{\frac{t}{\lambda_s}\sqrt{1+i\gamma B\tau_s}}. \tag{5.6}$$

Note that the cross product in Eq. 5.1 implies that spins will be deflected along the axis which is perpendicular to both their orientation and flow direction. This allows us to estimate the Hall signal in the parallel and perpendicular devices as

$$\Delta V_{\parallel} \approx \mathcal{I}m\left[\frac{\bar{Q}}{Q_0}\right]\gamma\alpha j\rho_0 l \tag{5.7a}$$

$$\Delta V_{\perp} \approx \mathcal{R}e\left[\frac{\bar{Q}}{Q_0}\right]\gamma\alpha j\rho_0 l \tag{5.7b}$$

where $\alpha \approx 0.2$ is the spin injection efficiency, $j \approx 760$ A/cm^2 is the current bias, $\rho_0 \approx$ 30 mΩ cm is the channel resistivity, and $l = 50$ µm is the length of the contact. Figs. 5.2(c) and (d) show the results of evaluating Eqs. 5.7a and 5.7b respectively. As a function of applied magnetic field, we expect then to observe even and odd quasi-Lorentzian line-shapes with a peak-to-peak voltage of roughly 10 µV and a width of ≈ 500 Oe. More rigorous calculations do not significantly alter these estimates.

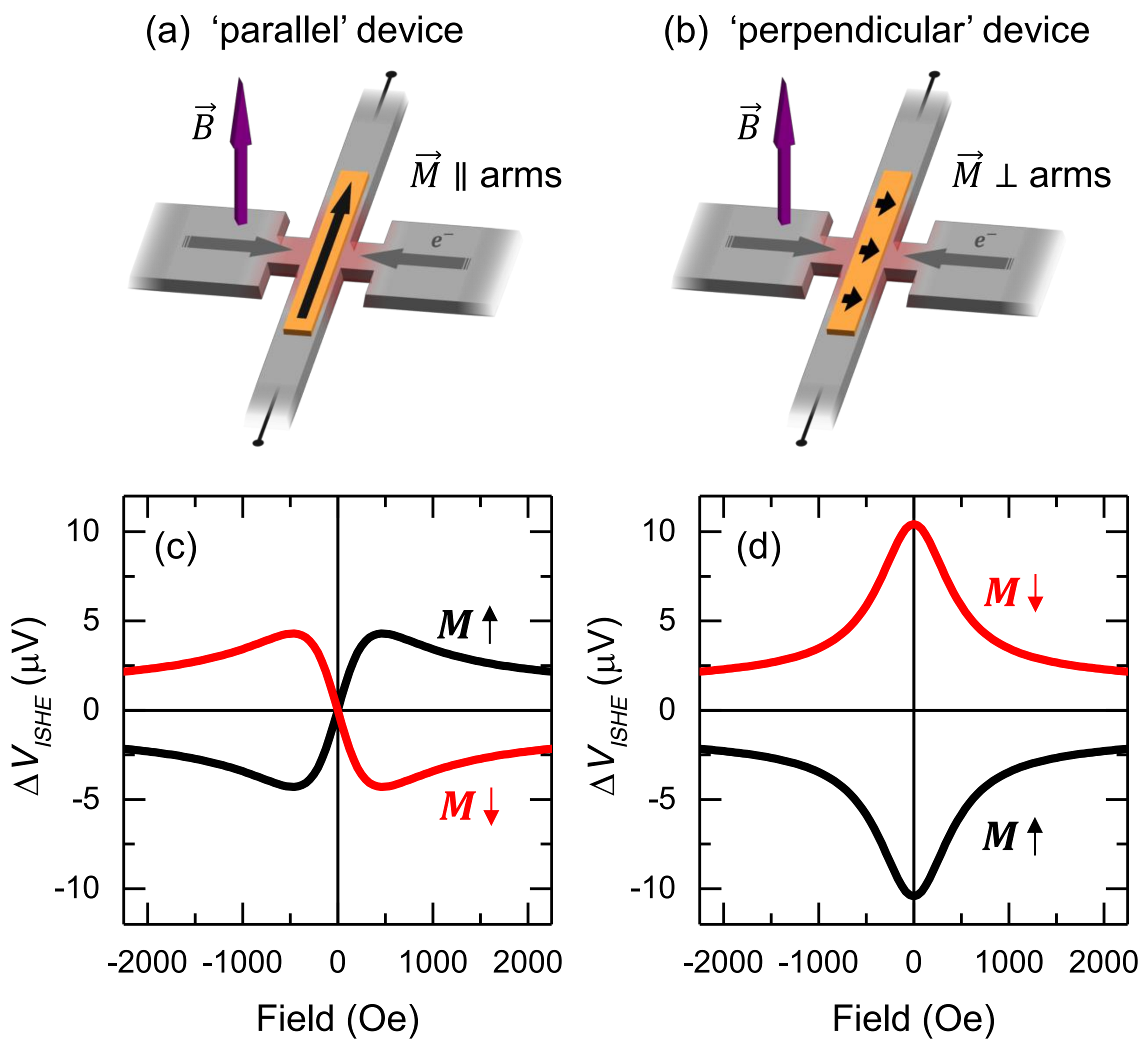

Figure 5.2: (a, b) ‘Parallel’ and ‘perpendicular’ device geometries. (c, d) Expected magnitude and width of Hanle curves.

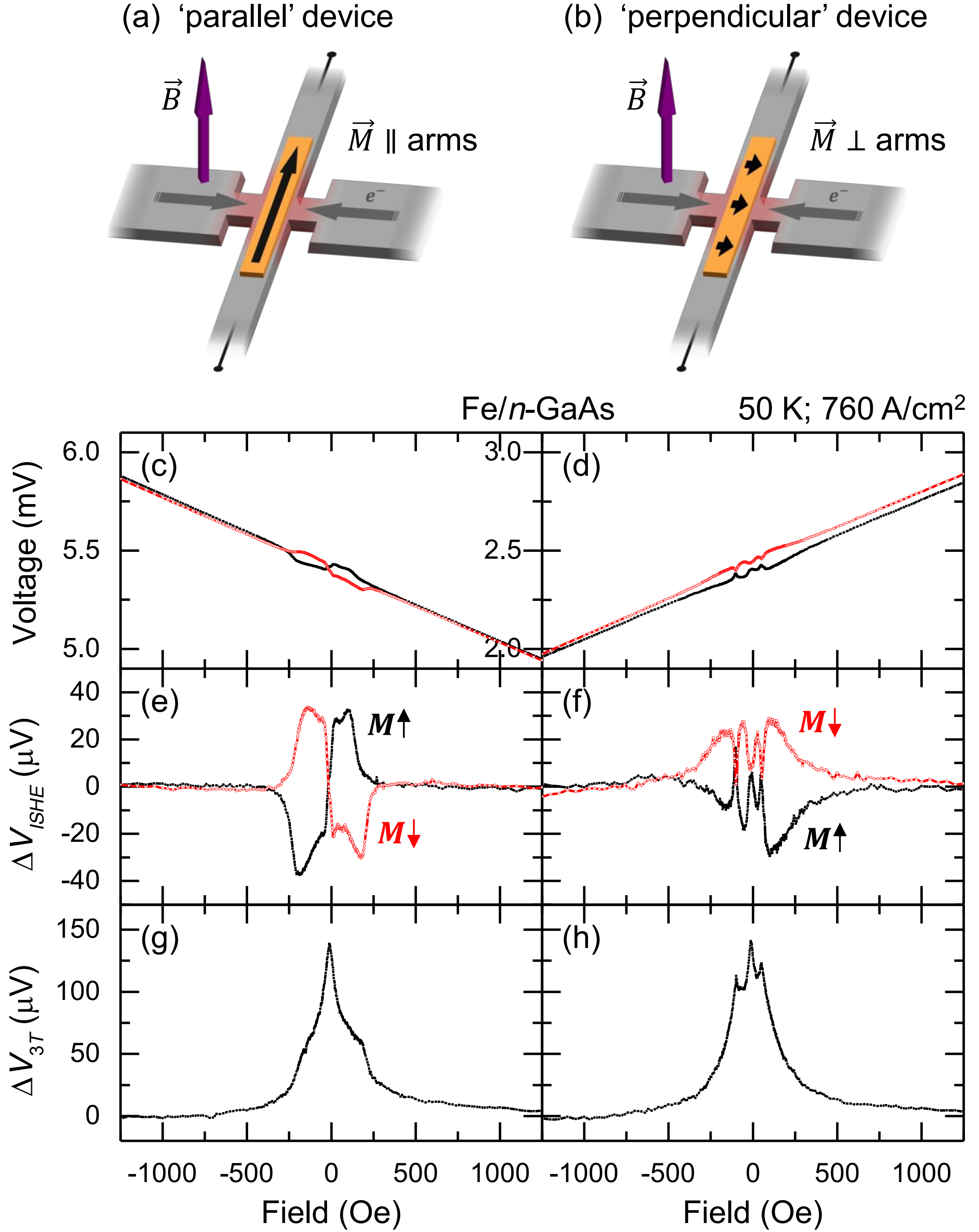

Figure 5.3: (a, b) 'Parallel' and 'perpendicular' device geometries. (c, d) Raw spin-dependent Hall data. (e, f) Spin-dependent Hall data after removal of quadratic background. (g, h) Three-terminal measurement under identical conditions.

These predictions stand in stark contrast to the experimental data presented in Fig. 5.3. These data were obtained on an Fe/n-GaAs (UMN019-02) at 50 K with a current bias of 760 A/cm^2. The raw curves shown in Figs. 5.3(c) and (d) correspond to the parallel and perpendicular devices shown in Figs. 5.3(a) and (b) respectively. The black and the red curves indicate different magnetization states of the central FM contact which may be set prior to the experiment by applying an in-plane field along the FM easy axis. A second-order polynomial was subtracted from of each curve individually to obtain the curves shown in Figs. 5.3(e) and (f). Note that the signal size obtained on the parallel device is nearly an order of magnitude larger than our estimate and its width is significantly narrower. The perpendicular device was expected to have its maximum signal at zero applied field, but instead exhibits a minimum. As the polarization is increased by measuring at low temperatures or higher biases, the discrepancy with the usual ISHE model expressed in Eq. 5.1 increases further.

For reference, the three-terminal signal for each case is shown in Figs. 5.3(g) and (h). Note that in the perpendicular case, two additional peaks are visible in the three-terminal signal. These are caused by the ferromagnetic fringe fields of the central contact which influence the orientation of the nuclear system. To avoid such complications, we focus the majority of our discussion on the parallel device geometry of Fig. 5.3(a).

5.2 Pump-probe measurements

Fig. 5.4(a) shows a micrograph of a Co_2MnSi/n-GaAs device used for the measurements in the following sections. The central contact contains an unintentional 2 µm mis-alignment relative to the center of the Hall arms. The ISHE signal obtained at a temperature of 60 K is shown in Fig. 5.4(b) for both magnetization directions. Note that even if the spin injection efficiency was unity, i.e. $\alpha = q/j = 1$, the $\approx$ 400 µV magnitude of this signal would still imply a spin-Hall angle of $\gamma \approx 0.01$ as per the estimation in Eq. 5.7a.

Note that the black and red curves shown in Fig. 5.4(b) are not completely symmetric about the background slope. This can be more clearly seen by directly subtracting the raw data obtained for the two magnetization directions as shown in Fig. 5.4(c) with no additional background subtraction. If instead we add the curves obtained for $\vec{M}+$ and $\vec{M}-$, we obtain the smaller curve shown in 5.4(d). These two curves represent distinct contributions to the Hall signal and have been observed on multiple devices. Although not yet investigated systematically, this even component likely originates from the spin-EMF generated eddy currents discussed in Sec. 4.6 which contribute to the Hall signal upon any non-ideal alignment of the central contact. For the remainder of the discussion below, we

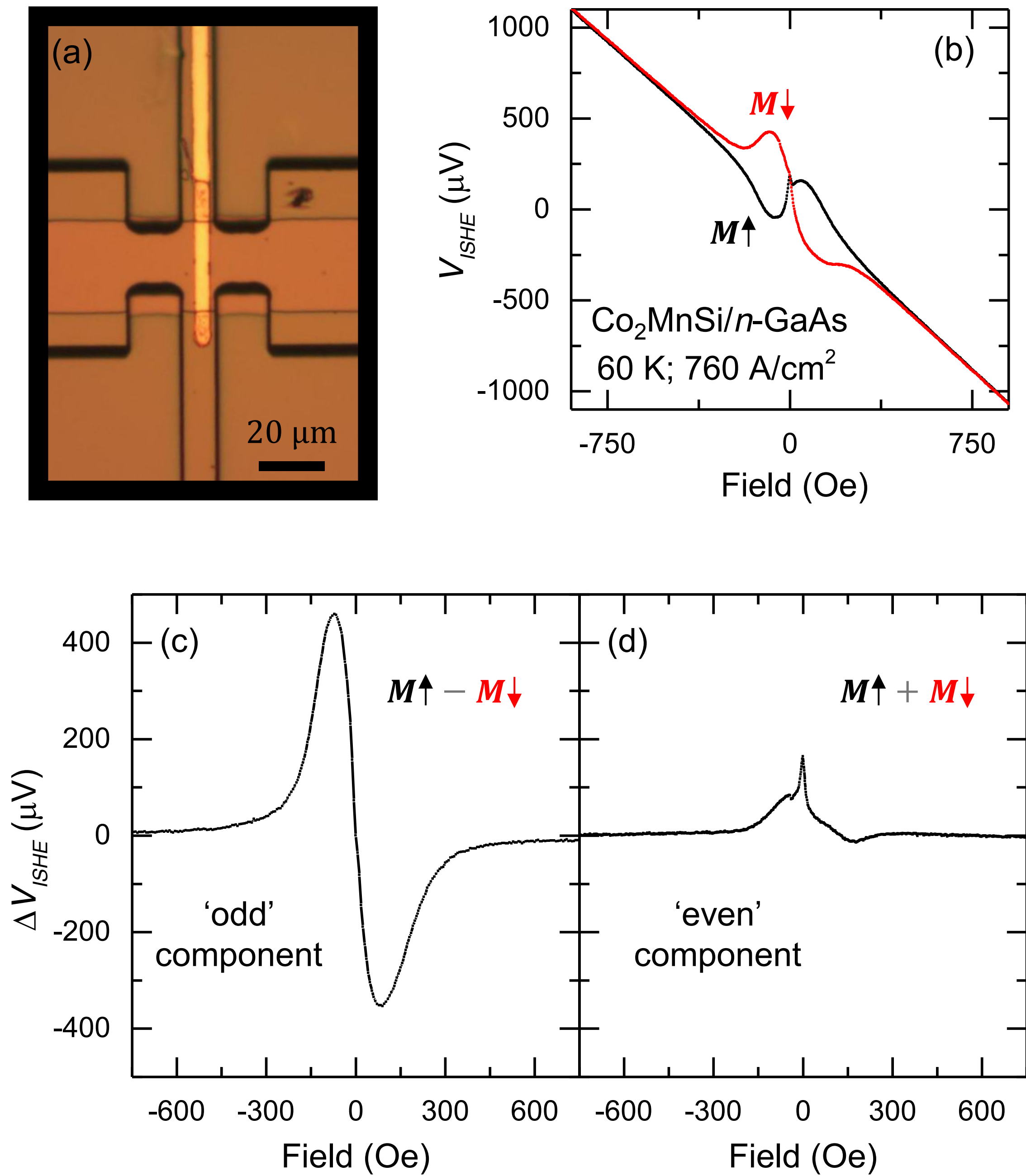

Figure 5.4: (a) Micrograph of mis-aligned Co_2MnSi/n-GaAs sample (UMN023-02I). (b) Raw spin-dependent Hall data for both magnetization directions. (c) Component of signal odd with respect to magnetization. No background subtracted. (d) Component of signal even with respect to magnetization. Second-order polynomial background subtracted.

eliminate this contribution using the symmetrization procedure displayed in Fig. 5.4(c).

To investigate the influence of the nuclear polarization on the ISHE signal, we employ the pulsed measurement technique shown in Fig. 5.5(a). Taking advantage of the vast difference in electron and nuclear spin relaxation time scales ($\tau_s \sim 1$ ns versus $T_1 \gtrsim 1$ s) allows us to control their polarization levels independently. The current bias on the injector is held at $j_{wait} = 0$ A/cm^2 for a duration t_{wait} before each measurement pulse to allow the nuclear polarization to decay. The measurement pulse lasts for a duration of $t_{probe} \approx 25$ ms which is much slower than any electronic timescale, but much faster than the time required for the nuclear system to fully polarize.

Figs. 5.5(a) and (b) show ISHE Hanle measurements obtained for values of t_{wait} varying from steady-state ($t_{wait} = 0$ s) to $t_{wait} = 10$ s. Note that the ISHE component shown in Fig. 5.5(a) decreases dramatically upon elimination of the nuclear polarization. The magnitude of the 3T signal (not shown) remains unaffected by this procedure. Fig. 5.5(c) shows a semi-log plot of the odd and even component magnitudes plotted against t_{wait}. The decay process is fit well using a stretched exponential of the form

$$\Delta V_{ISHE,odd} = V_0 + V_1 \exp\left[\left(\frac{t}{T_H}\right)^{\beta}\right] \tag{5.8}$$

where V_0 is the background contribution from the normal ISHE, V_1 is the nuclear-induced ISHE, T_H is the hyperfine relaxation time and β is an exponent characterizing the decay process. Setting $\beta = 1$ (normal exponential decay) does not result in a good fit as as shown by the blue line in Fig. 5.5(c). Allowing β to be a fitting parameter yields the gray line corresponding to the following extracted parameters: $\beta = 0.56 \pm 0.02$, $T_H = 194 \pm 9$ ms, $V_0 = 15.3 \pm 0.8$ µV and $V_1 = 407 \pm 9$ µV. An exponent of $\beta = \frac{1}{2}$ is commonly observed in the decay rates of disordered spin-systems[86] and appears to be the case here. Assuming the current polarization to be $\alpha \approx 0.3$ from Fig. 4.13(b), the $V_0 \approx 15$ µV ISHE offset which remains after eliminating the nuclear polarization corresponds to a spin Hall ratio of $\gamma \approx 1.3 \times 10^{-3}$. This is in excellent agreement with the theoretical value and prior experimental works. Because $V_1 \gg V_0$, we will ignore the contribution from the 'normal' ISHE in all subsequent calculations.

5.3 Bias dependence

In this section we establish the scaling dependence of the ISHE signal on the electron and nuclear spin polarization levels. We employ the pulsed measurement technique shown in Fig. 5.6. This is similar to the approach of the previous section, but we now allow the application

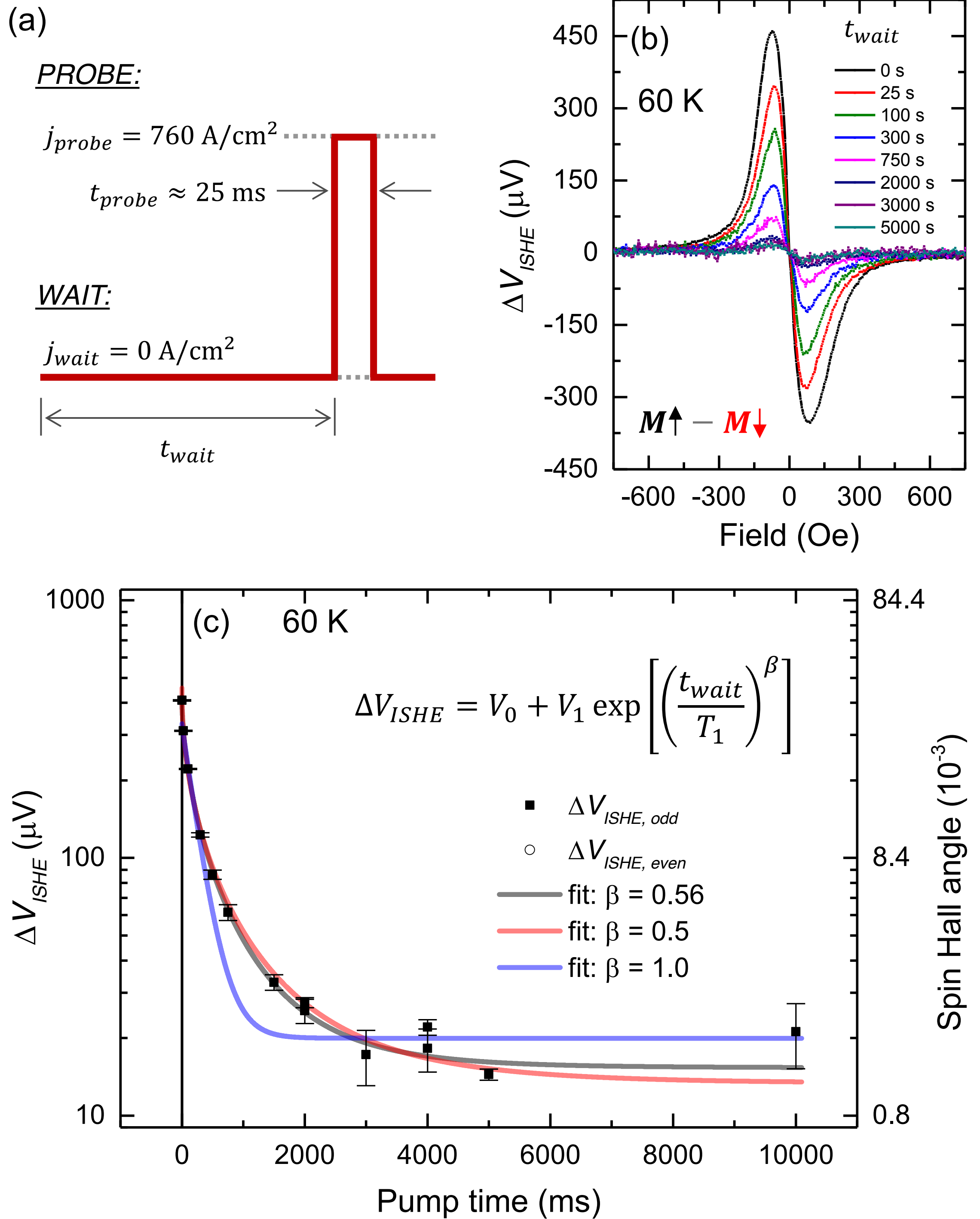

Figure 5.5: (a) Timing diagram for pulsed measurement sequence. (b) ISHE Hanle signal measured for several different wait times. (c) Magnitude of ISHE signal vs wait time fitted to stretched exponential functions with exponents $\beta = 0.56$ (black), $\beta = 0.5$ (red), and $\beta = 1.0$ (blue).

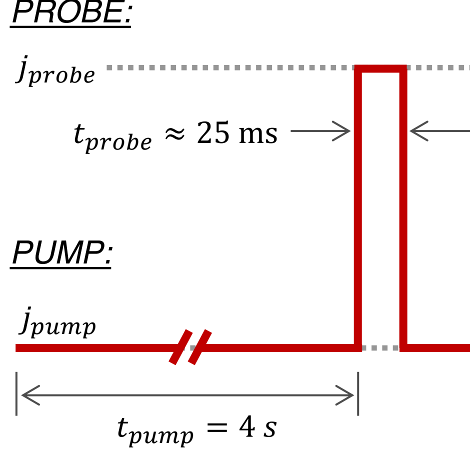

Figure 5.6: Timing diagram for the pump-probe measurement.

of a finite current bias in-between measurement pulses. A current bias of j_{pump} is applied to the central contact for a duration of $t_{pump} = 4$ s, after which a brief current pulse j_{probe} is used to record the ISHE signal before the polarization of the nuclear system changes appreciably from the value set by j_{pump}. In this manner we are able to independently control the magnitude of the electron and nuclear polarization by varying j_{probe} and j_{pump} respectively. The results of this procedure at 60 K are shown in Fig. 5.7(a), where each line represents ISHE Hanle curves taken with a constant value of j_{pump} for various values of j_{probe}.

As discussed in Sec. 3.4, however, the spin injection rate cannot be regarded as being directly proportional to the current bias. The polarization of the injected current depends strongly on the voltage drop across the interface and may be susceptible to additional spin-sinking effects. For this reason, we use the non-local spin valve signal as a proxy for the spin injection rate, similar to the approach adopted in Sec. 4.5. Fig. 5.7(b) shows non-local spin valve data acquired using the device shown earlier in Fig. 4.4(b) which was fabricated on the same chip as the ISHE device in Fig. 5.4(a). The injector and detector contacts had dimensions 5 µm x 52.5 µm with a center-to-center separation of 19 µm. The non-local spin valve magnitude ΔV_{NLSV} was obtained by taking the difference of the non-local voltage observed when sweeping current in the parallel and antiparallel configurations. The solid maroon line in Fig. 5.7(b) shows a windowed average over ten adjacent points. To good approximation, this curve is proportional to the bias dependence of the spin injection rate.

We now use the curve shown in Fig. 5.7(b) to plot our results vs. spin injection rate rather than current bias. Fig. 5.8(a) shows each value of ΔV_{ISHE} plotted against the non-local spin valve magnitude evaluated at the same value of j_{probe}. We observe a clear

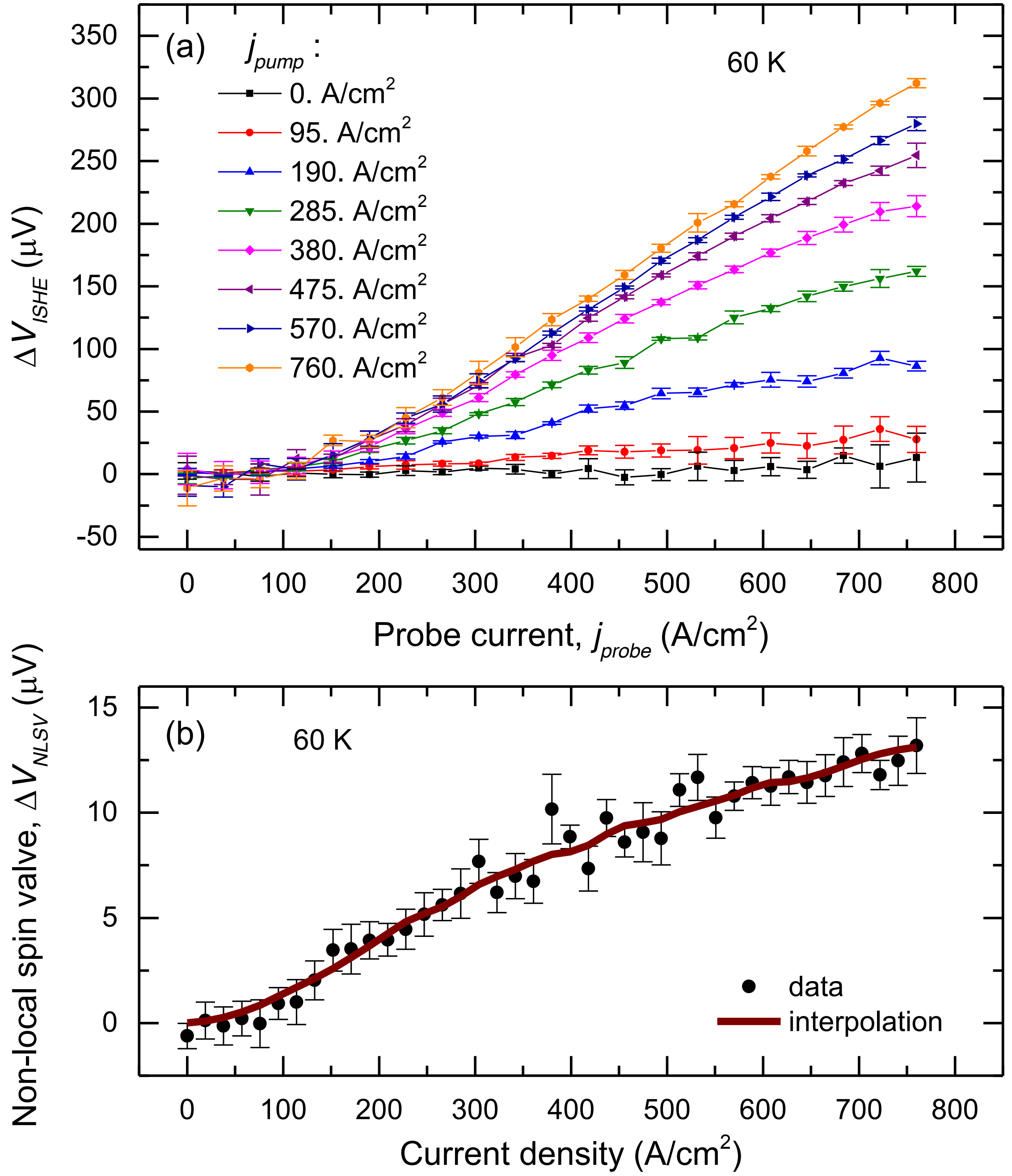

Figure 5.7: (a) Magnitude of ISHE signal as a function of current densities j_{probe} and j_{pump}. (b) Non-local spin valve vs. current density.

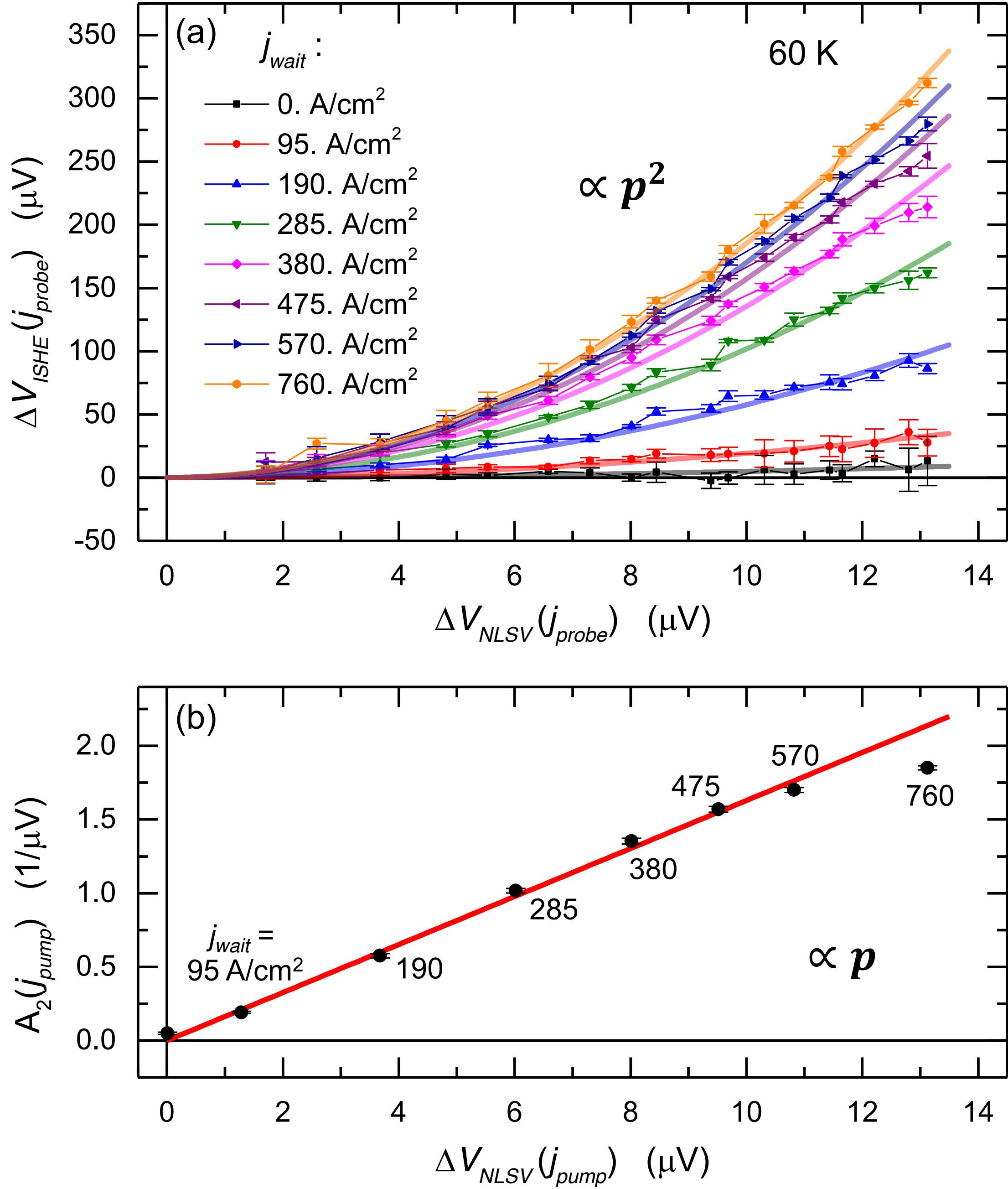

Figure 5.8: (a) Quadratic dependence of the ISHE magnitude on spin injection rate of the probe pulse. Solid lines are a fit to the quadratic form given in Eq. 5.9. (b) Linear dependence of the ISHE magnitude on spin injection rate of the pump bias.

quadratic dependence of the ISHE magnitude on the spin injection rate of the *probe* pulse. The solid lines represent fits to the quadratic expression

$$\Delta V_{ISHE}\left(j_{probe}\right) = A_2\left(j_{pump}\right)\left[\Delta V_{NLSV}\left(j_{probe}\right)\right]^2, \tag{5.9}$$

where $A_2\left(j_{pump}\right)$ denotes the constant of proportionality for each pump bias j_{pump}. The role of varying j_{probe} is soley to alter the magnitude of the spin injection rate independent of the nuclear polarization since $t_{probe} \ll T_H$. Note that while one power of the spin injection rate is implied by the presence of the spin current q in Eq. 5.1, the second power indicates that the spin accumulation is playing a direct role in enhancing the scattering asymmetry as discussed further below.

The dependence of the ISHE signal on the magnitude of the nuclear polarization may be seen by plotting each value of$A_2\left(j_{pump}\right)$ against the non-local spin valve signal evaluated at the same value of j_{pump}. The result of this process shown in Fig. 5.8(b) demonstrates a *linear* dependence of the ISHE magnitude on the spin injection rate of the *pump* current. Note that at high biases $j \gtrsim j_s = 580$ A/cm^2, drift effects cause a deviation from linear behavior due to the enhancement of the non-local signal (see Fig. 3.9). Since the nuclear polarization is expected to be linear with respect to the spin injection rate of the pump, this implies that scattering asymmetry is proportional to one power of the nuclear polarization.

To summarize, the observations in this section demonstrate that the ISHE signal depends *quadratically* on the spin injection rate of the probe pulse, and *linearly* on the spin injection rate of the pump bias. Attributing one power of the pump rate to the spin current, the enhancement in the ISHE must therefore be proportional to one power of the nuclear polarization and one power of the spin accumulation.

5.4 Hyperfine-enhanced spin-relaxation

To interpret the observations in the previous sections, we now outline a mechanism for the enhancement in the scattering asymmetry. Although a quantitative calculation of the scattering amplitudes is beyond the scope of this work, it is possible to motivate a phenomenological form for the effect which may be parameterized for comparison with theoretical estimates.

We start by noting that the nuclear field in our samples is highly inhomogeneous[30, 87, 88] as shown schematically in Fig. 5.9. This is a consequence of being doped close to the metal insulator transition where the condition for linear screening $k_F a_B \gg 1$ does not apply. This means that a significant fraction of the donor sites hybridize with the conduction band to form virtual bound states rather than being fully screened as in the Thomas-Fermi

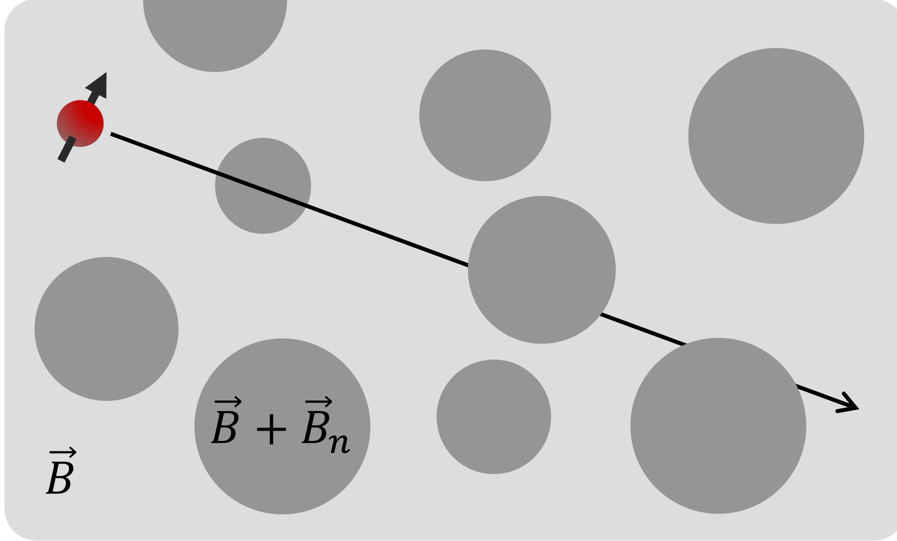

Figure 5.9: Cartoon showing an electron spin traversing inhomogeneities in the nuclear system.

approach. Since the hyperfine interaction is of the contact form (i.e. proportional to the square of the electronic wavefunction evaluated at the site of the nucleus), the peak in the local density of states near a donor site leads to an enhanced interaction between the electronic and nuclear states. Electrons traversing the sample experience a fluctuating hyperfine field which, critically, causes their orientation to differ from the rest of the electron spin ensemble. We contend that the resulting electron-electron exchange interaction gives rise to two experimental signatures: (1) an anisotropic source of spin relaxation and (2) an enhancement in the scattering asymmetry.

We first pause to consider the possible spin-dependent energy scales which may give rise to the enhanced scattering asymmetry. The 'normal' spin-Hall effect arises from the magnitude of the (renormalized) spin-orbit field $\frac{1}{2}g^{\star}\mu_B B_{SO,P} = \lambda_{SO}\vec{k}\times\vec{\nabla}V$ near an ionized impurity. Evaluating the magnitude at a distance of one Bohr radius yields

$$B_{SO,P} = \frac{2\lambda_{SO}k_F}{g^{\star}\mu_B}\frac{\varepsilon_B}{a_B} \approx 0.3 \text{ T} \tag{5.10}$$

This allows a crude estimate[89] for the ordinary spin Hall angle as $\gamma \sim g^{\star}\mu_B B_{SO}/2\varepsilon_F \sim 0.5\times 10^{-3}$, in agreement with the values mentioned previously. We note that an additional energy scale or resonant effect is required to obtain an enhancement in the scattering asymmetry. The strength of the Dresselhaus spin-orbit field is comparable to the estimate above.

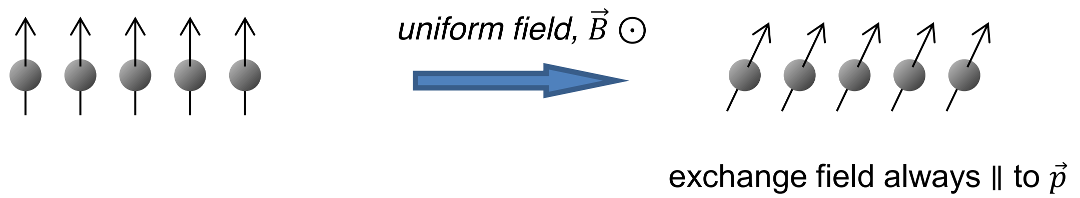

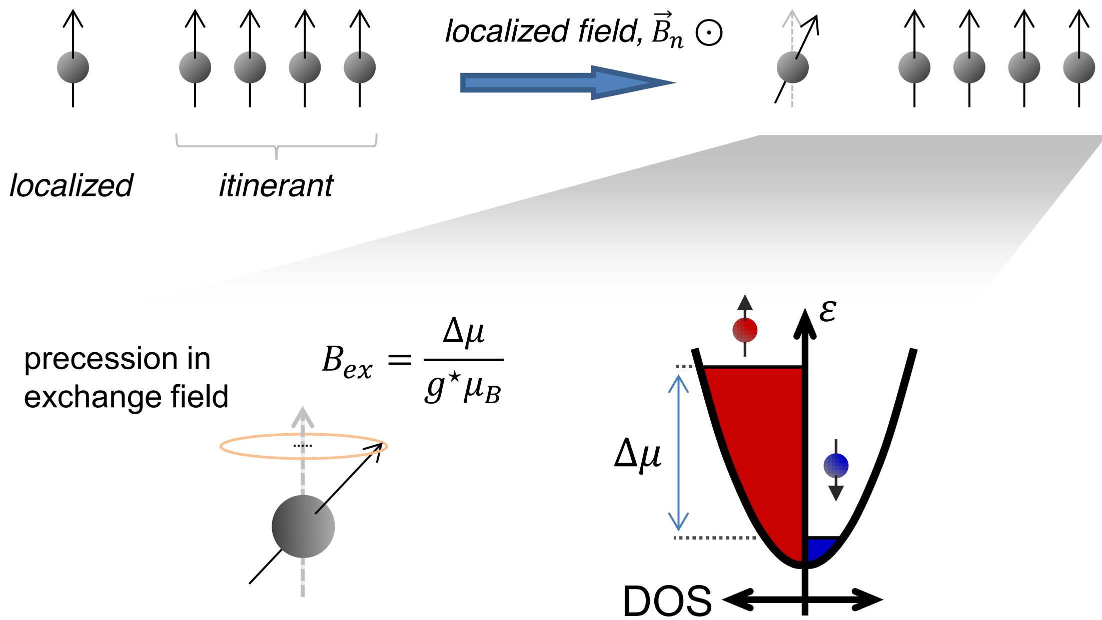

Figure 5.10: Diagram showing behavior of a spin polarized ensemble in (a) homogeneous and (b) inhomogeneous environments.

Using Eq. 3.74 with $n = 2n_c$, we obtain:

$$B_{SO,D} = \frac{\hbar}{g^\star \mu_B}\sqrt{\langle \Omega_D^2 \rangle} = \frac{2\beta}{g^\star \mu_B}\sqrt{\frac{4}{105}}3\pi^2 n \approx 0.4 \text{ T}. \tag{5.11}$$

In n-GaAs, the maximum possible hyperfine field is given by a straightforward calculation by Paget *et al.* [29] as

$$B_n^{max} \approx 5.7 \text{ T}. \tag{5.12}$$

In comparison with Eq. 5.10, these fields alone are not large enough to generate the increase in the observed scattering asymmetry. Adding them to the scattering calculation will not produce the desired enhancement.

If we consider, however, the chemical potential spin-splitting as an effective electronic exchange field, the magnitude may be quite large:

$$B_{ex} = \frac{\Delta\mu}{g^\star \mu_B} = \frac{2e}{g^\star \mu_B}\frac{D}{\nu}p. \tag{5.13}$$

For reasonable values of D/ν, this corresponds to 5 T for every percent of spin polarization. As shown in the previous chapter, we are routinely able to achieve polarizations in excess of 30%, which by this reasoning corresponds to an effective field of 150 T. However, this exchange field is not observed under typical conditions because it is always oriented parallel to the spin accumulation:

$$\left(\frac{\partial \vec{p}}{\partial t}\right)_{\text{precess}} = -\gamma\left(\vec{B} + \vec{B}_{ex}\right) \times \vec{p} \tag{5.14}$$

$$= -\gamma \vec{B} \times \vec{p} - \gamma\left(\frac{2e}{g^\star \mu_B}\frac{D}{\nu}\right)\vec{p} \times \vec{p} \tag{5.15}$$

$$= -\gamma \vec{B} \times \vec{p}. \tag{5.16}$$

This homogeneous precession is depicted in Fig. 5.10(a), where no significant variation is expected within the volume over which the polarization has been coarse grained. However, in the presence of an inhomogeneous nuclear field, this need no longer be the case as shown by the following crude derivation.

As shown in Fig. 5.10(b), we assume that at any given moment in time, a fraction f of the electrons are transiently localized in the vicinity of a donor site where the nuclear field is strongest[30, 87, 88]. After a residency time Δt_l, these local spins acquire a net phase $-\gamma\left|\vec{B}_n \times \hat{p}\right|\Delta t_l/f$ relative to the itinerant moments. Note that in this model, the Overhauser field only acts upon a fraction f of the electron spins at any given moment in time. Thus, to properly connect with the effective Overhauser field felt by the ensemble,

$\vec{B}_n$ needs to be normalized[30] here by the localized fraction f.

We now suppose that after Δt_l, these spins become itinerant again for a time Δt_i. Because their orientation is different than the rest of the ensemble, they must precess and dephase under the influence of the exchange field. Assuming the exchange field completely dephases any perpendicular component, the polarization will have been decreased by a factor of

$$1 - \cos\left[-\frac{\gamma \left|\vec{B}_n \times \hat{p}\right| \Delta t_l}{f}\right] \approx \frac{\gamma^2 \left|\vec{B}_n \times \hat{p}\right|^2 (\Delta t_l)^2}{2f^2} \tag{5.17}$$

Since this process happens every $\Delta t_l + \Delta t_i$, the relaxation rate is given by

$$\left(\frac{\partial p}{\partial t}\right)_{\text{relax, hyperfine}} = -\frac{\gamma^2 \left|\vec{B}_n \times \hat{p}\right|^2}{2f^2} \frac{(\Delta t_l)^2}{\Delta t_l + \Delta t_i} p \tag{5.18}$$

With $f \approx \Delta t_l / (\Delta t_l + \Delta t_i)$, we have

$$\left(\frac{\partial p}{\partial t}\right)_{\text{relax, hyperfine}} = -\frac{1}{2}\gamma^2 \left|\vec{B}_n \times \hat{p}\right|^2 \Delta t_{hf} p \tag{5.19}$$

where $\Delta t_{hf} \equiv \Delta t_l + \Delta t_i$. The role of the nuclear field then is to cause a fraction of the itinerant spins to be misaligned relative to their neighbors. This results in a source of spin relaxation analogous to the Bir-Aronov-Pikus mechanism which describes the dephasing of conduction electron spins due to their exchange interaction with unpolarized hole states. In our case, the electrons precessed by the inhomogeneous nuclear system are dephased by the exchange interaction with the other electron states in the ensemble.

5.4.1 Resonant skew scattering

We now outline how the combination of spin-orbit coupling, a polarized nuclear system, and a large effective exchange field may give rise to a spin-dependent contribution to the Hall signal. We propose an extrinsic mechanism is based on the enhancement of spin-flip scattering by the nuclear system, which in the presence of spin-orbit coupling generates a contribution to the Hall effect. For incident spin-up and spin-down electrons scattered by an angle ϑ, the scattering amplitudes may be written as[90, 89]

$$f_\uparrow(\vartheta) = f_1(\vartheta)\left|\uparrow\right\rangle + ie^{i\varphi} f_2(\vartheta)\left|\downarrow\right\rangle \tag{5.20}$$

$$f_\downarrow(\vartheta) = f_1(\vartheta)\left|\downarrow\right\rangle - ie^{-i\varphi} f_2(\vartheta)\left|\uparrow\right\rangle. \tag{5.21}$$

$f_1(\vartheta)$ and $f_2(\vartheta)$ are the non-spin-flip and spin-flip amplitudes respectively in the presence of spin-orbit coupling. φ denotes the azimuthal angle. The (spin-independent) intensity of the scattering is given by the function

$$I(\vartheta) = |f_1(\vartheta)|^2 + |f_2(\vartheta)|^2 \tag{5.22}$$

which is related to the momentum relaxation rate as

$$\tau_p^{-1} = n_i v_F \int d\Omega I(\vartheta)(1-\cos\vartheta), \tag{5.23}$$

where n_i is the density of scatterers and v_F is the Fermi velocity. Here $d\Omega$ denotes integration over the solid angle.

The asymmetry introduced by the spin-flip term in Eqs. 5.20 and 5.21 may be described as follows. An unpolarized source of electrons incident along $\vec{k}$ and scattered into $\vec{k}'$ will acquire a polarization oriented along the direction $\hat{k}\times\hat{k}'$. The magnitude of this polarization is given by the Sherman function

$$S(\vartheta) = \frac{2\mathrm{Im}\left[f_1^\star(\vartheta) f_2(\vartheta)\right]}{|f_1(\vartheta)|^2 + |f_2(\vartheta)|^2}, \tag{5.24}$$

which specifies the skewness of each scattering event. This may be used in the spin-dependent Boltzmann equation to solve for the spin-Hall angle as[79, 49, 89]

$$\gamma = \frac{\int d\Omega I(\vartheta) S(\vartheta)\sin\vartheta}{\int d\Omega I(\vartheta)(1-\cos\vartheta)}. \tag{5.25}$$

This may be re-written as

$$\gamma = n_i v_F \tau_p \int d\Omega 2\mathrm{Im}\left[f_1^\star(\vartheta) f_2(\vartheta)\right]. \tag{5.26}$$

Note that the spin-Hall angle is proportional to the spin-flip scattering amplitude $f_2(\vartheta)$. This reflects the fact that in the presence of spin-orbit coupling, the spin-index alone is not a good quantum number for labeling Bloch states. Processes which alter the spin degree of freedom must necessarily also induce a change in the crystal momentum $\hbar\vec{k}$. However, as noted at the beginning of the section, the spin-orbit coupling in the conduction band of GaAs alone is insufficient to generate the enhancement in scattering. For this we need to invoke the concept of resonant scattering.

In our samples the inverse Fermi wavelength k_F^{-1} is on the same order as the effective Bohr radius. This means that in contrast to the Thomas-Fermi approach, the screening of

impurities will occur in a non-linear fashion via the formation of virtual bound states with Friedel oscillations. The way in which an impurity is dissolved by the Fermi sea is intimately related to the particulars of its scattering cross section. While the potential at each impurity site is insufficient to establish a bound state, it produces a peak in the local density of states which retains most of the features of its "atomic legacy" (see the excellent discussion in [91]). This allows us to associate each impurity state of total angular momentum $J = L + S$ with a corresponding partial wave shift. Incident electrons preferentially hybridize with the virtual bound states most closely matched to their total angular momentum and energy. If the impurity is occupied such that only $L > 0$ states are available, electrons passing to the right of the impurity will be preferentially scattered, leading to a left-right asymmetry.

The functions $f_1(\vartheta)$ and $f_2(\vartheta)$ may be expressed in terms of partial wave shifts as[90, 89]

$$f_1(\vartheta) = \sum_l \frac{P_l(\cos\vartheta)}{2ik}\left[(l+1)\left(e^{2i\delta_l^+}-1\right) + l\left(e^{2i\delta_l^-}-1\right)\right] \tag{5.27}$$

$$f_2(\vartheta) = \sum_l \frac{\sin\vartheta}{2ik}\left(e^{2i\delta_l^+} - e^{2i\delta_l^-}\right)\frac{d}{d\cos\vartheta}P_l(\cos\vartheta), \tag{5.28}$$

where δ_l^+ and δ_l^- are the partial wave shifts for total angular momentum terms $l + \frac{1}{2}$ and $l - \frac{1}{2}$ respectively. Inserting these expressions in Eq. 5.25 yields

$$\gamma \approx n_i v_F \tau_p \left(\frac{16\pi}{3}\right)\sin\delta_0 \sin\left(\delta_1^+ + \delta_1^- - \delta_0\right)\sin\left(\delta_1^+ - \delta_1^-\right). \tag{5.29}$$

where we have carried out the expansion only to the lowest order term yielding a non-zero contribution ($l = 1$). The order of the expansion is not important for this discussion, but we note that for a quantitative calculation, expression 5.23 provides a way of testing the partial wave analysis against the total scattering cross-section implied by the experimental mobility as was performed in Ref. [79].

The partial wave shift for the (resonant) scattering of an incident electron of energy ε from a virtual bound state with energy $\varepsilon_l^\pm$ is given by[92, 30, 93, 94]

$$\cot\delta_l^\pm = \frac{\varepsilon - \varepsilon_l^\pm}{\Delta}. \tag{5.30}$$

Here Δ denotes the width of the resonant state and is likely on the order of the binding energy ε_B in our systems. To obtain expressions for $\varepsilon_l^\pm$, and thereby the partial wave shifts,

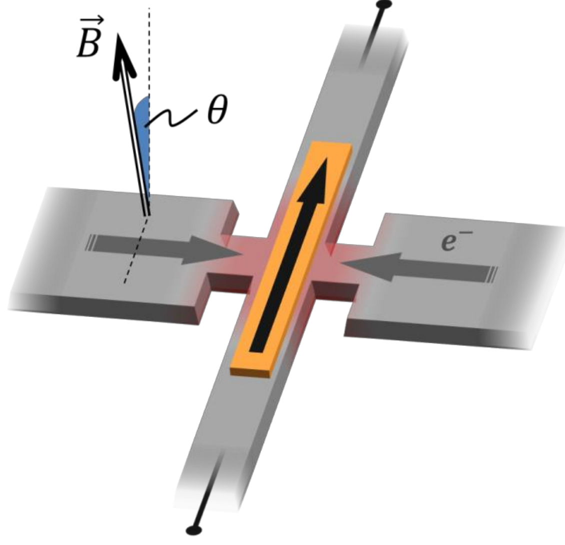

Figure 5.11: Diagram of oblique Hanle field direction

it is necessary to solve the following Hamiltonian perturbatively:

$$H = H_0 + \underbrace{\lambda \vec{L} \cdot \vec{s}}_{\text{spin-orbit}} + \underbrace{J\left(\vec{s} \cdot \vec{S}\right)}_{\text{exchange}} + \underbrace{\gamma \vec{B}_n \cdot \vec{s}}_{\text{hyperfine}}. \tag{5.31}$$

where H_0 yields hydrogenic states. Here $\vec{S}$ denotes the large exchange field imposed by the background spin accumulation. $\vec{s}$ is the polarization of the incident electron. A full analysis of this problem is complicated by the possibility of spin-flips of the nuclear system or within the exchange field during the scattering process. Several treatments of such a model may be found with the context of the anomalous Hall effect[95, 96, 92, 97, 89, 94, 98, 99], but usually either the itinerant or localized states are assumed to be unpolarized. We simply point out here that as in the hyperfine-induced relaxation mechanism, the role of the hyperfine term in Eq. 5.31 is to cause an inhomogeneity within the electron spin system. The exchange term may be written as

$$J\vec{s} \cdot \vec{S} = J_{\|} s_z S_z + J_{\perp}\left(s_+ S_- + s_- S_+\right). \tag{5.32}$$

The flip-flop term will only be 'activated' in the presence of the nuclear polarization.

5.5 Angle dependence

The hypothesis of the previous section implies a strong anisotropy of the relaxation rate with respect to the orientation of the Overhauser field $\vec{B}_n$. To test this, we performed a detailed angle dependence of the 3T and ISHE Hanle signals. As shown in Fig. 5.11, the orientation of the applied field was canted by an angle θ away from the vector normal to the plane of the device towards the ferromagnetic easy axis. As discussed in Sec. 4.4, this produces satellite peaks at field values where the Overhauser field partially cancels the applied field. Hanle sweeps were performed at 60 K for angles ranging from $-20°$ to $+20°$ in 5° increments for both magnetization states. Fig. 5.12 shows the angle dependence of the three-terminal signal in the gray open circles.

To model these data, we solve the following zero-dimensional model:

$$\frac{\partial \vec{p}}{\partial t} = -\frac{\vec{p}}{\tau_s} - \gamma \left(\vec{B} + \vec{B}_n \right) \times \vec{p} + \frac{\vec{\eta} j}{net}. \tag{5.33}$$

The first three terms specify the relaxation, precession, and injection behavior of the system respectively. Here t denotes the thickness of the device. We use the standard form for the Overhauser field given by[77, 50]

$$\vec{B}_n = b_n \left\langle \vec{I} \right\rangle = \frac{b_n \vec{p} \cdot \left(\vec{B} + b_e \vec{p} \right)}{\left| \vec{B} + b_e \vec{p} \right|^2 + \xi B_L^2} \left(\vec{B} + b_e \vec{p} \right) \tag{5.34}$$

where b_n denotes the Overhauser coefficient, b_e is the Knight field coefficient, and $\sqrt{\xi} B_L$ parameterizes the strength of the random local field. For the sake of this discussion, it is not necessary to understand the origin of this expression. However, it is important to note that the Overhauser field $\vec{B}_n$ is co-linear with and directly proportional to the magnitude of the nuclear polarization $\left\langle \vec{I} \right\rangle$. Because of the non-trivial dependence of the Overhauser field on polarization, Eq. 5.33 must be solved by iterating

$$\vec{p}^{new} = \vec{p} + \frac{\partial \vec{p}}{\partial t} \Delta t \tag{5.35}$$

until convergence is achieved at each value of the applied field. The results of this modeling procedure are shown by the red lines in Fig. 5.12(a). The following five parameters were adjusted until an optimum solution was obtained: b_n, b_e, $\sqrt{\xi} B_L$, τ_s, and a single scaling factor V_0 used to adjust the magnitude of all curves simultaneously. Although the spin lifetime is known from non-local Hanle measurements, the reduced dimensionality of this model artificially increases the spin relaxation rate as mentioned in Sec. 3.2.3. Although

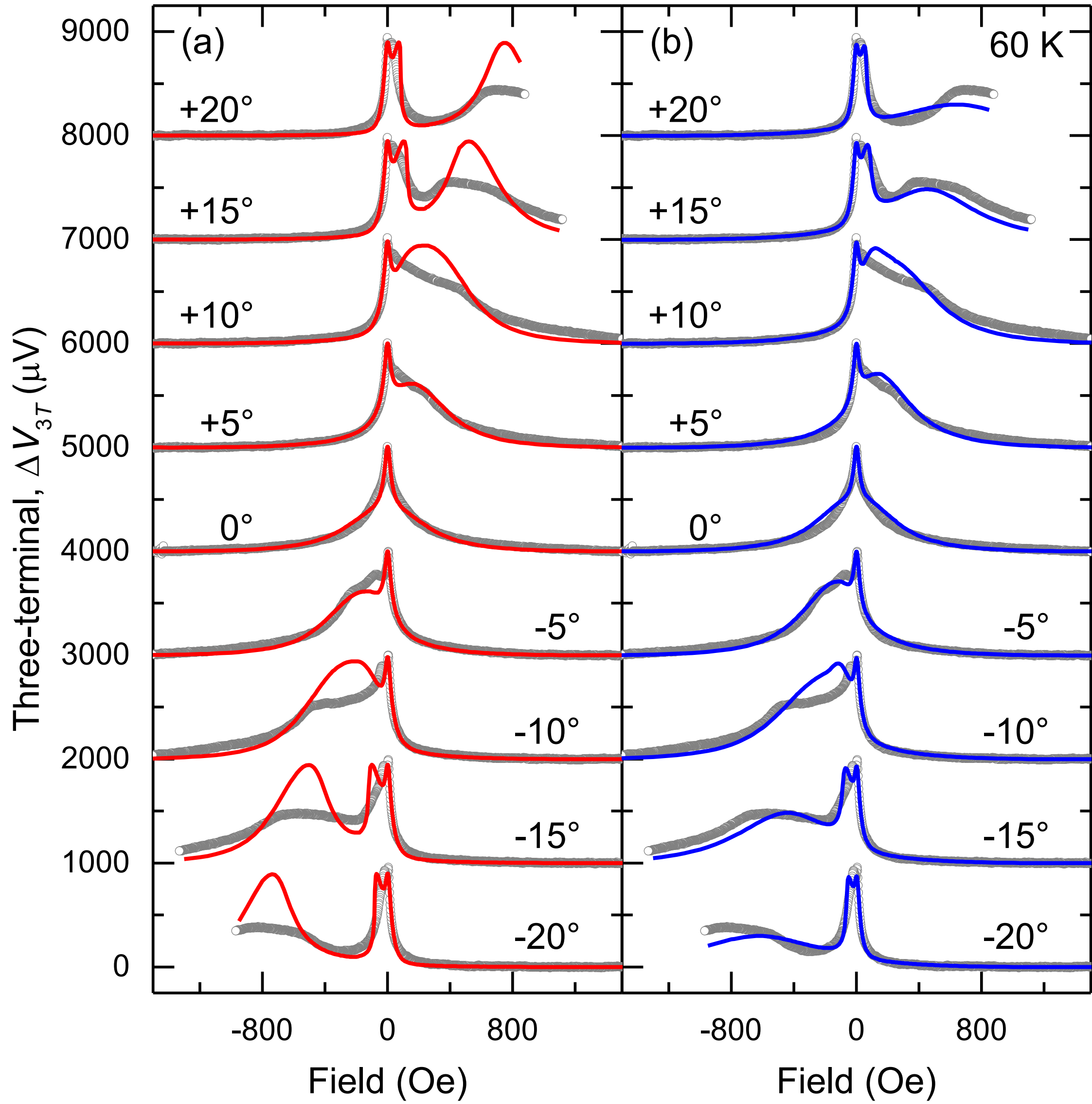

Figure 5.12: 3T signal as a function of angle (gray). Modeling shown (a) without and (b) with additional source of spin relaxation due to nuclear polarization.

Table 5.1: Optimized modeling parameters

Parameter	Isotropic relaxation	Anisotropic relaxation
isotropic spin lifetime, τ_s	1.49 ns	1.39 ns
Overhauser coefficient, b_n	−19700 Oe	−17400 Oe
Knight coefficient, b_e	−159 Oe	−127 Oe
local field, $\sqrt{\xi}B_L$	90.2 Oe	69.9 Oe
hyperfine relaxation, Δt_{hf}	N/A	389 ps

data for only one magnetization is shown in Fig. 5.12, these parameters were optimized using data from all eighteen field sweeps.

At higher angles, the isotropic relaxation model (5.33) overestimates the height of the satellite peaks. This is remedied by including the anisotropic contribution derived in the previous section. Fig. 5.12(b) shows the modeling results when Eq. 5.19 is included as

$$\frac{\partial \vec{p}}{\partial t} = -\frac{\vec{p}}{\tau_s} - \gamma\left(\vec{B} + \vec{B}_n\right) \times \vec{p} + \frac{\vec{\eta} j}{net} - \frac{1}{2}\gamma^2 \left|\vec{B}_n \times \hat{p}\right|^2 \Delta t_{hf}\vec{p}. \tag{5.36}$$

The optimized parameters used to generate curves in Fig. 5.12(a) and (b) are given in Table 5.1.

The angle dependence of the ISHE signal is shown as the gray curves in Fig. 5.13 which have been symmetrized to eliminate the contribution from the even component. We note that simultaneously reversing the sign of the magnetization $\vec{M}$ and the angle θ is equivalent to rotating the device by 180°, i.e. swapping the V_+ and V_- labels on the Hall terminals.

Using the values for the polarization $\vec{p}$ determined from Eq. 5.36, the line-shape of the ISHE signal may be modeled by assuming that the spin current giving rise to the Hall voltage is proportional to the polarization under the contact. This is an appropriate assumption when the contribution from drift effects is small. While more rigorous modeling techniques could be implemented, our aim here is to quickly identify which phenomenological form for the deflection is consistent with the experimental observations discussed in the previous sections. In particular, any form for the deflection must satisfy the following requirements. The ISHE signal must (1) reverse sign with magnetization, (2) be proportional to one power of the nuclear polarization and two powers of the electron polarization, (3) maintain a roughly constant magnitude as a function of angle, and (4) yield the symmetries observed in both the parallel and perpendicular devices.

For the sake of comparison, we first note that Eq. 5.1 predicts the following form for the deflection:

$$\vec{j}^H \propto \hat{z} \times \vec{p}, \tag{5.37}$$

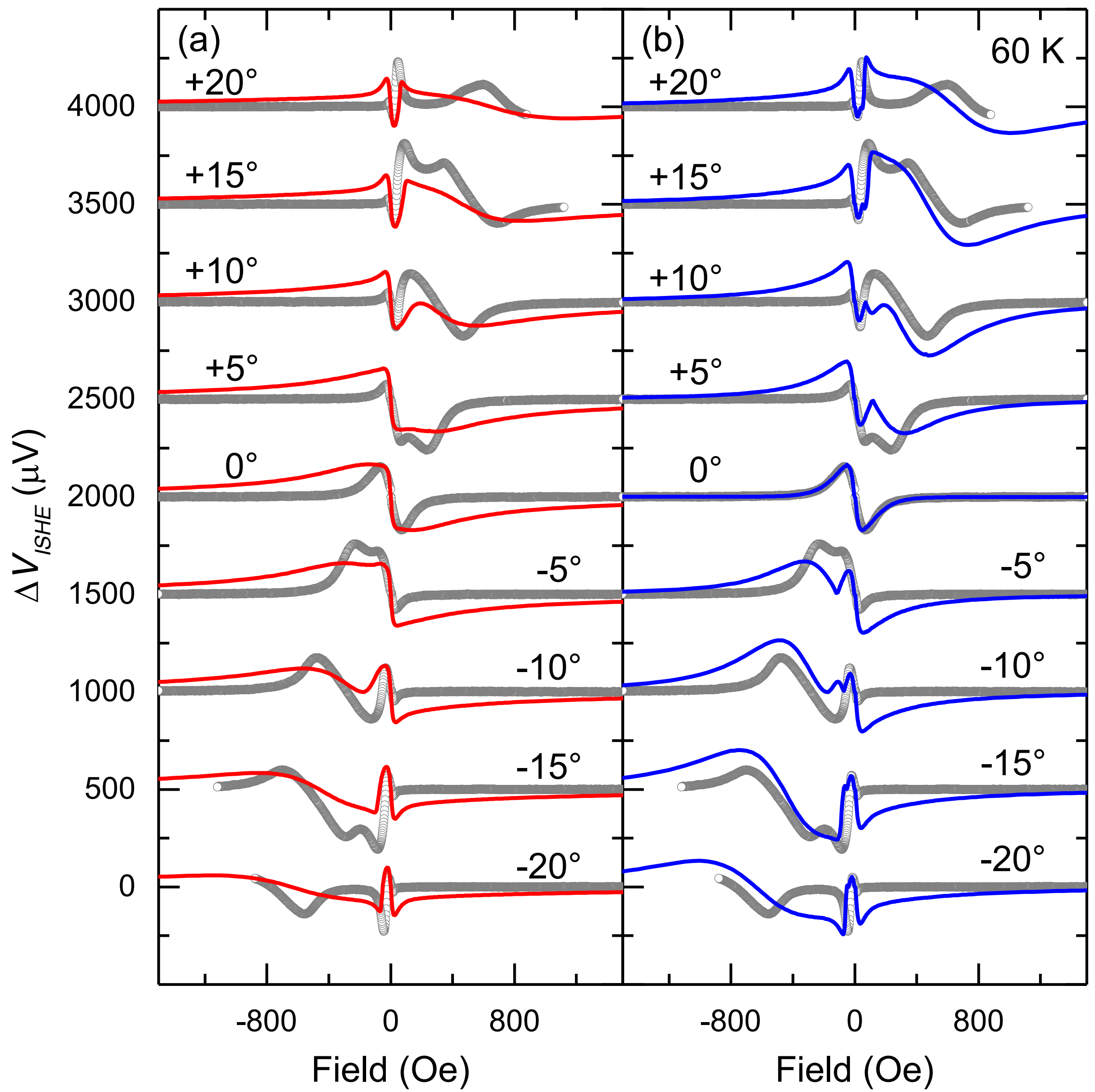

Figure 5.13: Experimental ISHE signal for several oblique angles shown in gray. (a) Modeling using the normal ISHE prediction of Eq. 5.1. (b) Modeling using the anisotropic expression in 5.38.

where $\hat{z}$ denotes the direction normal to the plane of the device. This form produces the red modeling curves shown in Fig. 5.13(a). However, as already noted at the beginning of this chapter, this does not fulfill several of the criteria listed above. In particular, conditions (2) and (3) highly constrain the possible forms for the deflection since the numerator of Eq. 5.34 grows significantly as the angle becomes more oblique.

The simplest form which *does* fulfill these requirements may be motivated by considering the mechanism presented in Sec. 5.4. Our hypothesis is that a fraction of the spins traversing the sample are precessed locally by an inhomogeneous nuclear field. The resulting interaction with the exchange field established by the other electrons causes a transverse deflection. With this in mind, the form should be proportional to (a) the ability of the nuclear system to precess the electron spins (i.e. $\left|\vec{B}_n \times \hat{p}\right|$) and (b) the magnitude of the exchange field $\propto |\vec{p}|$. This reasoning leads us to write

$$\vec{j}^H \propto \left|\vec{B}_n \times \vec{p}\right| (\hat{z} \times \vec{p}) \,. \tag{5.38}$$

The modeling results corresponding to this expression are shown by the blue curves in Fig. 5.13(b). The results in Fig. 5.14 confirm that the expression in Eq. 5.38 also reproduces the symmetries of the perpendicular device.

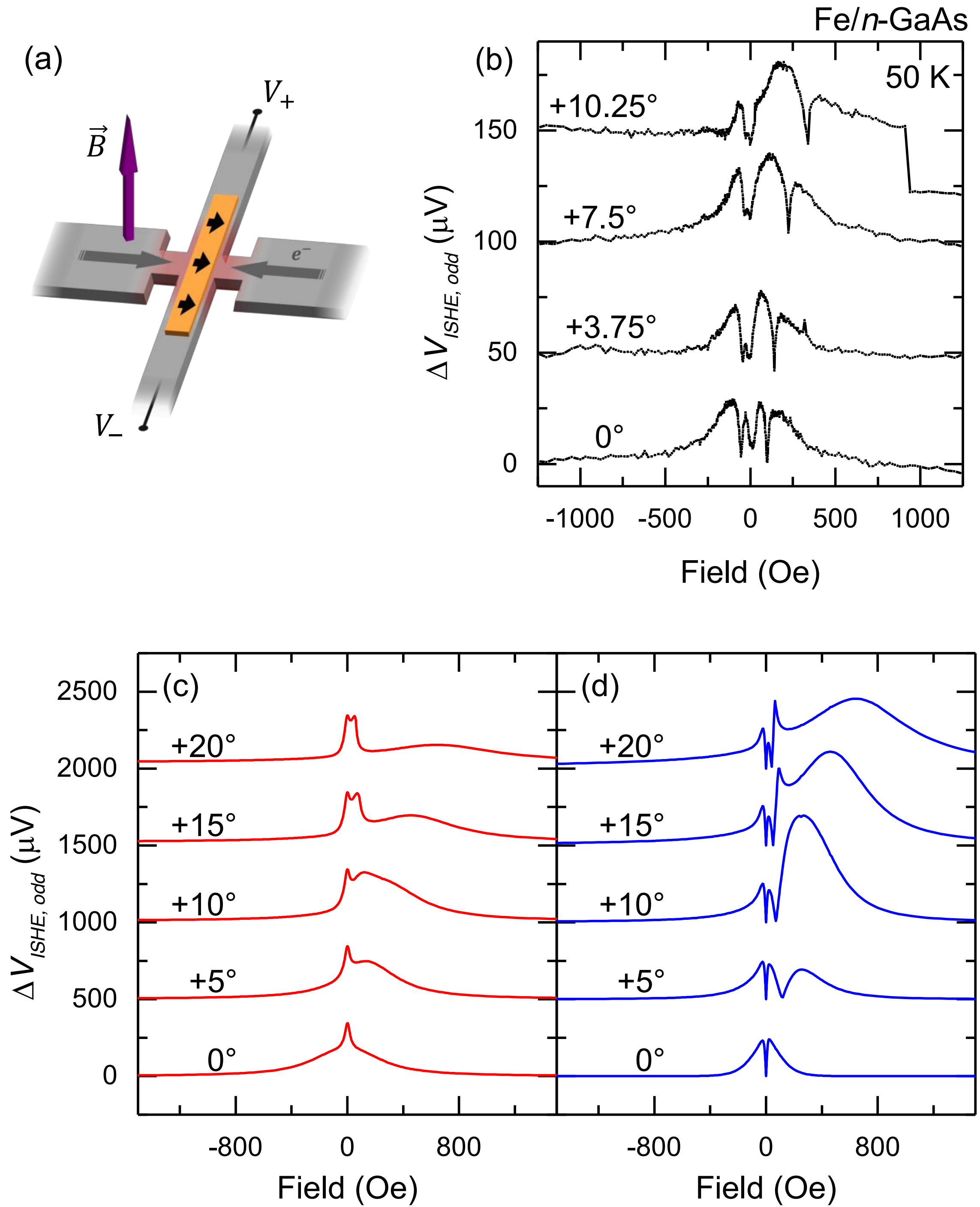

Figure 5.14: (a) Wiring diagram for perpendicular device. (b) Experimental angle dependence obtained on Fe/n-GaAs device. (c) Modeling using the normal ISHE prediction of Eq. 5.1. (d) Modeling using the anisotropic expression in 5.38.

Chapter 6

Conclusions

This dissertation provides a quantitative approach to the interpretation of several spin-dependent transport phenomena in semiconductors. A special emphasis is placed on experimental signatures which develop when the system is polarized far from equilibrium, i.e. when the chemical potential splitting $\Delta\mu = \mu_\uparrow - \mu_\downarrow$ becomes comparable to other energy scales in the problem.

One of the outstanding problems in semiconductor-based spintronics is the lack of a robust method for characterizing device performance across material systems. While this is important for providing incremental progress towards technological applications, we emphasize that a quantitative understanding is also a prerequisite for the interpretation of new physical phenomena. Unlike the case of charge transport measurements, the interpretation of spin-based measurements typically must account for a greater degree of spatial inhomogeneity. Furthermore, the behavior of most spin generation and detection techniques is not passive and may vary considerably as a function of the experimental parameters (temperature, bias, doping, material composition, etc.).

In this work we provided several experimental demonstrations to help address these problems. Chapter 3 presented a full phenomenology to account for variations in the transport parameters at large polarizations. The concept of spin resistances was introduced and applied to several important geometries. For the one-dimensional case, it was demonstrated that, regardless of the underlying mechanism or polarization of the ferromagnet, the spin injection rate must saturate in the regime of large bias.

A model for the non-local device geometry was used to fit Hanle precession curves. This allowed the extraction of independent information about both the spin diffusivity and spin lifetime across a wide range of temperatures and dopings. For the samples examined, it was found that the spin and charge diffusion constants are the same, thus validating our earlier

assumption that the influence of the impurity band on calculations involving the density of states may be neglected. We further demonstrated that the spin lifetime values exhibited excellent agreement with theoretical predictions at high temperatures. A deviation from expectations was observed at low temperatures in multiple samples.

Chapter 4 introduced experimental observations of the spin-generated electromotive force. This is a new spin-to-charge conversion appearing whenever a significant difference exists in diffusion rates for majority and minority carriers. As succinctly expressed by the Einstein relation, this effect then may be decomposed into positive contributions arising from the energy dependence of the carrier densities and mobilities, and a negative contribution from the density of states.

To observe this effect, we added a pair of shorted Hall arms to serve as a non-magnetic probe of the electrochemical potential in the vicinity of a ferromagnetic injector contact. A large Hanle precession signal was observed in the presence of applied and hyperfine fields. By comparing the observed magnitude with traditional ferromagnetic detection techniques, we demonstrated that the spin-generated EMF signal scales quadratically with the polarization.

Using the quantitative framework developed in the previous chapters, the various contributions to this effect may be evaluated with a high degree of accuracy. We employed straightforward electrostatic relaxation techniques to obtain a directly relation between the observed experimental shift and the spin polarization under the injector. Since this effect depends only on material parameters of the bulk semiconductor, the extract polarization values are notably independent of any assumptions regarding the efficiency of the spin injection process.

In Chap. 5, we examined spin-dependent contributions to signals measured in the Hall geometry. A large scattering asymmetry was observed which greatly exceeds existing predictions based on ionized impurity scattering. Using a pulsed measurement technique, it was shown this may be attributed to the presence of nuclear polarization. Based on the experimental observations, we proposed a mechanism for the enhancement based on inhomogeneities in the nuclear field which cause an additional source of spin relaxation in the exchange field imposed by chemical potential splitting. This was used to motivate phenomenological forms for both an anisotropic source of spin relaxation as well as a contribution to the Hall signal. Using the modeling techniques developed in the previous chapters, we verified that these forms are consistent with the observed angle dependence of both the three-terminal and Hall signals.

References

[1] I. R. Committee, *International Technology Roadmap for Semiconductors, 2011 Edition* (Semiconductor Industry Association, 2011).

[2] I. Žutić, J. Fabian, and S. Das Sarma, Rev. Mod. Phys. **76**, 323 (2004).

[3] M. N. Baibich, J. M. Broto, A. Fert, F. N. Van Dau, and F. Petroff, Phys. Rev. Lett. (1988).

[4] G. Binasch, P. Grünberg, F. Saurenbach, and W. Zinn, Phys. Rev. B **39**, 4828 (1989).

[5] S. Datta and B. Das, Appl. Phys. Lett. **56**, 665 (1990).

[6] G. E. W. Bauer, E. Saitoh, and B. J. van Wees, Nat Mater **11**, 391 (2012).

[7] A. Manchon, Nature Phys. **10**, 340 (2014).

[8] K. F. Mak, K. He, J. Shan, and T. F. Heinz, Nature nanotechnology **7**, 494 (2012).

[9] K. Roy, S. Bandyopadhyay, and J. Atulasimha, Appl. Phys. Lett. **99**, 063108 (2011).

[10] X. Lou, C. Adelmann, S. A. Crooker, E. S. Garlid, J. Zhang, K. S. M. Reddy, S. D. Flexner, C. J. Palmstrøm, and P. A. Crowell, Nature Phys. **3**, 197 (2007).

[11] M. Ciorga, A. Einwanger, U. Wurstbauer, D. Schuh, W. Wegscheider, and D. Weiss, Phys. Rev. B **79**, 165321 (2009).

[12] G. Salis, S. F. Alvarado, and A. Fuhrer, Phys. Rev. B **84**, 041307 (2011).

[13] T. Uemura, T. Akiho, M. Harada, K.-i. Matsuda, and M. Yamamoto, Appl. Phys. Lett. **99**, 082108 (2011).

[14] O. M. J. van 't Erve, A. T. Hanbicki, M. Holub, C. H. Li, C. Awo-Affouda, P. E. Thompson, and B. T. Jonker, Appl. Phys. Lett. **91**, 212109 (2007).

[15] I. Appelbaum, B. Huang, and D. J. Monsma, Nature **447**, 295 (2007).

[16] S. P. Dash, S. Sharma, R. S. Patel, M. P. de Jong, and R. Jansen, Nature **462**, 491 (2009).

[17] T. Suzuki, T. Sasaki, T. Oikawa, M. Shiraishi, Y. Suzuki, and K. Noguchi, Appl. Phys. Express **4**, 023003 (2011).

[18] R. Jansen, S. P. Dash, S. Sharma, and B. C. Min, Semicond. Sci. Technol. **27**, 083001 (2012).

[19] N. Tombros, C. Jozsa, M. Popinciuc, H. T. Jonkman, and B. J. van Wees, Nature **448**, 571 (2007).

[20] Y. Zhou, W. Han, L.-T. Chang, F. Xiu, M. Wang, M. Oehme, I. A. Fischer, J. Schulze, R. K. Kawakami, and K. L. Wang, Phys. Rev. B **84**, 125323 (2011).

[21] T. Saito, N. Tezuka, M. Matsuura, and S. Sugimoto, Appl. Phys. Lett. **103**, 122401 (2013).

[22] Y. Manzke, R. Farshchi, P. Bruski, J. Herfort, and M. Ramsteiner, Phys. Rev. B **87**, 134415 (2013).

[23] T. Akiho, J. Shan, H.-x. Liu, K.-i. Matsuda, M. Yamamoto, and T. Uemura, Phys. Rev. B **87**, 235205 (2013).

[24] W. Han, X. Jiang, A. Kajdos, S.-H. Yang, S. Stemmer, and S. S. P. Parkin, Nature Communications **4**, 1 (2013).

[25] R. Winkler, in *Spin-orbit Coupling Effects in Two-Dimensional Electron and Hole Systems* (Springer, 2003).

[26] D. Romero, S. Liu, H. D. Drew, and K. Ploog, Phys. Rev. B **42**, 3179 (1990).

[27] S. Liu, H. D. Drew, A. Illiades, and S. Hadjipanteli, Phys. Rev. B **45**, 1155 (1992).

[28] S. Liu, K. Karrai, F. Dunmore, H. D. Drew, R. Wilson, and G. A. Thomas, Phys. Rev. B **48**, 11394 (1993).

[29] D. Paget, G. Lampel, B. Sapoval, and V. I. Safarov, Phys. Rev. B **15**, 5780 (1977).

[30] D. Paget, Phys. Rev. B **24**, 3776 (1981).

[31] R. A. Smith, *Semiconductors*, 2nd ed. (Cambridge University Press, New York, 1978).

[32] M. E. Flatté and J. M. Byers, Phys. Rev. Lett. **84**, 4220 (2000).

[33] J. H. Quast, T. Henn, T. Kiessling, W. Ossau, L. W. Molenkamp, D. Reuter, and A. D. Wieck, Phys. Rev. B **87**, 205203 (2013).

[34] D. Belitz and T. R. Kirkpatrick, Rev. Mod. Phys. **66**, 261 (1994).

[35] J. S. Blakemore, *Semiconductor Statistics* (Courier Dover Publications, 2002).

[36] M. Römer, H. Bernien, G. Müller, D. Schuh, J. Hübner, and M. Oestreich, Phys. Rev. B **81**, 075216 (2010).

[37] E. O. Kane, Physical Review **131**, 10 (1963).

[38] B. I. Shklovskii and A. L. Efros, *Electronic Properties of Doped Semiconductors* (Springer-Verlag, Berlin Heidelberg, 1984).

[39] P. V. Mieghem, Rev. Mod. Phys. **64**, 755 (1992).

[40] C. Jacoboni, *Theory of Electron Transport in Semiconductors*, A Pathway from Elementary Physics to Nonequilibrium Green Functions, Vol. 165 (Springer, Berlin, Heidelberg, 2010).

[41] D. L. Rode and S. Knight, Phys. Rev. B **3**, 2534 (1971).

[42] M. Benzaquen, D. Walsh, and K. Mazuruk, Phys. Rev. B **34**, 8947 (1986).

[43] D. L. Rode, *Semiconductors and Semimetals, v. 10*, edited by R. K. Willardson and A. C. Beer (Academic Press, New York).

[44] Z. G. Yu and M. E. Flatté, Phys. Rev. B **66**, 235302 (2002).

[45] I. D'Amico and G. Vignale, Phys. Rev. B **65**, 085109 (2002).

[46] A. G. Petukhov, J. Niggemann, V. N. Smelyanskiy, and V. V. Osipov, J. Phys.: Condens. Matter **19**, 315205 (2007).

[47] F. Cadiz, D. Paget, and A. C. H. Rowe, Phys. Rev. Lett. **111**, 246601 (2013).

[48] I. D'Amico and G. Vignale, EPL **55**, 566 (2001).

[49] M. I. Dyakonov and A. V. Khaetskii, in *Spin Physics in Semiconductors*, edited by M. I. Dyakonov (Springer, 2008) pp. 211–243.

[50] M. K. Chan, *Hyperfine Effects in Ferromagnet-Semiconductor Heterostructures*, Ph.D. thesis, University of Minnesota.

[51] F. Meier and B. P. Zakharchenya, *Optical Orientation* (Elsevier, 1984).

[52] R. Dzhioev, K. Kavokin, V. Korenev, M. Lazarev, B. Meltser, M. Stepanova, B. Zakharchenya, D. Gammon, and D. Katzer, Phys. Rev. B **66**, 245204 (2002).

[53] J. M. Kikkawa and D. D. Awschalom, Phys. Rev. Lett. **80**, 4313 (1998).

[54] W. Lau, J. Olesberg, and M. E. Flatté, Phys. Rev. B **64**, 161301 (2001).

[55] E. I. Rashba, Phys. Rev. B **62**, R16267 (2000).

[56] D. L. Smith and R. Silver, Phys. Rev. B **64**, 045323 (2001).

[57] V. Osipov and A. Bratkovsky, Phys. Rev. B **72**, 115322 (2005).

[58] H. Dery and L. J. Sham, Phys. Rev. Lett. **98**, 046602 (2007).

[59] Y. Song and H. Dery, Phys. Rev. B **81**, 045321 (2010).

[60] D. L. Smith and A. N. Chantis, Phys. Rev. B **78**, 235317 (2008).

[61] S. A. Crooker, E. S. Garlid, A. N. Chantis, D. L. Smith, K. S. M. Reddy, Q. O. Hu, T. Kondo, C. J. Palmstrøm, and P. A. Crowell, Phys. Rev. B **80**, 041305 (2009).

[62] P. C. Hammel, Y. Pu, J. Beardsley, P. M. Odenthal, A. G. Swartz, R. K. Kawakami, E. Johnston-Halperin, J. Sinova, and J. P. Pelz, Appl. Phys. Lett. **103**, 012402 (2013).

[63] J. Shiogai, M. Ciorga, M. Utz, D. Schuh, M. Kohda, D. Bougeard, T. Nojima, J. Nitta, and D. Weiss, Phys. Rev. B **89** (2014).

[64] R. Jansen, S. P. Dash, S. Sharma, J. C. Le Breton, J. Peiro, H. Jaffrès, J. M. George, and A. Lemaître, Phys. Rev. B **84**, 054410 (2011).

[65] S. M. Sze and K. K. Ng, *Physics of Semiconductor Devices* (John Wiley & Sons, 2006).

[66] A. T. Hanbicki, B. T. Jonker, G. Itskos, G. Kioseoglou, and A. Petrou, Appl. Phys. Lett. **80**, 1240 (2002).

[67] A. T. Hanbicki, O. M. J. van 't Erve, R. Magno, G. Kioseoglou, C. H. Li, B. T. Jonker, G. Itskos, R. Mallory, M. Yasar, and A. Petrou, Appl. Phys. Lett. **82**, 4092 (2003).

[68] Q. O. Hu, E. S. Garlid, P. A. Crowell, and C. J. Palmstrøm, Phys. Rev. B **84**, 085306 (2011).

[69] Q. O. Hu, *Electrical Spin Injection and Detection in Ferromagnet-Semiconductor Heterostructures.*, Ph.D. thesis, Proquest, Umi Dissertation Publishing (2012).

[70] G. Homm, P. J. Klar, J. Teubert, and W. Heimbrodt, Appl. Phys. Lett. **93**, 042107 (2008).

[71] I. J. Vera-Marun, V. Ranjan, and B. J. van Wees, Phys. Rev. B **84**, 241408 (2011).

[72] I. J. Vera-Marun, V. Ranjan, and B. J. van Wees, Nature Phys. **8**, 313 (2012).

[73] I. J. Vera-Marun, B. J. van Wees, and R. Jansen, Phys. Rev. Lett. **112**, 056602 (2014).

[74] N. W. Ashcroft and N. D. Mermin, *Solid State Physics* (Holt, Rinehart and Winston, New York, 1976).

[75] V. A. Johnson and K. Lark-Horovitz, Physical Review **92**, 226 (1953).

[76] D. Kölbl, D. M. Zumbühl, A. Fuhrer, G. Salis, and S. F. Alvarado, Phys. Rev. Lett. (2012).

[77] M. K. Chan, Q. O. Hu, J. Zhang, T. Kondo, C. J. Palmstrøm, and P. A. Crowell, Phys. Rev. B **80**, 161206 (2009).

[78] X. Lou, C. Adelmann, M. Furis, S. A. Crooker, C. J. Palmstrøm, and P. A. Crowell, Phys. Rev. Lett. **96**, 176603 (2006).

[79] H.-A. Engel, B. Halperin, and E. Rashba, Phys. Rev. Lett. **95**, 166605 (2005).

[80] W.-K. Tse and S. Das Sarma, Phys. Rev. Lett. **96**, 056601 (2006).

[81] Y. K. Kato, R. C. Myers, A. C. Gossard, and D. D. Awschalom, Science (2004).

[82] E. S. Garlid, Q. O. Hu, M. K. Chan, C. J. Palmstrøm, and P. A. Crowell, Phys. Rev. Lett. **105**, 156602 (2010).

[83] K. Olejník, J. Wunderlich, A. C. Irvine, R. P. Campion, V. P. Amin, J. Sinova, and T. Jungwirth, Phys. Rev. Lett. **109**, 076601 (2012).

[84] M. Ehlert, C. Song, M. Ciorga, M. Utz, D. Schuh, D. Bougeard, and D. Weiss, Phys. Rev. B **86**, 205204 (2012).

[85] F. Bottegoni, A. Ferrari, G. Isella, M. Finazzi, and F. Ciccacci, Phys. Rev. B **88**, 121201 (2013).

[86] J. M. Flesselles and R. Botet, Journal of Physics a-Mathematical and General **22**, 903 (1989).

[87] D. Paget, Phys. Rev. B **25**, 4444 (1982).

[88] K. Christie, C. Geppert, S. Patel, Q. O. Hu, C. Palmstrøm, and P. Crowell, (2014), 1406.0436 .

[89] G.-Y. Guo, S. Maekawa, and N. Nagaosa, Phys. Rev. Lett. **102**, 036401 (2009).

[90] H. A. B. Jackiw and Roman, *Intermediate Quantum Mechanics (3rd Ed.)* (Menlo Park, CA).

[91] C. M. Hurd, Contemp. Phys. **16**, 517 (1975).

[92] A. Fert and O. Jaoul, Phys. Rev. Lett. **28**, 303 (1972).

[93] R. Shankar, *Principles of Quantum Mechanics* (Springer US, Boston, MA, 1994).

[94] N. Nagaosa, J. Sinova, S. Onoda, A. H. MacDonald, and N. P. Ong, Rev. Mod. Phys. **82**, 1539 (2010).

[95] J. Kondo, Prog. Theor. Phys. **27**, 772 (1962).

[96] J. Kondo, Prog. Theor. Phys. **28**, 846 (1962).

[97] P. M. Levy and A. Fert, Phys. Rev. B **39**, 12224 (1989).

[98] A. Fert and P. M. Levy, Phys. Rev. Lett. **106**, 157208 (2011).

[99] C. Herschbach, D. V. Fedorov, I. Mertig, and M. Gradhand, Phys. Rev. B (2013).

Appendix A

Derivations

A.1 Compressibility and higher derivatives

The number density n is determined by integrating over the density of states $g(\varepsilon)$ as a function of the chemical potential μ:

$$n = \int_{-\infty}^{+\infty} g(\varepsilon) f(\varepsilon - \mu) \, d\varepsilon. \tag{A.1}$$

Here $f(\varepsilon - \mu) = [\exp(\varepsilon - \mu) + 1]^{-1}$ is the Fermi-Dirac function. Taking a derivative with respect to μ yields the electronic compressibility:

$$\frac{\partial n}{\partial \mu} = \frac{\partial}{\partial \mu} \int_{-\infty}^{+\infty} g(\varepsilon) f(\varepsilon - \mu) \, d\varepsilon = -\int_{-\infty}^{+\infty} g(\varepsilon) f'(\varepsilon - \mu) \, d\varepsilon, \tag{A.2}$$

where we have used the fact that $\partial f / \partial \mu = -\partial f / \partial \varepsilon$. Integrating by parts yields:

$$\frac{\partial n}{\partial \mu} = -\int_{-\infty}^{+\infty} \left\{ \frac{\partial}{\partial \varepsilon} [g(\varepsilon) f(\varepsilon - \mu)] - g''(\varepsilon) f(\varepsilon - \mu) \right\} d\varepsilon. \tag{A.3}$$

The first term will be zero provided that the behavior of $\lim_{\varepsilon \to +\infty} g(\varepsilon)$ is less than exponential and that $\lim_{\varepsilon \to -\infty} g(\varepsilon) = 0$. This procedure can be generalized to higher order derivatives to yield the result

$$\frac{\partial^\alpha n}{\partial \mu^\alpha} = \int_{-\infty}^{+\infty} \frac{\partial^\alpha g}{\partial \varepsilon^\alpha} \frac{d\varepsilon}{e^{(\varepsilon - \mu)/k_B T} + 1}. \tag{A.4}$$

A.2 Derivation of spin-dependent current densities

The following derivation tracks Ref. [74] closely. We assume that the non-equilibrium distribution function for each spin species is given by

$$f_\sigma\left(\vec{k}\right) = f_0\left(\varepsilon\left(\vec{k}\right)\right) + \tau\left(\varepsilon\left(\vec{k}\right)\right)\vec{\nabla}\zeta_\sigma \cdot \left[\vec{v}\left(\vec{k}\right)\frac{\partial f_0}{\partial \varepsilon}\right] \tag{A.5}$$

$$= f_0\left(\varepsilon\left(\vec{k}\right)\right) + \frac{1}{\hbar}\tau\left(\varepsilon\left(\vec{k}\right)\right)\vec{\nabla}\zeta_\sigma \cdot \frac{\partial}{\partial \vec{k}} f\left(\varepsilon\left(\vec{k}\right)\right) \tag{A.6}$$

The current density in each spin channel is given by

$$\vec{j}_\sigma = -e\int \frac{d\vec{k}}{(2\pi)^3}\tau\left(\varepsilon\left(\vec{k}\right)\right)\vec{v}\left(\vec{k}\right) f_\sigma\left(\vec{k}\right) \tag{A.7}$$

$$= -\frac{e}{\hbar}\int \frac{d\vec{k}}{(2\pi)^3}\tau\left(\varepsilon\left(\vec{k}\right)\right)\vec{v}\left(\vec{k}\right)\left[\vec{\nabla}\zeta_\sigma \cdot \frac{\partial}{\partial \vec{k}} f_0\left(\varepsilon\left(\vec{k}\right)\right)\right] \tag{A.8}$$

Moving to tensor notation and assuming an energy independent momentum relaxation time

$$j_{\sigma,\mu} = -\frac{e}{\hbar}\frac{\partial \zeta_\sigma}{\partial x_\nu}\tau\int \frac{d\vec{k}}{(2\pi)^3} v_\mu\left(\vec{k}\right)\frac{\partial}{\partial k_\nu} f_0\left(\varepsilon\left(\vec{k}\right)\right) \tag{A.9}$$

Integrating by parts (see Ref. [74], Appendix I):

$$j_{\sigma,\mu} = e\tau\frac{\partial \zeta_\sigma}{\partial x_\nu}\int \frac{d\vec{k}}{(2\pi)^3}\frac{1}{\hbar^2}\frac{\partial^2 \varepsilon}{\partial k_\mu \partial k_\nu} f_0\left(\varepsilon\left(\vec{k}\right)\right) \tag{A.10}$$

Assuming an isotropic effective mass

$$\frac{1}{\hbar^2}\frac{\partial^2 \varepsilon}{\partial k_\mu k_\nu} = \frac{\delta_{\mu\nu}}{m^\star} \tag{A.11}$$

yields

$$j_{\sigma,\mu} = \frac{e\tau}{m^\star}\frac{\partial \zeta_\sigma}{\partial x_\mu}\int \frac{d\vec{k}}{(2\pi)^3} f_0\left(\varepsilon\left(\vec{k}\right)\right) \tag{A.12}$$

Or simply

$$\vec{j}_\sigma = n_\sigma \nu \vec{\nabla}\zeta_\sigma \tag{A.13}$$

A.3 Energy dependence of mobility and diffusion constant

The parameter Ξ was introduced in Sec. 3.1.2. The derivation is as follows:

$$\begin{aligned}
\Xi &= \frac{\nu_\uparrow - \nu_\downarrow}{\nu_\uparrow + \nu_\downarrow}\frac{1}{p} \approx \frac{\partial\nu/\partial n}{\nu/n} && \text{(A.14)}\\
&= \frac{n}{\nu}\frac{\partial\nu}{\partial\mu}\frac{\partial\mu}{\partial n} = \frac{1}{k_B T}\frac{n}{\nu}\frac{\partial\mu}{\partial n}\frac{\partial\nu}{\partial\xi} && \text{(A.15)}\\
&= \left(\frac{n}{\partial n/\partial\xi}\right)\left(\frac{1}{\nu}\frac{\partial\nu}{\partial\xi}\right) && \text{(A.16)}\\
&= \left(\frac{\mathcal{F}_{\frac{1}{2}}(\xi)}{\mathcal{F}_{-\frac{1}{2}}(\xi)}\right)\left(\frac{1}{\langle\tau\rangle}\frac{\partial\langle\tau\rangle}{\partial\xi}\right) && \text{(A.17)}\\
&= \left(\frac{\mathcal{F}_{\frac{1}{2}}(\xi)}{\mathcal{F}_{-\frac{1}{2}}(\xi)}\right)\left(\frac{\mathcal{F}_{-\frac{1}{2}+s}(\xi)}{\mathcal{F}_{\frac{1}{2}+s}(\xi)} - \frac{\mathcal{F}_{-\frac{1}{2}}(\xi)}{\mathcal{F}_{\frac{1}{2}}(\xi)}\right) && \text{(A.18)}\\
&= \frac{\mathcal{F}_{-\frac{1}{2}+s}(\xi)/\mathcal{F}_{-\frac{1}{2}}(\xi)}{\mathcal{F}_{\frac{1}{2}+s}(\xi)/\mathcal{F}_{\frac{1}{2}}(\xi)} - 1 && \text{(A.19)}
\end{aligned}$$

Following a similar procedure for the diffusion constant yields

$$\begin{aligned}
\Theta &= \frac{D_\uparrow - D_\downarrow}{D_\uparrow + D_\downarrow}\frac{1}{p} \approx \frac{e}{\nu}\frac{\partial D}{\partial\mu} && \text{(A.20)}\\
&= \frac{1}{\nu}\frac{\partial}{\partial\xi}\left(\nu\frac{\mathcal{F}_{\frac{1}{2}}(\xi)}{\mathcal{F}_{-\frac{1}{2}}(\xi)}\right) && \text{(A.21)}\\
&= \frac{1}{\nu}\frac{\partial\nu}{\partial\xi}\frac{\mathcal{F}_{\frac{1}{2}}(\xi)}{\mathcal{F}_{-\frac{1}{2}}(\xi)} + \frac{\partial}{\partial\xi}\left(\frac{\mathcal{F}_{\frac{1}{2}}(\xi)}{\mathcal{F}_{-\frac{1}{2}}(\xi)}\right) && \text{(A.22)}\\
&= \Xi + 1 - \frac{\mathcal{F}_{\frac{1}{2}}(\xi)\,\mathcal{F}_{-\frac{3}{2}}(\xi)}{\left[\mathcal{F}_{-\frac{1}{2}}(\xi)\right]^2}. && \text{(A.23)}
\end{aligned}$$